UNIVERSITÀ DEGLI STUDI
DI MODENA E REGGIO EMILIA

Dottorato di ricerca in
Information and communication technologies (ICT)

Ciclo XXXVIII

Novel High Performance Electric Motors by means of Additive Manufacturing and Innovative Materials

Candidato: Giada Sala

Relatore: Prof. Claudio Bianchini

Coordinatore del Corso di Dottorato: Prof. Luigi Rovati

Sommario

Questa tesi presenta l'integrazione dell'Additive Manufacturing con la progettazione, l'ottimizzazione e la realizzazione di diverse tipologie di macchine elettriche: un motore a riluttanza tubolare, un motore a rotore avvolto e una macchina a flusso assiale. L'obiettivo dei progetti proposti è massimizzare le prestazioni delle macchine senza ricorrere all'utilizzo di materiali a terre rare.

La massimizzazione della densità di potenza dei motori elettrici riveste oggi un ruolo cruciale nelle applicazioni speciali. Essa può essere raggiunta attraverso una progettazione accurata della macchina e grazie all'impiego di materiali e tecniche produttive innovative. L'additive manufacturing offre un potenziale significativo per rivoluzionare la progettazione e la produzione delle macchine elettriche, consentendo di migliorarne le prestazioni termiche, elettromagnetiche e meccaniche. Inoltre, rispetto ai processi produttivi tradizionali, permette una notevole riduzione degli sprechi di materiale.

Inizialmente sono presentate le diverse tipologie di motore elettrico e una trattazione generale sulla modellazione analitica dei motori. In seguito, viene descritto un modello non lineare per la simulazione dei motori elettrici realizzato nel corso del dottorato. Tale modello consente di effettuare simulazioni rapide in ambiente PLECS ®, includendo la non linearità tramite le mappe delle induttanze e le perdite del ferro.

Viene presentato un metodo analitico di ottimizzazione generale per massimizzare la densità di potenza delle macchine elettriche. Partendo da un progetto di riferimento, il metodo consente di ottenere diverse geometrie di macchine con massa minimizzata, in funzione del diametro esterno dello statore.

In questo lavoro di tesi si presentano tre progetti di motori elettrici, accomunati dallo sfruttamento dell'Additive Manufacturing per ottenere geometrie innovative e ottimizzate.

Il primo motore è una macchina sincrona a riluttanza tubolare, con pistone realizzato tramite Additive Manufacturing. È stato sviluppato un modello analitico a parametri concentrati, derivato dallo stato dell'arte relativo ai motori rotativi, e

successivamente sono state condotte simulazioni parametriche per individuare le soluzioni più adatte all'applicazione proposta. Il prototipo è stato realizzato tramite additive manufacturing (in collaborazione con Raw Power Srl e m4p GmbH) utilizzando diverse polveri metalliche e successivamente testato per confrontare i risultati sperimentali con il modello analitico e con simulazioni FEA 2D.

Il secondo motore è un motore a rotore avvolto, il cui avvolgimento può essere realizzato mediante Additive Manufacturing. La particolare forma dei conduttori consente di massimizzare il fattore di riempimento del rotore, riducendo così le perdite Joule complessive a parità di punto di lavoro. Sono stati inoltre considerati avvolgimenti in alluminio per ridurre ulteriormente il peso del motore.

Il terzo motore è una macchina sincrona a riluttanza a flusso assiale a doppio sistema trifase. Anche in questo caso, grazie all'additive manufacturing, è stata sviluppata una geometria innovativa del rotore, che semplifica la configurazione tradizionale delle macchine a riluttanza per la topologia a flusso assiale, riduce la massa complessiva e migliora la densità di potenza.

Abstract

This thesis presents an integration of Additive Manufacturing with the design, optimization, and fabrication of different kinds of electrical machines: a tubular reluctance motor, a wound rotor motor and an axial flux machines. The proposed designs have the purpose of maximizing the performance of the machine without any dependence on rare-earth materials.

Nowadays the maximization of power density of electric motors is crucial for special applications: it can be obtained through a careful design of the machine and exploiting innovative materials and manufacturing techniques. Additive Manufacturing (AM) has the potential to innovate the design and manufacturing of Electric Machines (EMs) allowing an improvement in machine's thermal, electromagnetic, and mechanical performance. In addition, it is possible to reduce the waste of raw material compared to traditional manufacturing techniques.

Initially, the different types of electric motors and a general discussion on the analytical modeling of motors are presented. Subsequently, a nonlinear model for the simulation of electric motors developed during the PhD is described. This model enables fast simulations in the PLECS ® environment, including nonlinear effects through inductance maps and iron losses.

A general analytical optimization method to maximize the power density of electrical machines is presented. Starting from a reference design, thanks to this method different geometries of electrical machines with minimized mass can be obtained as a function of different outer stator diameter.

Three motor's design are presented, all of them exploit additive manufacturing to obtain innovative and optimized geometries.

The first motor is a tubular synchronous reluctance machine, whose plunger is produced using additive manufacturing. An analytical lumped parameter model for tubular machines is derived from the state of the art relating to rotational motors, then parametrized simulations are carried out to obtain the best solutions for the proposed application. The plunger was produced through metal additive manufacturing (thanks to Raw Power Srl and m4p GmbH) with different powder materials

and then tested to compare experimental results with the analytical model and 2D-FEA simulations.

The second motor is a wound rotor motor, whose rotor winding must be fabricated through metal additive manufacturing. The particular shape of the conductors allows the rotor filling factor to be maximized, reducing the total Joule losses in the rotor. Aluminum rotor windings are considered to reduce the weight of the motor.

The third one is a double three phase axial flux synchronous reluctance machine: also in this case, exploiting metal additive manufacturing, an innovative rotor geometry is obtained to simplify the traditional reluctance machine configuration, reducing the total mass of the machine and improving its power density.

Contents

List of Figures

List of Tables

Introduction

Nowadays, additive manufacturing (AM) has the potential to innovate the design and manufacturing of electric machines (EM). Thanks to AM new optimized geometries can be designed and manufactured with the purpose of improving machine's thermal, electromagnetic and mechanical performance [1], [2], [3]. In addition, it is possible to reduce the waste of raw material compared to traditional manufacturing techniques.

Nevertheless, AM still has some limitations that make it unsuitable for today's industrial production. Some of the most relevant disadvantages are:

- limited maximum size of the part;
- long manufacturing times;
- the need of finishing machining;
- the need of post processing such as annealing to obtain the desired mechanical or electromagnetic properties;
- high cost.

Recent scientific researches have shown some promising results for the manufacturing of the high efficiency EM.

In the context of the energy transition, electric motors are strictly connected to renewable energy sources, since they constitute one of the main technologies for converting electrical energy from sustainable generation systems into mechanical power. In 2019, only 4.5% of the total electricity harnessed in the EU came from the conversion of solar thermal energy to electricity by photovoltaic effect [4], [5].

Referring to 2022, more than half (56.1%) of the net electricity generated in the EU in 2022 came from non-combustible primary sources. Less than half (43.9%) came from combustible fuels (such as natural gas, coal and oil). Less than a quarter (21.4%) came from nuclear power stations. Among the renewable energy sources, the highest share of net electricity generation in 2022 was from wind turbines (15.4%),

followed by hydropower plants (11.2%) and solar power (7.7%).

The relative significance of renewable energy sources in relation to EU net electricity generation was almost constant between 2019 and 2022.

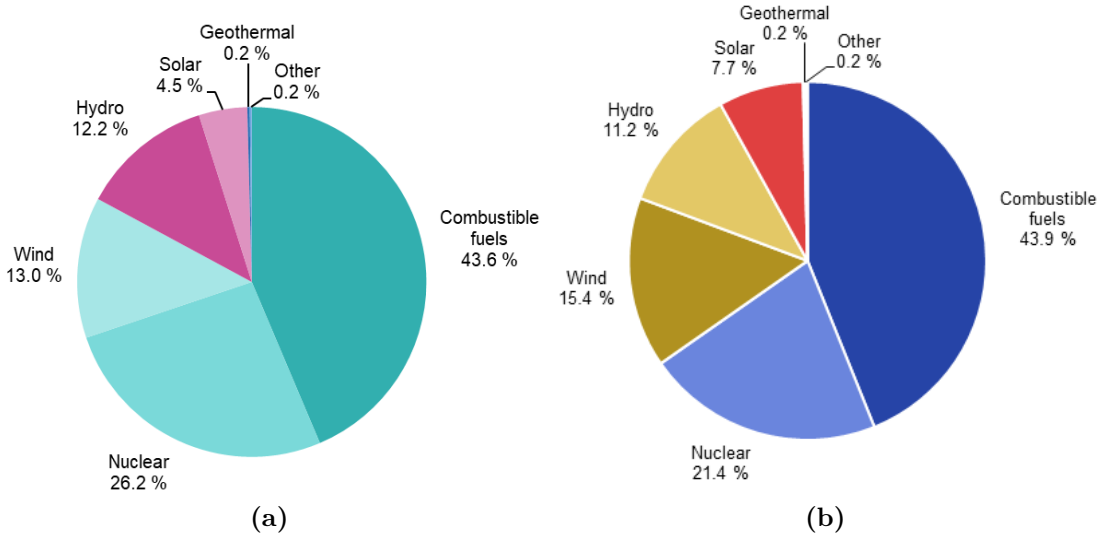

Figure 0.1: Net electricity conversion, EU; 2019(a) and 2022 (b) (% based on GWh) [4]

In addition, EMs for industrial applications, indicatively, took up 40% of the total available electricity and were expected to increase by 15% per year in the near future.

Referring to the present year a preliminary report on the renewable energy generation sources in the EU was made at the end of the first quarter of 2025 (see Figure 0.2).

The electricity conversion from combustible fuels has significantly decreased, going from 43.9 % to 9.8 %. On the other side, solar, hydro and wind became the most important sources for electricity conversion during the last years. With respect to 2022, the relative significance of renewable energy sources in relation to EU net electricity generation increased.

The massive and increasing use of EMs is evident, so it is of paramount importance to continuously develop and innovate EMs.

In this regard, in order to meet the new EU efficiency parameters required for all electric motors rated from 0.75 up to 1000 kW belonging to IE4 class. This task is really challenging beacuse in order to raise the efficiency by 2 percentage points

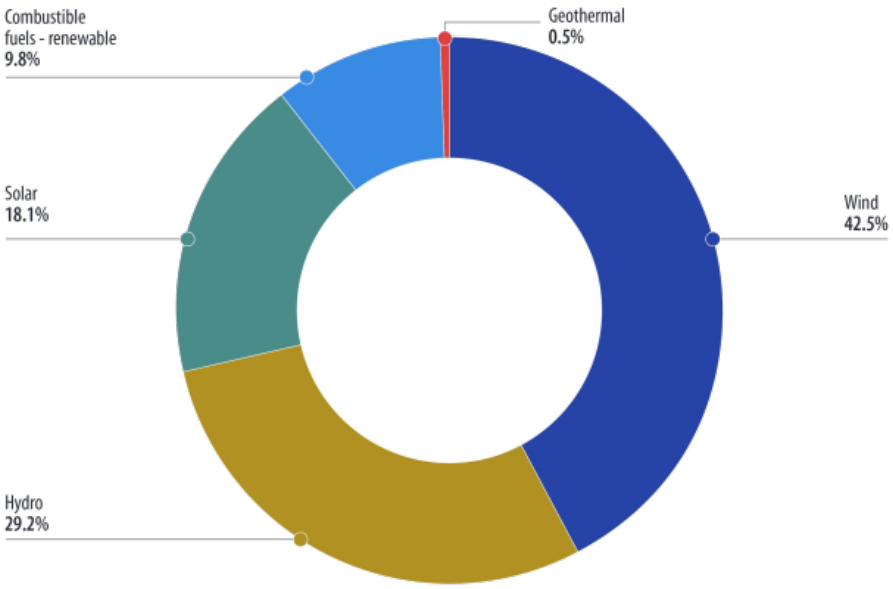

Figure 0.2: Net electricity conversion, EU; 2025 (% based on GWh) [4]

from 92% to 94%, the machine energy losses should be reduced by 25% [6]. In fact, most motor losses result in heat rejected into the atmosphere, reducing losses can significantly reduce cooling loads on an industrial facility's air conditioning system [7], [8].

In light of this, the development of new materials integrated into modern Additive Manufacturing (AM) technologies is what could have the greatest impact on the performance of future EMs [9]. Other areas of research such as control, design, and optimization allow for the refinement of the machine for implementation in the specific application, but it is the materials and manufacturing techniques that impose the practical limits of the machine itself [10].

This work of thesis presents different machines designs obtained using metal additive manufacturing. Initially, Chapter 1 provides an overview of the electrical machines topologies and their analytical modeling. Chapter 2 presents an efficient fast simulation non linear model which simulates electric motors. In Chapter 3 the well known traditional analytical design procedure for SPM machines is reported and, then an optimization analytical method to increase the power density is presented applied to a 10 kW electric motor. Then Chapter 4 presents a general overview on the AM technologies applied to electrical machines. After that, three applications of AM to electrical machines are presented and analyzed:

- Chapter 5 presents the analytical model and feasibility assessment of a synchronous reluctance tubular electrical machine with the rotor in additive manufacturing;
- Chapter 6 investigates an innovative additively manufactured winding design for a wound rotor machine;
- Chapter 7 presents an innovative double three phase axial flux machine with the rotor obtained through additive manufacturing.

The main software used for the simulations of these machines are FEMM®[11], MATLAB®[12] and PLECS®[13].

0.1 References

[1] M. U. Naseer, A. Kallaste, B. Asad, T. Vaimann, and A. Rassõlkin, «A review on additive manufacturing possibilities for electrical machines», *Energies*, vol. 14, no. 7, 2021, doi:10.3390/en14071940, ISSN: 1996-1073.

[2] T. Pham, P. Kwon, and S. Foster, «Additive manufacturing and topology optimization of magnetic materials for electrical machines—a review», *Energies*, vol. 14, no. 2, 2021, doi:10.3390/en14020283, ISSN: 1996-1073.

[3] D. Matt, L. Piscini, N. Boubaker, A. Gimeno, P. Enrici, and M. Aitakkache, «Low-voltage, high-frequency synchronous motor for aerospace applications», *Electronics*, vol. 11, no. 17, 2022, doi:10.3390/electronics11172719, ISSN: 2079-9292.

[4] EuroStat, *Electricity production, consumption and market overview.*

[5] S. R. S, P. Venugopal, R. V, H. Haes Alhelou, A. Al-Hinai, and P. Siano, «Analysis of electric vehicles with an economic perspective for the future electric market», *Future Internet*, vol. 14, no. 6, 2022, doi:10.3390/fi14060172, ISSN: 1999-5903.

[6] G. Bramerdorfer, J. A. Tapia, J. J. Pyrhönen, and A. Cavagnino, «Modern electrical machine design optimization: Techniques, trends, and best practices», *IEEE Transactions on Industrial Electronics*, vol. 65, no. 10, pp. 7672–7684, 2018.

[7] H. Tiismus, A. Kallaste, T. Vaimann, and A. Rassõlkin, «State of the art of additively manufactured electromagnetic materials for topology optimized electrical machines», *Additive Manufacturing*, vol. 55, p. 102 778, 2022, ISSN: 2214-8604.

[8] *Premium efficiency motor selection and application guide.* A guidebook for industry, Accessed on January 10th, 2023.

[9] T. Vaimann and A. Kallaste, «Additive manufacturing of electrical machines;towards the industrial use of a novel technology», *Energies*, vol. 16, no. 1, 2023, ISSN: 1996-1073.

[10] H. Tiismus, A. Kallaste, T. Vaimann, *et al.*, «Laser additively manufactured magnetic core design and process for electrical machine applications», *Energies*, vol. 15, no. 10, 2022, doi:10.3390/en15103665, ISSN: 1996-1073.

[11] FEMM by David Meekers .

[12] T. M. Inc., *Matlab version: 9.13.0 (r2022b)*, Natick, Massachusetts, United States, 2025. [Online]. Available: `https://www.mathworks.com`.

[13] Plexim, *The simulation platform for power electronic systems - user manual version 4.8.1*, 2024.

1. An Overview of Synchronous Electrical Machines

In this chapter, the essential characteristics of synchronous motors are presented. Synchronous electric motors play a fundamental role in modern electromechanical systems, offering high efficiency, precise speed control, and excellent torque density. Unlike asynchronous machines, synchronous motors operate at a constant speed that is directly proportional to the supply frequency, regardless of load variations. This characteristic makes them highly suitable for applications requiring accurate speed regulation, such as industrial automation [1], robotics, and electric vehicles [2], [3].

Recent advancements in materials, power electronics, and control algorithms have significantly improved the performance and reliability of synchronous machines. Among the various configurations, Permanent Magnet Synchronous Motors (PMSMs) have gained particular attention due to their high power density, compact size, and reduced losses. However, challenges such as thermal management, demagnetization risk, and cost of rare-earth materials still represent important aspects of ongoing research and optimization.

This chapter provides an overview of synchronous motor technologies, describing their operating principles, main topologies, and key design considerations.

A general overview about the operating principle of synchronous electrical machines is made and the $d-q$ axis reference frame is introduced.

1.1 Operating Principle of Synchronous Electric Motors

An electric motor is a device that allows to convert electrical energy into mechanical energy. Its operation is based on electromagnetic principles and the interaction between magnetic fields and electric currents.

The electromechanical conversion they perform follows the operating principle of

electrodynamic systems, which is based on the interaction between current-carrying conductors and magnetic fields generated by other conductors or by permanent magnets. The conductors on which the forces act are placed in the stator (the stationary part), while the permanent magnets are mounted on the rotor.

The stator is characterized by a three phase winding, in which each phase has the same total number of conductors. The three phases are mutually phase-shifted by 120 degrees and they are connected to an external three phase voltage source.

Referring to traditional radial flux machines, permanent magnet brushless motor are made of two parts: a stator, in which there are the windings, distributed in the slots, and a rotor, in which there are permanent magnets. Permanent magnets are fixed on the rotor laminations by high resistivity resins, and they are the excitation system of the machine.

The stator windings can be distributed, when the winding has a width of a polar pitch and there is an integer number of slots per pole per phase, or non-overlapping concentrated, in which every winding is wrapped around a tooth and the number of slots per pole per phase is fractional.

The rotor can be internal (as in Figure 1.1) or external, both configuration having radial flux; usually the internal configuration is the most utilized because it makes easier to remove the heat from the joule losses into the stator. Otherwise, it can be used a rotor disc, which leads to an axial flux.

Figure 1.1: Example of an inner rotor synchronous permanent magnet machine.

The great innovation of brushless motor is, as suggested by the name, the absence of brushes on the rotor shaft, which leads to several advantages such as a lower maintenance in long-term, since brushes were the most fragile part and they generated a lot of heat, a lower production of electromagnetic noise, a lower motor inertia which allows a better control in speed and in torque. In face of all these advantages, there are a few disadvantages such as the need of a complex and expansive controller and the high costs of the permanent magnets needed for the operating of the machine.

Synchronous machine can be divided into:

- surface permanent magnet machines, which can have inner or outer rotor;
- internal permanent magnet machines;
- axial flux machines;
- pure reluctance machines;
- wound rotor machines.

1.2 d-q Axis Reference Frame for SPM Machines

The convention used for PM machines states that the d-axis is oriented along the direction of minimum inductance of the rotor ($L_d < L_q$). This convention is generally used for SPM (where $L_d = L_q$) and IPM motors. As shown in Figure 1.2, the magnet flux vector λ_m is oriented along d-axis.

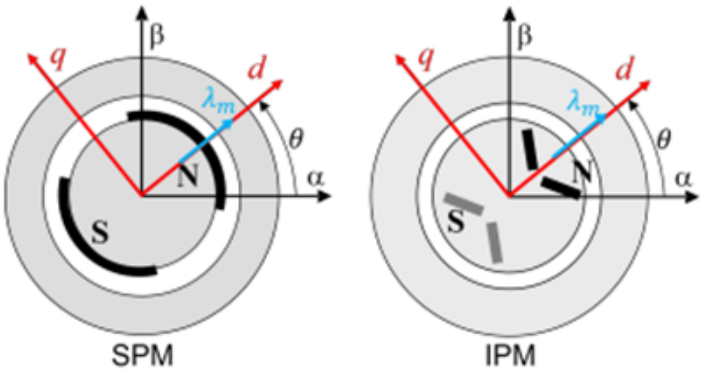

Figure 1.2: Convention of $d-q$ axis reference frame for PM machines.

In SPM machines $L_d = L_q$, so isotropic electrical machines are taken into account,

and the stator synchronous inductances of d-q axis have the same value, which corresponds to rotor magnetic permeance and it is equal in every radial direction. So, in this case, the saliency ratio $\xi = L_{sq}/L_{sd}$ is equal to 1.

Given the three-phase stator reference frame of a three-phase sinusoidal electrical machines, reported in Figure 1.3, it is possible to obtain the voltage equation as in (1.1), according to the passive sign convention.

$$\begin{cases} v_{su}(t) = R_s i_{su}(t) + \frac{d\Lambda_{su}(t)}{dt} \\ v_{sv}(t) = R_s i_{sv}(t) + \frac{d\Lambda_{sv}(t)}{dt} \\ v_{sw}(t) = R_s i_{sw}(t) + \frac{d\Lambda_{sw}(t)}{dt} \end{cases} \tag{1.1}$$

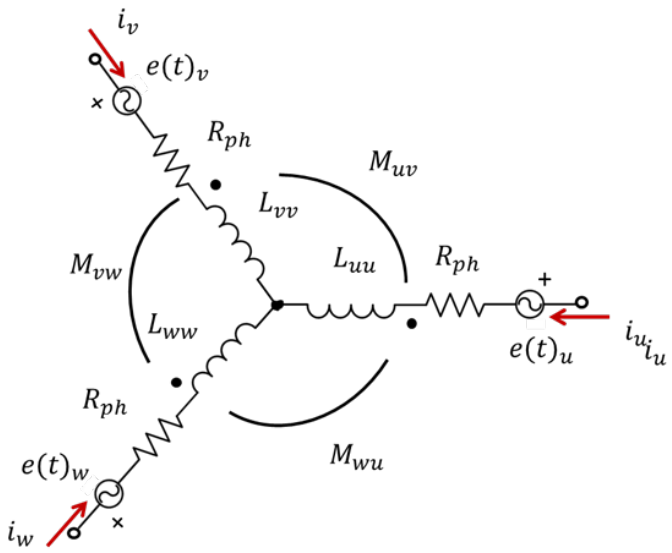

Figure 1.3: Three-phase stator reference frame.

Where i_{su}, i_{sv} and i_{sw} are the phase currents that flows in the three-phase winding and Λ_{su}, Λ_{sv} and Λ_{sw} are total magnetic fluxes linkage to each stator phase. The R_s term is the stator phase resistance and it is assumed equal for each stator winding.

According to (1.1), each winding terminal voltage is the sum of the resistance voltage drop and the inductive voltage drop occurring along the winding. Assuming that magnetic circuits work in linear magnetization conditions, which means far from the saturating point, the total magnetic flux is given by the sum of two contributions, according to (1.2).

$$\begin{cases} \Lambda_{su}(t) = \Lambda_{su,cp}(t) + \Lambda_{su,pm}(t) \\ \Lambda_{sv}(t) = \Lambda_{sv,cp}(t) + \Lambda_{sv,pm}(t) \\ \Lambda_{sw}(t) = \Lambda_{sw,cp}(t) + \Lambda_{sw,pm}(t) \end{cases} \tag{1.2}$$

Where $\Lambda_{s,cp}$ is the magnetic flux induced by stator currents and it relies on winding distribution and type and $\Lambda_{s,pm}$ is the magnetic flux produced by permanent-magnets and its value is a function of the relative position of the rotor to stator windings. The current flowing in each phase produces a Magneto-Motive Force (MMF), according to the Ampère's Law, which induces a magnetic flux. The induced magnetic flux links both with same phase winding and the other two phases. The magnetic flux can be split into two components: the self-inductance coefficient L, which considers the magnetic flux linked with the winding in which flows the same current that establish the magnetic flux, and the mutual-inductance coefficient M, which considers the magnetic flux linked to the other windings of the two phases. Considering a symmetrical three-phase system, these coefficients are equal for each phase, so the magnetic flux induced by stator currents $\Lambda_{s,cp}$ can be obtained as in (1.3).

$$\begin{cases} \Lambda_{su,cp}(t) = Li_{su}(t) + Mi_{sv}(t) + Mi_{sw}(t) \\ \Lambda_{sv,cp}(t) = Mi_{su}(t) + Li_{sv}(t) + Mi_{sw}(t) \\ \Lambda_{sw,cp}(t) = Mi_{su}(t) + Mi_{sv}(t) + Li_{sw}(t) \end{cases} \tag{1.3}$$

Three phase systems are usually connected with wye-connection, so the Kirchhoff principle must be verified, and the following system of equation is true at any time.

$$\begin{cases} i_{sv}(t) + i_{sw}(t) = -i_{su}(t) \\ i_{su}(t) + i_{sw}(t) = -i_{sv}(t) \\ i_{su}(t) + i_{sv}(t) = -i_{sw}(t) \end{cases} \tag{1.4}$$

Substituting (1.4) in (1.3), a new system of equations for $\Lambda_{s,cp}$ can be obtained.

$$\begin{cases} \Lambda_{su,cp}(t) = (L - M)i_{su}(t) \\ \Lambda_{sv,cp}(t) = (L - M)i_{sv}(t) \\ \Lambda_{sw,cp}(t) = (L - M)i_{sw}(t) \end{cases} \tag{1.5}$$

The synchronous inductance L_s is defined as the sum of the contribution of the self-inductance and the mutual inductance, as in (1.6).

$$L_s = L - M \tag{1.6}$$

So, in the end, the system can be written in function of the synchronous inductance, as in (1.7).

$$\begin{cases} \Lambda_{su,cp}(t) = L_s i_{su}(t) \\ \Lambda_{sv,cp}(t) = L_s i_{sv}(t) \\ \Lambda_{sw,cp}(t) = L_s i_{sw}(t) \end{cases} \tag{1.7}$$

The magnetic flux of the permanent magnet links each stator winding, assuming a sinusoidal distribution of flux density vector field $\vec{B}$, the linkage permanent magnet flux $\Lambda_{s,pm}$ for each phase is expressed with the following system of equations:

$$\begin{cases} \Lambda_{su,PM}(t) = \Lambda_{PM} \cos(\theta) \\ \Lambda_{sv,PM}(t) = \Lambda_{PM} \cos\left(\theta - \frac{2}{3}\pi\right) \\ \Lambda_{sw,PM}(t) = \Lambda_{PM} \cos\left(\theta - \frac{4}{3}\pi\right) \end{cases} \tag{1.8}$$

Where θ is the electric angle and Λ_{PM} is the peak value of the permanent magnet leakage flux. It is now possible to obtain the machine equations in the two-axis stationary frame $\alpha - \beta$, starting from the machine equations just obtained in the three-phase system and using Clarke's transformation. Figure 1.4 represents the

three phase reference frame and the $\alpha - \beta$ reference frame.

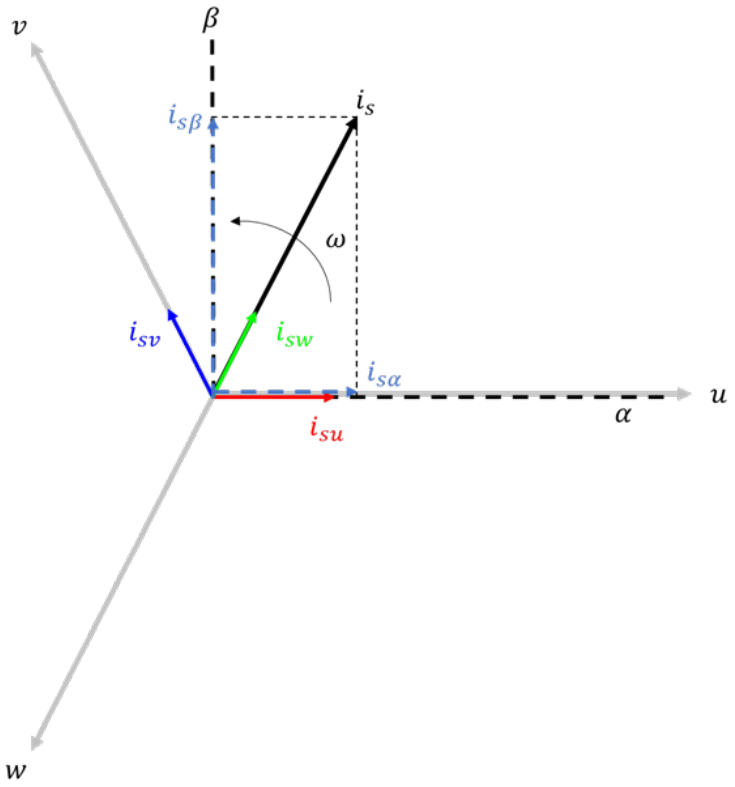

Figure 1.4: From three phase reference frame to two-axis stationary frame $\alpha - \beta$.

The Clarke's Transformation is a mathematical transformation to simplify the analysis of three-phase systems. The three-phase winding is transformed in a two-axis system in the stationary frame composed by $\alpha - \beta$ windings perpendicular to each other. The matrix used for Clarke's transformation can have two forms, one at constant amplitude and one at constant power.

To get the new notation in a more readable way, it is convenient to consider a matrix representation of the systems of equations found before, as in (1.9).

$$[v_s]_{uvw} = [R_s]_{uvw} [i_s]_{uvw} + [L_s]_{uvw} \frac{d[i_s]_{uvw}}{dt} + \frac{d[\Lambda_{s,PM}]_{uvw}}{dt} \tag{1.9}$$

Where

$$[i_s]_{uvw} = \begin{bmatrix} i_{su} \\ i_{sv} \\ i_{sw} \end{bmatrix} \tag{1.10}$$

Here, the phase resistances and the synchronous inductances can be represented as two matrices, according to (1.11) and (1.12).

$$[R_s]_{uvw} = \begin{bmatrix} R_s & 0 & 0 \\ 0 & R_s & 0 \\ 0 & 0 & R_s \end{bmatrix} \tag{1.11}$$

$$[L_s]_{uvw} = \begin{bmatrix} L_s & 0 & 0 \\ 0 & L_s & 0 \\ 0 & 0 & L_s \end{bmatrix} \tag{1.12}$$

To obtain machine equation in the two-axis stationary frame, both members of (1.9) are multiplied by Clarke's transformation matrix $T^{\alpha\beta}_{uvw}$, reported in (1.13), assuming the constant power form, so considering $K = \sqrt{\frac{2}{3}}$.

$$T^{\alpha\beta}_{uvw} = K \begin{bmatrix} 1 & -\frac{1}{2} & -\frac{1}{2} \\ 0 & \frac{\sqrt{3}}{2} & -\frac{\sqrt{3}}{2} \end{bmatrix} \tag{1.13}$$

After some calculations, currents (1.14) and voltages (1.15) in the two-axis stationary frame are obtained.

$$\begin{bmatrix} i_{s\alpha} \\ i_{s\beta} \end{bmatrix} = K \begin{bmatrix} 1 & -\frac{1}{2} & -\frac{1}{2} \\ 0 & \frac{\sqrt{3}}{2} & -\frac{\sqrt{3}}{2} \end{bmatrix} \begin{bmatrix} i_{su} \\ i_{sv} \\ i_{sw} \end{bmatrix} \tag{1.14}$$

$$\begin{bmatrix} v_{s\alpha} \\ v_{s\beta} \end{bmatrix} = K \begin{bmatrix} 1 & -\frac{1}{2} & -\frac{1}{2} \\ 0 & \frac{\sqrt{3}}{2} & -\frac{\sqrt{3}}{2} \end{bmatrix} \begin{bmatrix} v_{su} \\ v_{sv} \\ v_{sw} \end{bmatrix} \tag{1.15}$$

THen, the phase resistance and the synchronous inductance in the two-axis stationary frame are found as in (1.16) and (1.17).

$$[R_s]_{\alpha\beta} = \begin{bmatrix} R_s & 0 \\ 0 & R_s \end{bmatrix} \tag{1.16}$$

$$[L_s]_{\alpha\beta} = \begin{bmatrix} L_s & 0 \\ 0 & L_s \end{bmatrix} \tag{1.17}$$

The machine equations in two-axis stationary frame become as in (1.18).

$$\begin{cases} v_{s\alpha} = R_s i_{s\alpha} + \frac{d\Lambda_{s\alpha}}{dt} \\ v_{s\beta} = R_s i_{s\beta} + \frac{d\Lambda_{s\beta}}{dt} \end{cases} \tag{1.18}$$

Which in matrix notation can be written as in Equation 1.19.

$$[v_s]_{\alpha\beta} = [R_s]_{\alpha\beta} [I_s]_{\alpha\beta} + \frac{d [\Lambda_s]_{\alpha\beta}}{dt} \tag{1.19}$$

Now Park's transformation $T_{\alpha\beta}^{dq}$ can be applied, to move from the two-axis stationary frame $\alpha - \beta$ to the two-axis rotational frame $d - q$, which rotates synchronously with the rotor angular speed ω. The current phasor i_s has a constant amplitude and an angular speed $\omega = \frac{d\theta}{dt}$ and it is out-of-phase of a generic angle γ, as shown in Figure 1.5.

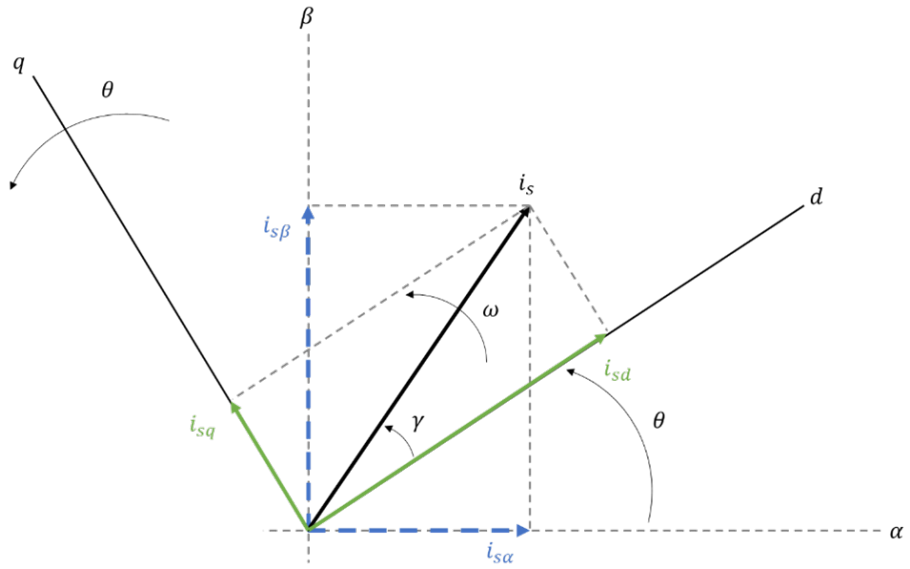

Figure 1.5: From two-axis stationary frame $\alpha-\beta$ to two-axis rotational frame $d-q$.

Park's transformation matrix is reported in (1.20).

$$T_{\alpha\beta}^{dq} = \begin{bmatrix} \cos(\theta) & \sin(\theta) \\ -\sin(\theta) & \cos(\theta) \end{bmatrix} \tag{1.20}$$

So, the machine equations in two-axis rotational frame can be found by multiplying Park's transformation matrix for each term of (1.19). In (1.21) the matrix form is reported, while (1.22) shows the system of equations.

$$[v_s]_{dq} = [R_s]_{dq} [I_s]_{dq} + \frac{d[\Lambda_s]_{dq}}{dt} + j\omega_{el} [\Lambda_s]_{dq} \tag{1.21}$$

$$\begin{cases} v_{sd} = R_s i_{sd} + \frac{d\Lambda_{sd}}{dt} + j\omega_{el}\Lambda_d \\ v_{sq} = R_s i_{sq} + \frac{d\Lambda_{sq}}{dt} + j\omega_{el}\Lambda_q \end{cases} \tag{1.22}$$

The term $j\omega_{el} [\Lambda_s]_{dq}$ represents the counter electromotive force and it is due to the rotational motion of the $d-q$ frame. The terms $[\Lambda_s]_{dq}$ and $j[\Lambda_s]_{dq}$ have the same amplitude and are perpendicular to each other, since a multiplication for j means a

counter clock rotation of 90 °.

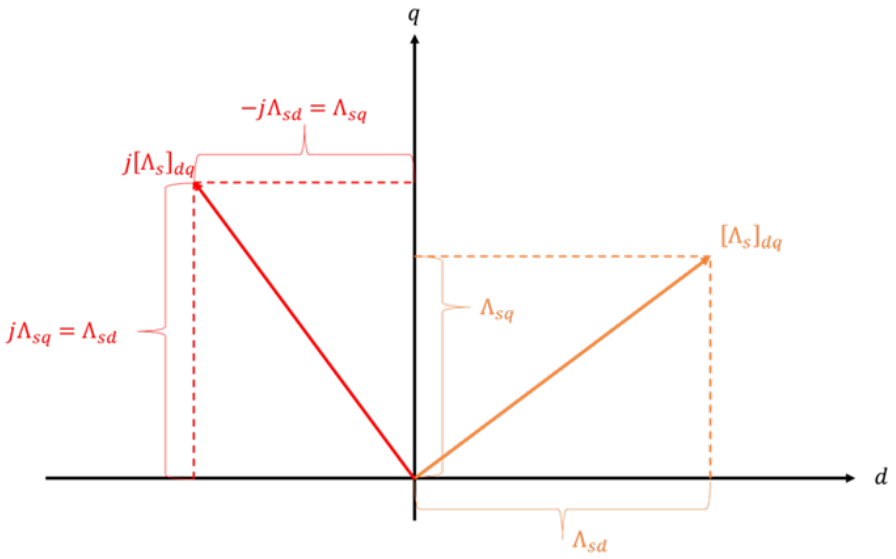

Figure 1.6: Correlation between vectors $[\Lambda_s]_{dq}$ and $j\,[\Lambda_s]_{dq}$.

The magnetic linkage flux can be expressed as in (1.23), because the direct axis d coincides with rotor polar axis, so the permanent magnets produce a constant flux $\Lambda_{sd,pm}$ in the axis d direction and null in axis q direction.

$$\begin{cases} \Lambda_{sd} = L_s i_{sd} + \Lambda_{sd,pm} \\ \Lambda_{sq} = L_s i_{sq} \end{cases} \tag{1.23}$$

Substituting (1.23) in (1.22), the voltage equations in d-q axis rotational frame are obtained as in (1.24).

$$\begin{cases} v_{sd} = R_s i_{sd} + L_s \frac{di_{sd}}{dt} - \omega_{el} L_s i_{sq} \\ v_{sq} = R_s i_{sq} + L_s \frac{di_{sq}}{dt} + \omega_{el} L_s i_{sd} + \omega_{el} + \omega_{el} \Lambda_{sd,pm} \end{cases} \tag{1.24}$$

Starting from (1.24), the torque expression can be obtained, by multiplying each row by current i_{sd} and i_{sq} and then, by summing the two equations' members to get the power balance.

$$v_{sd}i_{sd} + v_{sq}i_{sq} = R_s i_{sd}^2 + R_s i_{sq}^2 + L_s \frac{di_{sd}}{dt} i_{sd} + L_s \frac{di_{sq}}{dt} i_{sq} + \omega_{el} \Lambda_{sd,pm} i_{sq} \tag{1.25}$$

Where it can be noticed that:

- $v_{sd}i_{sd} + v_{sq}i_{sq} = P_{Abs}$ is the input power absorbed by the electrical machine;
- $R_s \left(i_{sd}^2 + i_{sq}^2 \right) = P_{Joule}$ represents the Joule losses inside the windings;
- $L_s(\frac{di_{sd}}{dt} i_{sd} + \frac{di_{sq}}{dt} i_{sq}) = P_{Mag}$ represents the magnetic energy stored inside the stator magnetic circuits;
- $\omega_{el} \Lambda_{sd,pm} i_{sq} = P_{Mec}$ represents the mechanical power produced by the electrical machine.

So, (1.25) can be rewritten in a simpler way, to highlight the power terms.

$$P_{abs} = P_{Joule} + P_{mag} + P_{mec} \tag{1.26}$$

Knowing that the mechanical power produced by the electrical machine can be expressed in function of the torque produced T_{mec} and the mechanical angular velocity ω_{mec} and supposing that all the electrical power produced will be transformed in mechanical power, (1.27) can be obtained.

$$T_{mec}\omega_{mec} = \omega_{el} \Lambda_{sd,pm} i_{sq} \tag{1.27}$$

So, the torque produced by the electrical machine can be easily found as in (1.28).

$$T_{mec} = \frac{\omega_{el} \Lambda_{sd,pm} i_{sq}}{\omega_{mec}} \tag{1.28}$$

Where $\omega_{mec} = \frac{\omega_{el}}{p}$ can be substituted, in which p is the number of pole pairs.

$$T_{mec} = p\Lambda_{sd,pm} i_{sq} \tag{1.29}$$

Generally, the Clark's transformation from a three-phase system to a two-axis stationary frame is made using the coefficient for a constant amplitude transformation, as seen before. According to that, the mechanical power computed in the two-axis reference frame is less than the real one in the three-phase system, according to (1.30).

$$P_{\alpha\beta} = \frac{2}{3} P_{uvw} \tag{1.30}$$

To guarantee the correct energy balance, the toque equation found in (1.29) must be multiplied by a corrective coefficient. The final formula is expressed as in (1.31).

$$T_{mec} = \frac{3}{2} p\Lambda_{sd,pm} i_{sq} \tag{1.31}$$

1.3 *d*-*q* Axis Reference Frame for IPM Machines

When IPM machines are taken into account the inductances on d and on q axis have different values and generally the relation is $L_d < L_q$. In this case, anisotropy is introduced and the saliency ratio is major than 1.

In this case, the inductance value for each phase depends on an oscillating term which is different depending on the phase and the rotor position. So the fluxes found in (1.3) can be rewritten according to (1.32) for IPM machines.

$$\begin{cases} \Lambda_{su,cp}(t) = L_{uu} i_{su}(t) + M_{uv} i_{sv}(t) + M_{uw} i_{sw}(t) \\ \Lambda_{sv,cp}(t) = M_{vu} i_{su}(t) + L_{vv} i_{sv}(t) + M_{vw} i_{sw}(t) \\ \Lambda_{sw,cp}(t) = M_{wu} i_{su}(t) + M_{wv} i_{sv}(t) + L_{sw} i_{ww}(t) \end{cases} \tag{1.32}$$

For each phase auto inductances can be computed according to the following equations, where L_{g0} is the mean magnetizing inductance, L_σ is the leakage inductance and L_{g2} is the oscillating term generated by motor anisotropy as it depends on rotor position.

$$L_{uu} = L_{g0} + L_\sigma - \hat{L}_{g2} \cos\left(2\theta_{el}\right) \tag{1.33}$$

$$L_{vv} = L_{g0} + L_\sigma - \hat{L}_{g2} \cos\left(2\theta_{el} + \frac{2}{3}\pi\right) \tag{1.34}$$

$$L_{ww} = L_{g0} + L_\sigma - \hat{L}_{g2} \cos\left(2\theta_{el} + \frac{4}{3}\pi\right) \tag{1.35}$$

The mutual inductances can be found as follows, assuming the same oscillating term.

$$M_{uv} = M_{g0} + M_\sigma - \hat{L}_{g2} \cos\left(2\theta_{el}\right) \tag{1.36}$$

$$M_{vw} = M_{g0} + M_\sigma - \hat{L}_{g2} \cos\left(2\theta_{el} + \frac{2}{3}\pi\right) \tag{1.37}$$

$$M_{uw} = M_{g0} + M_\sigma - \hat{L}_{g2} \cos\left(2\theta_{el} + \frac{4}{3}\pi\right) \tag{1.38}$$

Generally, it is $M_{g0} = -\frac{L_{g0}}{2}$. These components generates the inductance matrix $[L_s]_{uvw}$ for the matrix notation as in (1.9).

Employing the transformation matrix $T^{\alpha\beta}_{uvw}$ reported in (1.13) it is possible to obtain the inductance matrix in the two axis stationary frame for IPM machines.

$$[L_s]_{\alpha\beta} = \begin{bmatrix} \frac{3}{2}L_{g0} + L_\sigma - \frac{3}{2}\hat{L}_{g2}\cos(2\theta_{el}) & -\frac{3}{2}\hat{L}_{g2}\sin(2\theta_{el}) \\ -\frac{3}{2}\hat{L}_{g2}\sin(2\theta_{el}) & \frac{3}{2}L_{g0} + L_\sigma + \frac{3}{2}\hat{L}_{g2}\cos(2\theta_{el}) \end{bmatrix} \tag{1.39}$$

This matrix is used to model IPM machines as in (1.19) in two axis stationary frame.

Then to obtain the final model in d-q axis rotational frame Park's transformation matrix $T^{dq}_{\alpha\beta}$, reported in (1.20), is used.

$$[L_s]_{dq} = \begin{bmatrix} L_d & 0 \\ 0 & L_q \end{bmatrix} = \begin{bmatrix} \frac{3}{2}L_{g0} + L_\sigma - \frac{3}{2}\hat{L}_{g2} & 0 \\ 0 & \frac{3}{2}L_{g0} + L_\sigma + \frac{3}{2}\hat{L}_{g2} \end{bmatrix} \tag{1.40}$$

With this matrix the final model in d-q axis rotational frame can be obtained for IPM machines as in (1.21).

1.4 Conclusions

This chapter has provided a rigorous derivation of the mathematical model for synchronous electric motors, focusing on the fundamental coordinate transformations that simplify the analysis of three-phase electromagnetic systems. By transitioning from the physical *abc* reference frame to the stationary $\alpha\beta$ frame and, ultimately, to the rotor-aligned dq synchronous frame, a coherent analytical framework has been established.

The application of the Clarke and Park transformations has successfully decoupled the time-varying nature of the stator inductances. This transformation converts a system of differential equations with time-dependent coefficients into a more manageable set of equations, where the electrical quantities are represented as constant vectors during steady-state operation.

The adoption of the Space Vector formalism provides a powerful tool for visualizing the interaction between the stator magnetomotive force and the rotor magnetic field. This representation is not only elegant from a mathematical perspective but also essential for the implementation of modern pulse-width modulation (PWM)

techniques.

The *dq* model developed herein serves as the indispensable baseline for any high-performance control strategy, such as Field-Oriented Control (FOC).

In conclusion, the transition from phase variables to *dq* components provides the necessary analytical clarity to describe the motor's behavior under both transient and steady-state conditions. This mathematical structure constitutes the essential "skeleton" upon which the non-linearities (such as saturation and cross-coupling) and the models discussed in the subsequent chapters will be built.

1.5 References

[1] W. Maogang and Z. Rongxiang, «A novel mixed speed regulation method for permanent magnet synchronous motor with high precision», in *2009 Chinese Control and Decision Conference*, 2009, pp. 258–261. DOI: 10.1109/CCDC.2009.5195092.

[2] S. Sharifan, S. Ebrahimi, A. Oraee, and H. Oraee, «Performance comparison between brushless pm and induction motors for hybrid electric vehicle applications», in *2015 Intl Aegean Conference on Electrical Machines & Power Electronics (ACEMP), 2015 Intl Conference on Optimization of Electrical & Electronic Equipment (OPTIM) & 2015 Intl Symposium on Advanced Electromechanical Motion Systems (ELECTROMOTION)*, 2015, pp. 719–724. DOI: 10.1109/OPTIM.2015.7492473.

[3] M. D. S and V. Bagyaveereswaran, «Electric motor systems: Relative study on diverse motors in the electric vehicles», in *2023 Innovations in Power and Advanced Computing Technologies (i-PACT)*, 2023, pp. 1–6. DOI: 10.1109/i-PACT58649.2023.10434509.

2. Inductance Based Lumped Parameter IPM Machine Model for Fast Simulation

The increasing demand for high power density and superior energy efficiency in modern electromechanical conversion systems has pushed the design of electric motors toward operating points characterized by deep magnetic saturation. In this context, the traditional assumption of magnetic linearity—while computationally convenient—is no longer a viable approximation for describing the dynamic behavior of the machine, particularly during heavy load conditions or high-speed flux-weakening operations.

This chapter employs the analytical model presented before to build an advanced non-linear model of the electric motor, centered on the accurate characterization of d and q-axis inductances as functions of the stator currents. Moving beyond constant-parameter models, the proposed approach explicitly accounts for two critical physical phenomena that dictate high-performance drive behavior:

- magnetic Saturation: the variation in the permeability of the ferromagnetic core, which leads to a non-linear reduction of inductances as current magnitude increases;
- cross-magnetization (Cross-Coupling): the mutual interaction between the d and q axes, where the flux linkage of one axis is significantly influenced by the current component of the orthogonal axis.

Furthermore, this model includes the voltage drop due to iron losses.

The following sections will detail the model and the parameter identification procedure through Finite Element Analysis (FEA). In the end a robust validation of the model is provided through experimental measurements. The results demonstrate a significant improvement in voltage estimation accuracy and dynamic response compared to conventional linear modeling.

2.1 Non linear models of electric motors

To obtain the desired performance from an IPM machine a good control design is crucial and during this design phase, it is fundamental to have a good model which allows to simulate the behaviour coupled with the inverter and the related control strategies.

The traditional d-q axes reference frame is based on the assumption of constant L_d and L_q, nevertheless it can lead to a significant error respect to the performance of a actual machine where the inductances show a current dependent behaviour and a cross saturation between the d and q axes.

The difference between the performance with a constant inductance and a complete magnetic model based on frozen permeabilty method for steady state condition is presented in Figure 2.1 (a) and in Figure 2.1 (b) from [1]. As expected not only the MTPA, FW, MTPV trajectories are different, but also the voltage limit ellipses are heavily distorted.

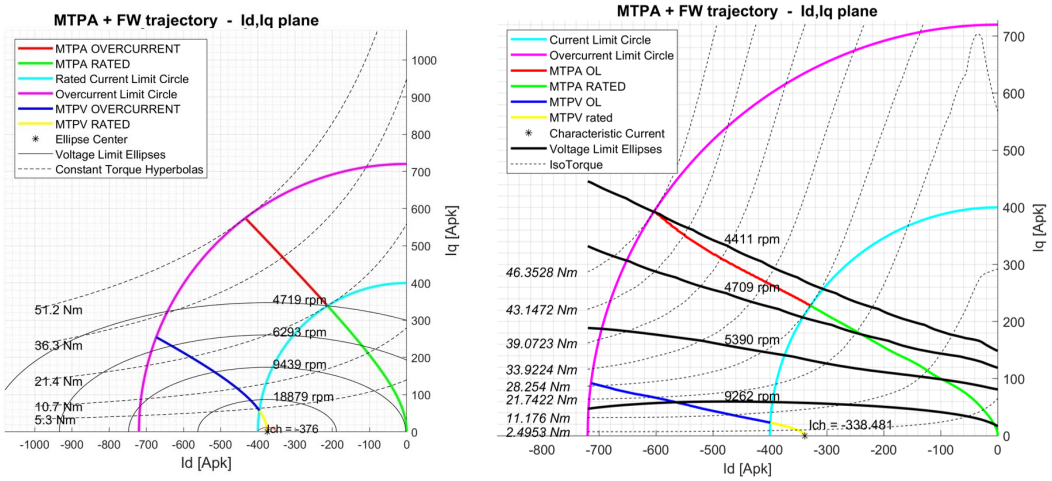

(a) **(b)**

Figure 2.1: MTPA, FW and MTPV trajectories with constant $d-q$ inductances (a) and with variable $d-q$ inductances computed with frozen permeability method (b) [1].

The control of IPM machines, even when operating under Maximum Torque per Ampere (MTPA) conditions, may be difficult to implement because of the pronounced nonlinear magnetic behavior of the machine. In particular, the inductances are

strongly dependent on the stator current components, owing to the saturation of the iron core. Therefore, the d- and q-axis inductances cannot be assumed constant, but vary with the operating point, making the machine model inherently nonlinear. This nonlinearity significantly affects the accuracy of the control strategy, since MTPA operation requires precise knowledge of the machine parameters to generate the optimal current references. Neglecting saturation effects may result in inaccurate torque estimation, suboptimal current trajectories, and a reduction in overall drive performance.

Consequently, a complete magnetic model of the machine is essential for the proper simulation and implementation of the control loops, as it allows the flux-current relationships and the cross-saturation effects to be represented with sufficient accuracy.

In [2], [3] and [4] the impact of cross saturation effect in synchronous reluctance machines is exposed and the importance of taking it into account during the control design of the machine is highlighted.

The importance of a complete magnetic model was also highlighted in [5] where the inductances maps are used to optimize the control of IPM motors with the purpose of increasing the robustness of the PI controller and reducing the mismatch between the control and the motor model. A comparison between different model of IPM machines can be found in [6], [7], [8] and [9].

A model based on the magnetic flux of the machine can be an alternative approach, as shown in [10], but it is less suitable to develop an equivalent circuit model based on electrical lumped-parameter, so in the following a model employing variable inductances will be presented.

Taking into account the analytical considerations exposed before, it is possible to build a model for fast simulation of electrical machines. In this case, the model was built in PLECS® environment. The proposed approach uses the apparent inductance maps on i_d and i_q axes that can be computed by 2D FEA using the frozen permeability method.

2.2 The Reference IPM Machine and 2D-FEA

The reference IPM machine is shown in Figure 2.2 and the main motor data are reported in Table 2.1. The motor considered as a reference is a 24 slots 8 poles IPM machine.

Table 2.1: Motor and Inverter Parameters.

Name	Symbol	Value	Unit
Pole Pairs Number	p	4	-
Slot Number	Q	24	-
Stator Resistance	R_s	1.8	$m\Omega$
Synchronous inductance	L_s	0.025	mH
Voltage constant	k_e	8.25	$V/krpm$
PM Flux Linkage	λ_{PM}	0.024	Vs
Rated Torque	T_n	12	Nm
Rated Current	I_n	110	A_{pk}
DC BUS Voltage	V_{DC}	48	V
Rated Speed	ω_n	3500	rpm

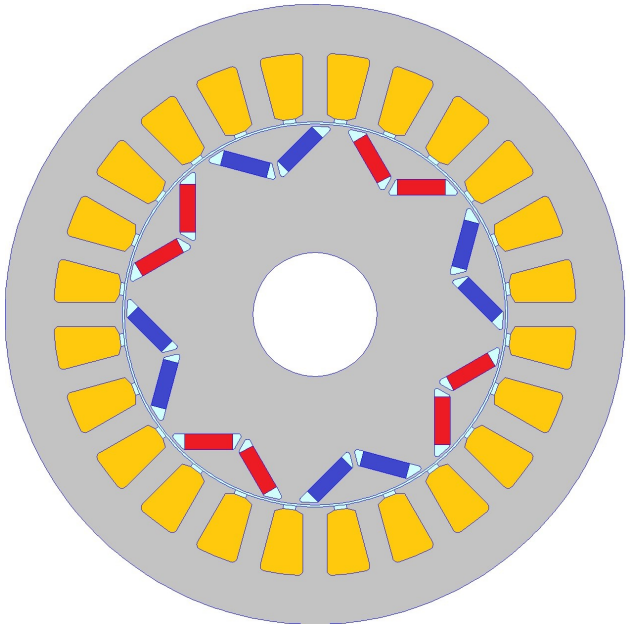

Figure 2.2: Reference motor.

The main data reported in Table 2.1 would be enough to simulate a simple linear model of the machine. Nevertheless, this would not include in the simulation all the

non linearities that characterize the effective behaviour of the machine.

Some 2D FEA simulations are performed to obtain the data necessary to build an accurate dynamic model such as flux and inductance map.

The frozen permeability method allows to compute the inductance values of the machine including the flux of the magnets using 2D-FEA as in [11]. The method is composed by two simulation steps: the first one which consist in a non linear load simulation and the second one is a linear load simulation where the flux of the permanent magnet is set to zero.

Figure 2.3 a) and Figure 2.3 b) show respectively the d-axis and the q-axis inductance map of the machine obtained using with frozen permeability method.

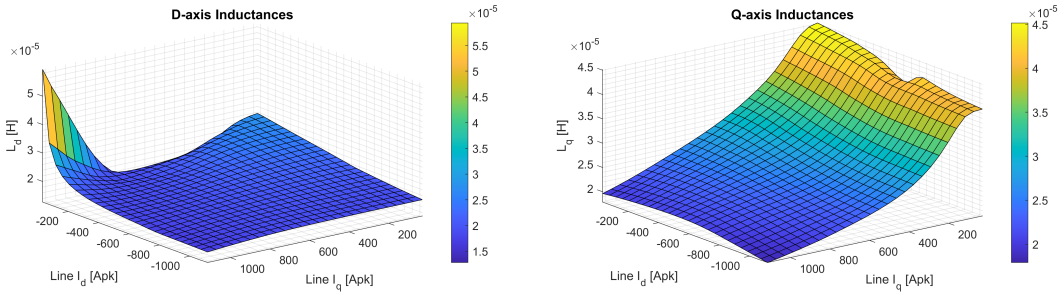

(a) **(b)**

Figure 2.3: L_d (a) and L_q (b) maps obtained via 2D FEA using froze permeability.

2.3 The Model

The electric model of the IPM machine was implemented on a three-phase stationary reference frame. With this approach the circuit is designed with an equivalent star connection of the three phases and each phase is composed by a resistor, a variable inductor, a variable resistor and a voltage source. The voltage source is driven by a Back-EMF block, necessary to model the voltage due to the presence of the permanent magnet.

The lumped circuital model of the IPM machine was implemented in PLECS® following the above description Figure 2.4.

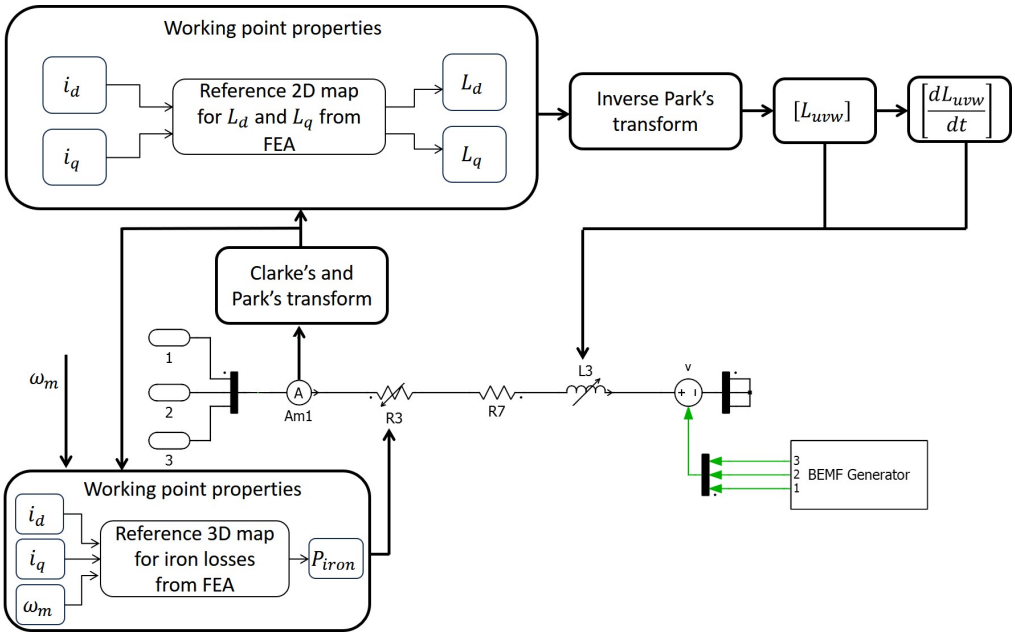

Figure 2.4: PLECS® circuit model.

As shown in Figure 2.4, the model allows to obtain a representation of the dynamic behaviour of the electrical machine thanks to:

- The dynamic update of the phase inductance value and the magnet flux contribution from the maps obtained with 2D FEA for different operating points;
- The modeling of the iron losses of the machine.

In the following, each subsection will deepen different characteristics of the dynamic model.

2.4 Phase Inductance Computation

When a three-phase system is considered the IPM machine inductances matrix can be written including both the auto and the mutual terms with their dependency on the rotor position respect to the stator winding. In (2.1) the phase inductance matrix is reported, where L_σ represents the leakage inductance component, $M_{g0} = -\frac{L_{g0}}{2}$ and M_σ represent the leakage mutual inductance component. Otherwise L_{g0} is the synchronous inductance component and $\hat{L}_{g2}$ is the inductance component due to the anisotropy of the machine, in fact it is multiplied by a sinusoidal waveform depending on the angular position of the rotor.

$$[L_{uvw}] = \begin{bmatrix} L_{g0} + L_\sigma - \hat{L}_{g2}\cos 2\theta_{el} & M_{g0} + M_\sigma - \hat{L}_{g2}\cos 2(\theta_{el} + \frac{2}{3}\pi) & M_{g0} + M_\sigma - \hat{L}_{g2}\cos 2(\theta_{el} - \frac{2}{3}\pi) \\ M_{g0} + M_\sigma - \hat{L}_{g2}\cos 2(\theta_{el} + \frac{2}{3}\pi) & L_{g0} + L_\sigma - \hat{L}_{g2}\cos 2(\theta_{el} - \frac{2}{3}\pi) & M_{g0} + M_\sigma - \hat{L}_{g2}\cos 2\theta_{el} \\ M_{g0} + M_\sigma - \hat{L}_{g2}\cos 2(\theta_{el} - \frac{2}{3}\pi) & M_{g0} + M_\sigma - \hat{L}_{g2}\cos 2\theta_{el} & L_{g0} + L_\sigma - \hat{L}_{g2}\cos 2(\theta_{el} + \frac{2}{3}\pi) \end{bmatrix} \tag{2.1}$$

The flux along d and q axes can be found as a function of inductances and currents according to (2.2) and (2.3).

$$\frac{d\Psi_d}{dt} = L_d\frac{\partial i_d}{dt} + \frac{\partial L_d}{dt}i_d \tag{2.2}$$

$$\frac{d\Psi_q}{dt} = L_q\frac{\partial i_q}{dt} + \frac{\partial L_q}{dt}i_q \tag{2.3}$$

The flux depends on the inductance value and its derivative with respect to the time, so this component must be evaluated. Each component of the matrix reported in (2.1) is derived with respect to the electric angle and, then, everything is multiplied by the electric speed, as in (2.4).

$$\left[\frac{dL_{uvw}}{dt}\right] = 2\omega_{el}\hat{L}_{g2}\begin{bmatrix} \sin 2\theta_{el} & \sin 2(\theta_{el} + \frac{2}{3}\pi) & \sin 2(\theta_{el} - \frac{2}{3}\pi) \\ \sin 2(\theta_{el} + \frac{2}{3}\pi) & \sin 2(\theta_{el} - \frac{2}{3}\pi) & \sin 2\theta_{el} \\ \sin 2(\theta_{el} - \frac{2}{3}\pi) & \sin 2\theta_{el} & \sin 2(\theta_{el} + \frac{2}{3}\pi) \end{bmatrix} \tag{2.4}$$

The implemented model is in the $d-q$ reference frame, so Clarke's and Park's transformations should be adopted to find correlation between the phase inductances just defined and the $d-q$ inductances.

At first the inductance on $\alpha-\beta$ reference frame are computed using Clarke's transformation matrix, according to (2.5).

Then Park's transformation matrix is used to pass from $\alpha-\beta$ reference frame to $d-q$ reference frame.

$$[L_s]_{\alpha\beta} = \begin{bmatrix} \frac{3}{2}L_{g0} + L_\sigma - \frac{3}{2}\hat{L}_{g2}\cos 2\theta_{el} & -\frac{3}{2}\sin 2\theta_{el} \\ -\frac{3}{2}\sin 2\theta_{el} & \frac{3}{2}L_{g0} + L_\sigma + \frac{3}{2}\hat{L}_{g2}\cos 2\theta_{el} \end{bmatrix} \tag{2.5}$$

$$[L_s]_{dq} = \begin{bmatrix} \frac{3}{2}L_{g0} + L_\sigma - \frac{3}{2}\hat{L}_{g2} & 0 \\ 0 & \frac{3}{2}L_{g0} + L_\sigma + \frac{3}{2}\hat{L}_{g2} \end{bmatrix} \tag{2.6}$$

According to Clarke's and Park's transformations, it is possible to find a direct relation between the inductance on d and q axes and the main inductance components that allow to define the inductance value on the original three phase system.

$$L_{g0} = \frac{L_d + L_q}{3} \tag{2.7}$$

$$\hat{L}_{g2} = \frac{L_d - L_q}{3} \tag{2.8}$$

Thanks to (2.7) and (2.8) an immediate relationship between phase and $d-q$ inductances is found. The $d-q$ maps can be integrated with the model in order to select depending on the current value of the motor the correct $d-q$ inductance and computing the auto and mutual inductance components for the modeling, without neglecting the inductive coupling between each phase and updating dynamically the inductance value according to 2D-FEA results.

PLECS® allows to use a variable inductor [12] which needs as input values the complete inductance matrix and its derivative with respect to the time. In this way also the cross saturation effect is considered in the modeling. In the logical part of the model the computation of the inductance matrix is implemented, starting from the inductance values on d and q axes given from the maps obtained with 2D-FEA.

In Figure 2.5 and 2.6 the stator currents obtained from simulations results with a torque load applied at 0.2 s are shown. The difference between the currents in transient conditions is evident.

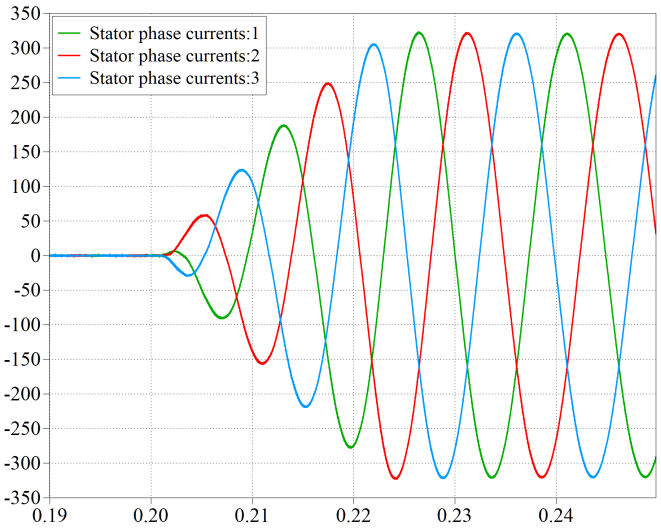

Figure 2.5: Stator currents with constant inductance model.

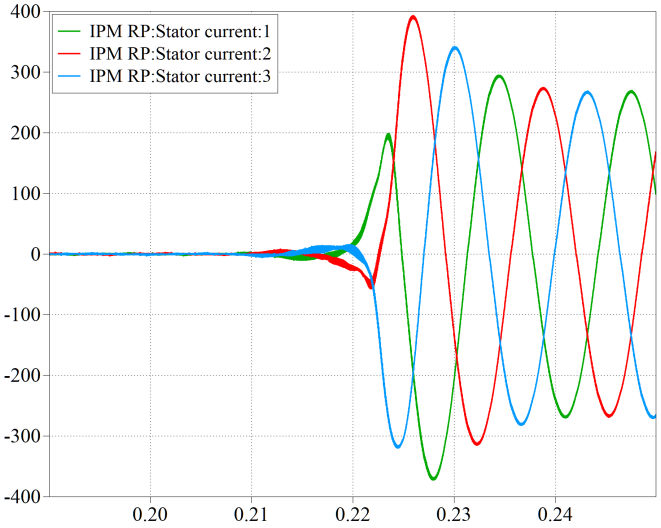

Figure 2.6: Stator currents with the proposed variable inductance model.

2.5 *d* Axis Flux Evaluation

The model is inductance based, so to introduce correctly the flux generated by the permanent magnets it is appropriate to evaluate it with 2D FEA. Thanks to the performed simulations, the flux map on d and q axes with permanent magnets on

and off can be found. The permanent magnets flux contribution is on d axis, so the variation on d axis flux obtained with and without the magnets can be introduced in the model to evaluate correctly permanent magnets contribution.

Figure 2.7 shows the difference between the theoretical permanent magnets flux contribution and the effective variation on d axis flux when magnets are involved or neglected.

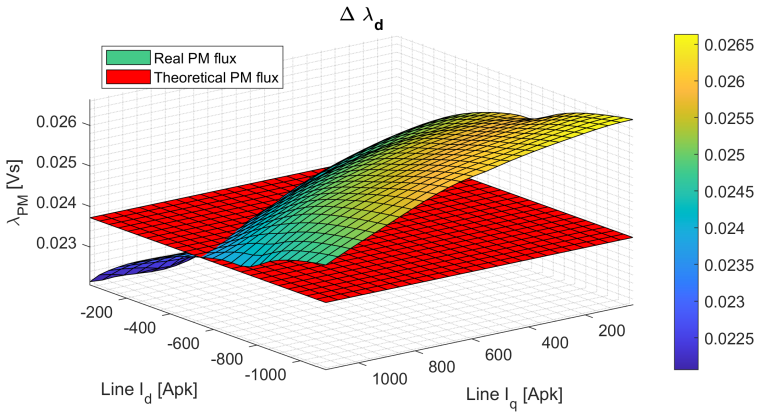

Figure 2.7: Theoretical permanent magnets flux (in red) and effective variation on d axis flux with magnets on and off (colored map).

The effective variation on d axis flux is not constant, so the map representing this variable is introduced in the model in order to evaluate correctly the total d axis flux and the torque.

Using the map representing the λ_{PM} contribution, the total flux on d and the torque can be computed in the model.

$$\Lambda_d = L_d i_d + \lambda_{PM} \tag{2.9}$$

$$T = \frac{3}{2}\left[\left(L_d - L_q\right) i_d i_q + \lambda_{PM}\right] \tag{2.10}$$

The computed electromagnetic torque is used in the mechanical part of the model, where the inertia of the rotor and friction are introduced.

2.6 Iron Losses Model

Iron losses represent a crucial aspect in the analysis and modeling of electric motors, and their contribution should be properly taken into account in any accurate analytical formulation. These losses originate in the magnetic core of the machine and are mainly associated with hysteresis and eddy-current phenomena, both of which arise from the time-varying magnetic field within the ferromagnetic material. Their magnitude is strongly influenced by the operating conditions of the machine, and in particular by the electrical frequency. As the electrical frequency increases, the periodic magnetization and demagnetization of the core occur more rapidly, resulting in a substantial growth of the associated losses.

This effect becomes particularly relevant in high-speed applications, where the electrical frequency can reach very high values. In such conditions, iron losses may no longer be regarded as a secondary contribution, but instead become a significant component of the total power losses of the machine. In particular, eddy-current losses exhibit a quadratic dependence on frequency, making them increase very rapidly as the operating frequency rises. Consequently, neglecting iron losses in the analytical model may lead to an underestimation of the total losses, an overestimation of efficiency, and a less accurate prediction of the machine thermal behavior.

For these reasons, the inclusion of iron losses in the analytical modeling of electric motors is essential, especially when the machine is intended to operate over a wide speed range or at elevated frequencies. A proper representation of these losses allows a more realistic evaluation of machine performance, efficiency, and thermal loading, thus improving both the design process and the reliability of the overall model.

In simplified models, iron losses are often neglected; however, when they are non-negligible, it is essential to account for them in the analytical formulation in order to achieve a motor simulation that accurately reflects real operating conditions. In particular, it is important to model their voltage drop. It is fundamental that the global phase-to-phase voltage is modeled in order to verify that the DC BUS voltage can power correctly the machine.

In this case a variable resistor, always from PLECS® library [12], is used. The resistance value is updated dynamically depending on the working point of the

machine, identified by the current on d and q axes and the mechanical speed of the rotor. A 3D map of the losses trend as a function of d and q current and the mechanical speed of the rotor is found from 2D FEA simulations and given as an input to the model.

The model defines a 3D lookup table of the losses values and compute dynamically the losses in the operating point. These losses are assumed as the power dissipated by the variable resistor introduced in the machine model. The current flowing in each phase is measured from the ammeter, so the resistance value is computed. Figure 2.8 shows the 3D maps used for iron losses representation for the motor under analysis.

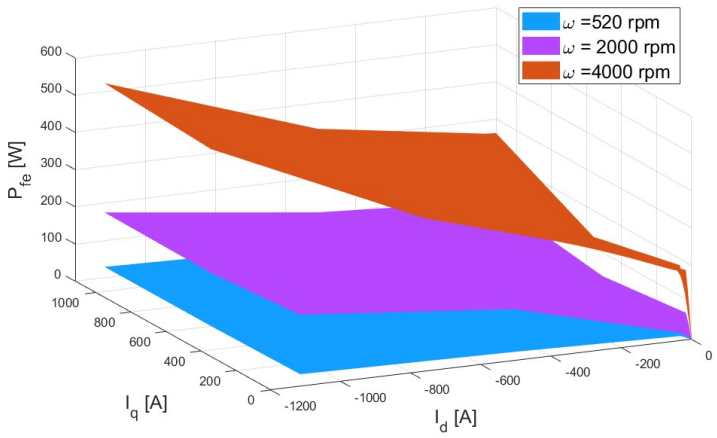

Figure 2.8: Iron losses map obtained as a function of the current value on d and q axes and the speed.

The introduction of the iron losses map at different speed values allows to represent the voltage drop of the machine due to the iron losses. Generally, this voltage contribution is neglected, but in some cases, especially at high speed, this component can become quite high with respect to the voltage in input from the DC BUS.

Figure 2.9 and Figure 2.10 show the phase voltage of the machine obtained, respectively, including and neglecting the iron losses. According to simulations results, the voltage drop has an increment of about 5 V when the iron losses are introduced in the model.

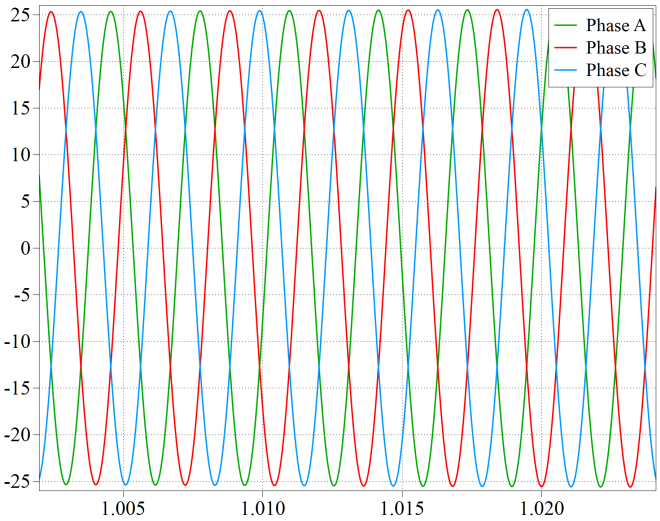

Figure 2.9: Phase voltage neglecting the iron losses at 3500 rpm.

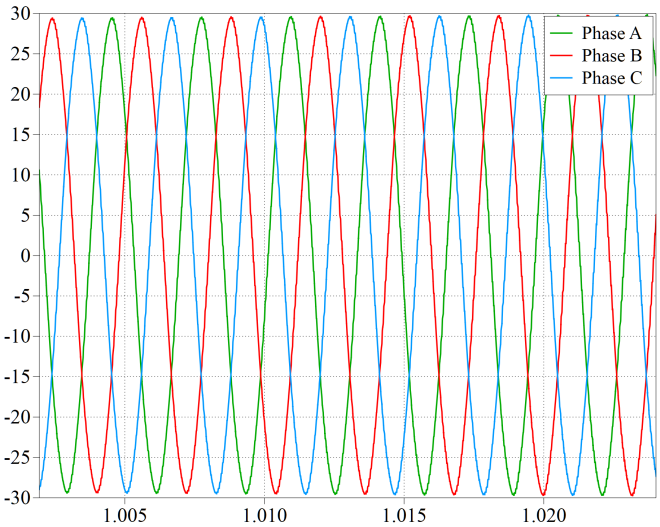

Figure 2.10: Phase voltage including the iron losses at 3500 rpm.

2.7 Global Model

All the equations seen before are implemented in the IPM machine model. Figure 2.11 shows the model implemented in PLECS®and the necessary input data.

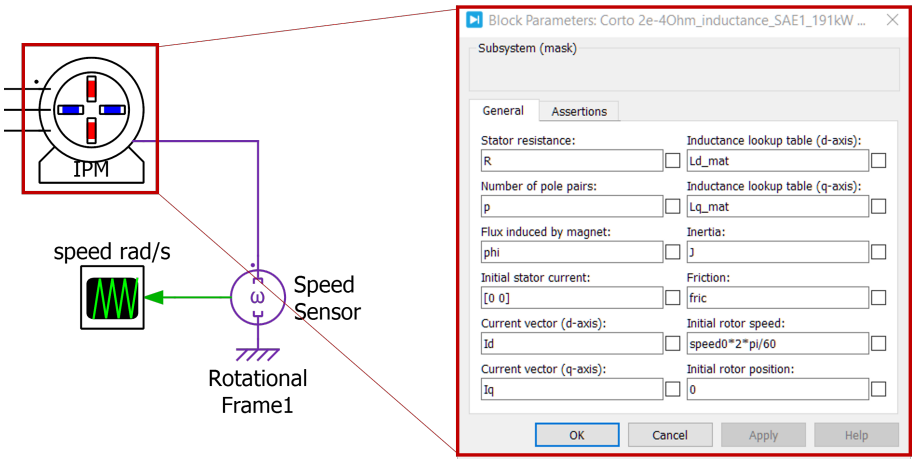

Figure 2.11: IPM machine model: required input data.

The IPM machine model, shown in Figure 2.12, consists of three main parts:

- an electrical circuit, which simulates the electrical connections of the machines;
- two logical subsystems, one for the computation of the BEMF generated by the voltage sources and the other one for the computation of the phase inductances;
- a mechanical part.

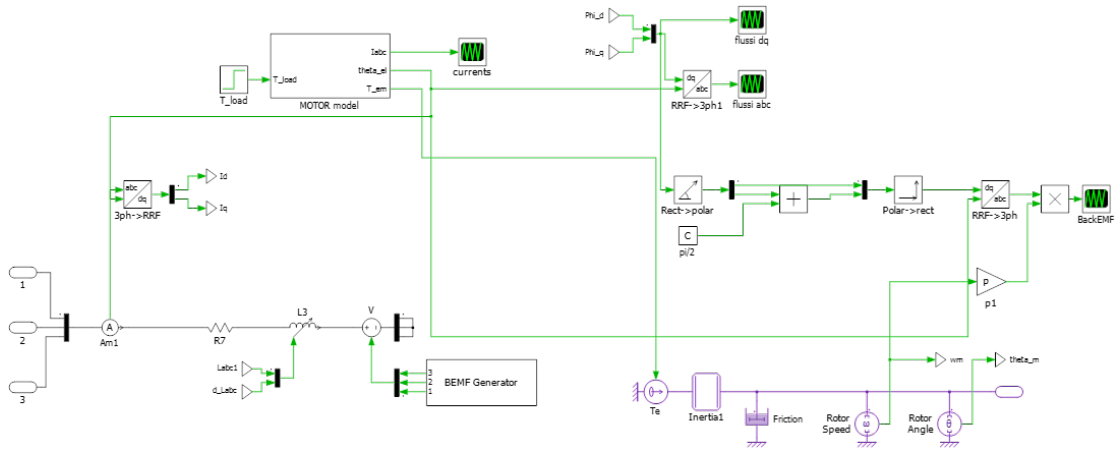

Figure 2.12: IPM machine model.

Inside the motor model subsystem, the computation of the inductances is implemented. Then, thanks to the current signal measured in the electrical circuit the *d*-*q* flux and the electrical torque are computed.

The logical part of the model allows also to compute the Back-EMF, the torque, the fluxes on d and q axes of the motor. Thanks to the dynamic model adopted, the torque computation is obtained taking into account the saturation effects, getting

an accurate evaluation of the global machine's performance.

Moreover, there is a mechanical part which allows to introduce motor inertia and friction in order to compute the motor rotational speed.

2.8 Experimental Validation

The obtained simulations' results are validated experimentally with the motor under analysis. Figure 2.13 shows the test bench used for the experimental validation.

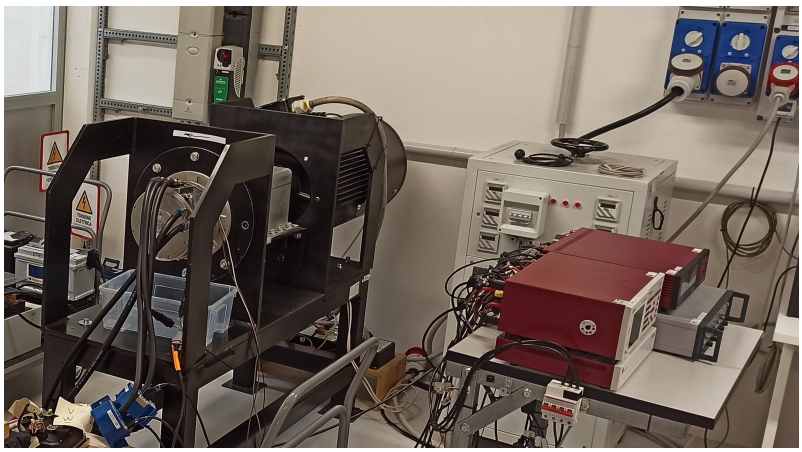

Figure 2.13: Motor test bench.

Table 2.2 resumes the phase-to-phase voltage values obtained from simulations with and without the iron losses model integration and experimental measurements at different speed values.

Table 2.2: Experimental and simulations results comparison.

Speed $[rpm]$	**Peak voltage from simulations with iron losses** $[V]$	**Peak voltage from experimental**$[V]$
1750	30	30.3
2500	38	37
3000	38.8	37.5
4000	39	38

According to experimental measurements the phase-to-phase voltage value obtained is very similar to the one obtained in simulations with the model adopted, considering the same operating point.

2.9 Conclusions

This chapter presented an inductance based lumped-parameter dynamic model for IPM machines considering iron losses.

Thanks to the dynamic update of the inductance values and permanent magnet flux in the machine, the dynamic model allows to take into account iron saturation, magnets working points and cross saturation effect on the $d-q$ axes.

The input data set of the model are easily computed by means of 2D FEA, employing frozen permeability method. The model inputs are based on $d-q$ reference frame equations.

The magnetic model is implemented with a variable inductance matrix and the iron losses are modelled with a variable resistors put in series in each phase.

Generally iron losses are represented with an equivalent resistor in parallel, actually what can be measured on a real setup is an increase of the voltage drop across the motor terminals when the iron losses increases, while there is no change in the motor phase currents.

The iron losses maps for different operating points (i.e. i_d i_q points) at different speed values are computed with 2D FEA. The maps are introduced in the model in a 3D lookup table: in this way for each operating point at a specific speed, the right losses value is considered. The iron losses value computed via 3D lookup table is the power dissipated by the variable resistor and then according to the Ohm's law and the instantaneous phase currents is converted in an equivalent resistance.

The model was validated on a reference machine and the experimental results are in good agreement with the model ones.

2.10 References

[1] C. Bianchini, G. Bisceglie, A. Torreggiani, *et al.*, «Effects of the magnetic model of interior permanent magnet machine on mtpa, flux weakening and mtpv evaluation», *Machines*, vol. 11, no. 1, 2023, ISSN: 2075-1702. DOI: 10.3390/machines11010077. [Online]. Available: https://www.mdpi.com/2075-1702/11/1/77.

[2] A. Vagati, M. Pastorelli, F. Scapino, and G. Franceschini, «Impact of cross saturation in synchronous reluctance motors of the transverse-laminated type», *IEEE Transactions on Industry Applications*, vol. 36, no. 4, pp. 1039–1046, 2000. DOI: 10.1109/28.855958.

[3] A. Vagati, M. Pastorelli, and G. Franceschini, «Effect of magnetic cross-coupling in synchronous reluctance motors», 1997. [Online]. Available: https://api.semanticscholar.org/CorpusID:118823837.

[4] A. Colotti and K. S. Stadler, «Magnetic cross-coupling effects on the performance of the synchronous reluctance machine», in *2014 16th European Conference on Power Electronics and Applications*, 2014, pp. 1–10. DOI: 10.1109/EPE.2014.6910730.

[5] F. Husnayain, T. Noguchi, K. Iwama, and F. Yusivar, «Mismatch reduction using 2-d inductance map for robust vector control of ipm motor», in *2021 17th International Conference on Quality in Research (QIR): International Symposium on Electrical and Computer Engineering*, 2021, pp. 90–93. DOI: 10.1109/QIR54354.2021.9716174.

[6] T. Jerčić and D. Žarko, «A survey of permanent magnet synchronous machine models suitable for computer simulation», in *2017 19th International Conference on Electrical Drives and Power Electronics (EDPE)*, 2017, pp. 307–312. DOI: 10.1109/EDPE.2017.8123251.

[7] Y. Mao, H. Yang, S. Lyu, H. Lin, H. Zhan, and C. Liu, «Dynamic modeling for asymmetric interior pm machine with consideration of magnetic saturation and cross-coupling effect», in *2023 IEEE Energy Conversion Congress and Exposition (ECCE)*, 2023, pp. 4966–4971. DOI: 10.1109/ECCE53617.2023.10362900.

[8] M. Li, X. Chen, and Y. Lei, «Research on simulation modeling of permanent magnet synchronous motor based on variable parameters», in *2021 China Automation Congress (CAC)*, 2021, pp. 6199–6204. DOI: 10.1109/CAC53003.2021.9728641.

[9] Y.-S. Park, M.-M. Koo, S.-M. Jang, J.-Y. Choi, and D.-J. You, «Dynamic characteristic analysis of interior permanent magnet synchronous motor considering varied parameters by outer disturbance based on electromagnetic field analysis», *IEEE Transactions on Magnetics*, vol. 50, no. 11, pp. 1–4, 2014. DOI: 10.1109/TMAG.2014.2323344.

[10] G. Weidenholzer, S. Silber, G. Jungmayr, G. Bramerdorfer, H. Grabner, and W. Amrhein, «A flux-based pmsm motor model using rbf interpolation for time-stepping simulations», in *2013 International Electric Machines & Drives Conference*, 2013, pp. 1418–1423. DOI: 10.1109/IEMDC.2013.6556323.

[11] J. Walker, D. Dorrell, and C. Cossar, «Flux-linkage calculation in permanent-magnet motors using the frozen permeabilities method», *IEEE Transactions on Magnetics*, vol. 41, no. 10, pp. 3946–3948, 2005. DOI: 10.1109/TMAG.2005.854973.

[12] Plexim, *The simulation platform for power electronic systems - user manual version 4.8.1*, 2024.

3. Electrical Machines Design and Optimization

The optimization of electric motors has become a critical field of research and development in light of growing efficiency requirements, sustainability goals, and increasingly demanding performance specifications. Modern applications, spanning from industrial automation to electric vehicles, require machines that not only deliver high power and torque but also maintain minimal losses, high reliability, and competitive cost.

Building upon the theoretical foundation of synchronous motor modeling established in the previous chapter, this chapter shifts the focus from the analytical representation of electromagnetic behavior to the systematic design optimization of the machine. While the previous chapter detailed how non-linearities and flux linkages define the motor's operation, this stage focuses on determining the optimal physical dimensions, specifically the stator diameter and stack length, required to meet specific performance targets.

The purpose of this method is to find the minimum stack length for a given set of stator outer diameters that ensures the desired performance while respecting the thermal equilibrium of the machine. By integrating iron losses into the analytical sizing loop, the model provides a robust tool for early-stage design.

The following sections describe the fundamental performance metrics, the main categories of design variables (geometric, electromagnetic, and thermal), and the application of the framework to a case study. This optimization process highlights the inherent geometric and thermal constraints of conventional motor architectures, setting the stage for the advanced manufacturing solutions discussed later in this thesis.

The application of the framework to a case study motor is presented, highlighting how optimization leads to significant improvements in terms of efficiency and weight reduction.

3.1 General Overview

As weight and mass reduction becomes evermore a crucial objective in transport applications such as aerospace, marine and traction, the need for higher power density electrical machines is becoming ever more important [1], [2].

Electrification efforts over the whole transport industry have in the past few decades, achieved very important improvements of system and sub-system performances, such as efficiency and power density. In the aerospace industry, the more electric [3] and the all electric [4] aircraft initiatives have resulted in modern aircraft employing electric systems that can improve improve efficiency, emissions, reliability, and maintenance costs [5]. For traction applications, the need for high performance, high efficiency and at the same time cost-effective traction electrical machines has resulted in the development of compact electric drives with a high level of torque per volume ratio [6], [7].

In maritime operations, traditional diesel engines are however much more common among the majority of the applications. The concept of turbo-electric systems has been used in marine applications for decades [8]. While being highly consolidated and proven to be the most efficient system to date, however the inclusion of internal combustion engines still results in a significant environmental impact [9].

In fact, fully and/or hybrid electric propulsion has also become an interesting solution to transform the maritime industry [10]. Typical examples of hybrid solutions are given in [11], which presents two different design criteria, namely:

- one aiming to ensure that the engine-generator group runs at fixed speed and power;
- another focusing on variable power and speed operation points.

In all these applications, the performance and quality of the electric drive is paramount. In particular, electrical machines with a high power density is critical [12]. In [13] a design method for a stator core shape for an improvement in power density of a small surface-mounted permanent magnet (SPM) motor is proposed. The stator core shape design method improves the machine's power density by reducing the machine weight without compromising the operational torque.

3.2 Analytical Design of the Reference Machine

The requirements for the reference machine are reported in Table 3.1.

Table 3.1: Requirements

Parameter	Symbol	Value	Unit
Nominal power	P_m	10	kW
Nominal speed	n	6000	rpm
DC BUS voltage	V_{DC}	48	V
Power density	P_{den}	2	kW/kg
Number of phases	m	3	-

Due to the nominal operating speed, the number of pole pairs p is fixed at six. The operating frequency at the nominal working point would be found according to (3.1).

$$f = \frac{pn}{60} = 600 \tag{3.1}$$

At this operating frequency iron, AC and magnet losses becomes consistent. To mitigate the amount of iron losses a M250 or NO20 lamination is recommended; hereafter, for the analytical design procedure an M250 lamination is chosen.

Regarding the magnets, NdFeB N42SH are chosen for the analytical design procedure. Considering the operating frequency at nominal conditions, a segmentation will be recommended to mitigate magnet losses.

Since the motor will be cooled with natural air convection, a desired value for the current density j_{rms} inside the slot is 6 A/mm^2 with a slot filling factor of 0.4.

The analytical procedure considered for the design of the reference machine is the one reported in [14].

The airgap flux density at noload B_{g0} for SPM machines can be found as in (3.2), where B_{rem} is the remainance of the magnet, μ_{rel} is the relative permeability of the magnet and t_m is the magnet thickness.

$$B_{g0} = \frac{B_{rem}}{1 + \frac{\mu_{rel} g}{t_m}} \tag{3.2}$$

Considering that generally the ratio $t_m/g \approx 3 \div 6$ it can be taken as a first approximation $B_{g0} \approx 0.75 B_{rem}$.

The desired torque at nominal power can be computed according to (3.3).

$$T = \frac{P_n}{n \frac{2\pi}{60}} \tag{3.3}$$

As known, the torque can also be expressed as in (3.4), where k_w is the winding factor, $\hat{K}_s$ is the peak electric load, $\hat{B}_{g1}$ is the first harmonic flux density in the airgap and L_{stk} is the stack length.

$$T = \frac{\pi}{\sqrt{2}} k_w \hat{K}_s \hat{B}_{g1} \frac{\pi}{4} D_g^2 L_{stk} \tag{3.4}$$

The electric load represents the current that is distributed on the airgap and can be found according to (3.5).

$$\hat{K}_s = \frac{3 k_w N_s \sqrt{2} I}{\pi D_i} \tag{3.5}$$

Dividing the numerator and the denominator for Q, another expression for the electric load can be found.

$$\hat{K}_s = \frac{k_w I_{slot}}{p_s} \tag{3.6}$$

Generally the electric load stays between 30 and 100 kA/m.

The first harmonic flux density can be found as in (), where B_{g0} is the magnetic

load in the airgap and α_m^e is the electric angle spanned by the magnet.

$$\hat{B}_{g1} = \frac{4}{\pi} B_{g0} \sin \alpha_m^e \tag{3.7}$$

The magnetic load depends on the iron saturation and generally it stays between 0.7 T and 1 T.

The ratio between the stack length L_{stk} and the airgap diameter D_g can be found according to the empirical equation reported in (3.8).

$$\frac{L_{stk}}{D_g} = \frac{1 \div 2.3}{\sqrt{2p}} \tag{3.8}$$

Here, $\frac{L_{stk}}{D_g} = \frac{1.2}{\sqrt{2p}}$ is chosen.

Considering the variation of flux density due to the current reported in (3.9).

$$\Delta B_s = \mu_0 \delta H_s = \mu_0 \frac{\hat{K}_s D_g}{2p\left(g + \frac{t_m}{\mu_{rel}}\right)} \tag{3.9}$$

And knowing that the magnet thickness is expressed according to (3.10), where μ_{rel} is the relative permeability of the magnet, $g'' = g k_c k_{sat}$ is the equivalent airgap which take into account the Carter's coefficient $k_c \approx 1.1$ and the saturation coefficient $k_{sat} \approx 1.2$.

$$t_m = \mu_{rel} g'' \frac{B_{g0}}{B_{rem} - B_{g0}} \approx 4mm \tag{3.10}$$

It is possible to find the electric load, the airgap diameter and the stack length.

The stator design starts with the definition of the slot pitch according to the empirical equation reported in (3.11), where D_g is expressed in mm.

$$p_s = 1.6\sqrt{\frac{D_g}{p}} \tag{3.11}$$

Then the number of slots is obtained as in (3.12).

$$Q = \frac{\pi D_g}{p_s} \tag{3.12}$$

Then the number of slots per pole per phase can be computed as shown in (3.13).

$$q = \frac{Q}{m2p} \tag{3.13}$$

So, $q = 0.5$ is chosen and the number of slots and the slot pitch are computed as a consequence.

Imposing a desired flux density in the tooth, the tooth width can be computed as in (3.21), where $B_t = 1.6T$ is the desired flux density in the tooth and $c_s = 0.96$ is the stacking factor.

$$w_t = \frac{B_{g0} + \delta B_s}{B_t} p_s c_s \tag{3.14}$$

In the same way the back iron thickness can be found, starting with the computation of the magnetic flux through the back iron as a function of the total flux at load conditions ϕ_{load}, as shown in (5.24), where α_m is the angle spanned by the magnet.

$$\phi_{bi} = \frac{\phi_{load}}{2} = \frac{1}{2}\left(B_g \alpha_m D_g L_{stk} + \Delta B_s \frac{D_g L_{stk}}{p}\right) \tag{3.15}$$

Consequently, considering a flux density in the back iron $B_{bi} = 1.3T$, the back iron thickness is found according to (3.16).

$$h_{bi} = \frac{\phi_{bi}}{B_{bi} L_{stk} c_s} \tag{3.16}$$

Then the slot surface must be computed in order to obtain the external diameter of the machine. The rms phase current necessary for the torque generation is found as in (3.17), where N_{ph} is the number of turns per phase.

$$I_m = \frac{\pi}{3} \frac{D_g \hat{K}_s}{k_w N_{ph} \sqrt{2}} \tag{3.17}$$

Fixing a desired current density j_{rms} of 6 A/mm^2 with a slot filling factor of 0.4 and considering 6 parallel connections, the slot surface can be found according to (3.18), where n_{cs} is the equivalent number of conductors in series per slot.

$$S_{slot} = n_{cs} \frac{I_m}{j_{rms}} \tag{3.18}$$

From this the slot dimensions can be found and, then the outer stator diameter can be obtained as shown in (3.19).

$$D_e = D_g + 2h_s + 2h_{bi} = 148mm \tag{3.19}$$

3.3 Analytical Volume Minimization

For a lot of applications maximizing the power density of the motor is the main task. So one of the key point is to obtain the desired performance from the machine with the minimum volume.

The analytical procedure reported hereafter allow to find the minimum stack length of a motor to reach the desired performance. This procedure can be applied considering different external stator diameter.

The analytical procedure considers also the iron losses: starting from a reference machine, the iron losses of this machine are computed via preliminary 2D FEA simulations or they can be estimated analytically.

Figure 3.1 shows a flowchart of the proposed optimization method.

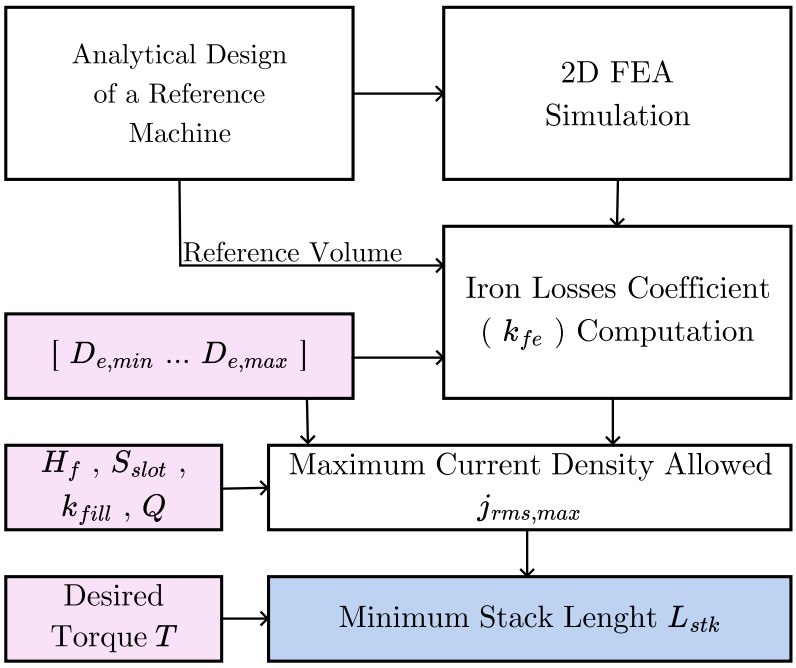

Figure 3.1: Flowchart of the proposed optimization process.

The data of the reference motor are reported in Table 3.2.

Table 3.2: Reference Motor Data

Parameter	Symbol	Value	Unit
Stator outer diameter	$D_{e,ref}$	148	mm
Airgap diameter	$D_{g,ref}$	98	mm
Stack length	$L_{stk,ref}$	34	mm
Current density	$j_{rms,ref}$	6	$\frac{A}{mm^2}$
Torque	T_{ref}	17.7	Nm
Joule losses	$P_{j,ref}$	166	W
Iron losses	$P_{i,ref}$	262	W

The main input for the analytical process are resumed in Table 3.3.

Table 3.3: Reference Motor Data

Parameter	Symbol	Value	Unit
Desired torque	T	16	Nm
Heat flow coefficient	H_f	2300	$\frac{W}{m^2}$
Stator outer diameter vector	D_e	[100 ... 160]	mm
Diameters ratio	D_{ratio}	0.65	–
Magnetic load	$\hat{B}_g$	0.9	T
Tooth induction	$\hat{B}_t$	1.7	T
Stator yoke induction	$\hat{B}_{bi}$	1.5	W
Slot filling factor	k_{fill}	0.4	–
Stacking factor	k_{stk}	0.96	–
Polar expansion coefficient	k_{pp}	0.93	–

The flux in the airgap can be expressed according to

$$\Phi_g = \hat{B}_g \pi D_g L_{stk} \tag{3.20}$$

Where D_g and L_{stk} are respectively the airgap diameter and the stack length of the optimized machine. So the tooth width and the stator yoke can be found considering the desired operating point.

$$w_t = \frac{\Phi_g}{\hat{B}_t L_{stk} k_{stk} Q} \tag{3.21}$$

Substituting (3.20) in (3.21), the expression of the tooth width is found independently from the stack length. Figure 3.2 (a) shows the resulting teeth width for different stator outer diameters.

$$w_t = \frac{\hat{B}_g \pi D_g}{\hat{B}_t k_{stk} Q} \tag{3.22}$$

The same procedure is applied to find the stator yoke. The results obtained are reported in Figure 3.2 (b).

$$h_{bi} = \frac{\Phi_g}{\hat{B}_{bi} L_{stk} k_{stk} 4p} = \frac{\hat{B}_g \pi D_g}{\hat{B}_{bi} k_{stk} 4p} \tag{3.23}$$

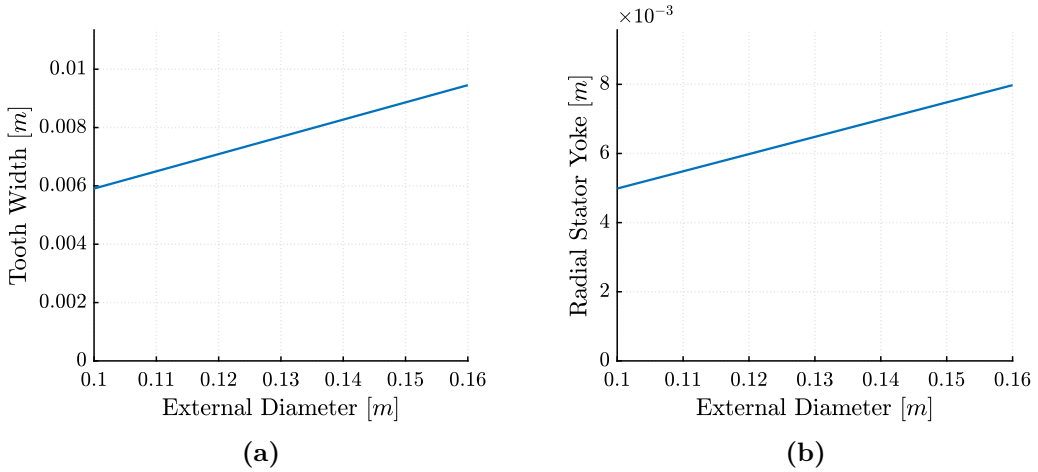

Figure 3.2: Tooth width (a) and stator yoke (b) for different stator outer diameters.

The total stator iron surface can be found summing the total teeth surface and the total surface of the back iron, as shown in (3.24), where $D_b = D_e - 2h_{bi}$ is the diameter at the end of the slot and $D_i = D_g + 2g$ is the inner stator diameter.

$$S_{fe,TOT} = S_{fe,t} + S_{fe,bi} = Q w_t \frac{D_b - D_i}{2} + \pi/4 \left(D_e^2 - D_b^2 \right) \tag{3.24}$$

The slot surface can be found according to (3.25) where $S_{stator} = \frac{\pi}{4} \left(D_e^2 - D_i^2 \right)$ is the total surface of the stator.

$$S_{slot} = \frac{S_{stator}}{Q} \left(1 - \frac{S_{fe,TOT}}{S_{stator}} \right) k_{pp} \tag{3.25}$$

As well known, the joule losses can be expressed as in (3.26).

$$P_j = Q\rho S_{slot} k_{fill} j_{rms}^2 L_{stk} \tag{3.26}$$

This expression neglects the end windings. For this reason this procedure should be applied to concentrated windings.

The iron losses of the machine can be expressed simply as a function of the iron losses obtained from the 2D FEA simulations of the reference machine. An iron losses coefficient k_{fe} is computed to find the iron losses as a function of the length of the stack as shown in (3.27), where $V_{ref} = \frac{D_{e,ref}^2 - D_{i,ref}^2}{4} L_{stk}$ is the stator volume of the reference machine.

$$k_{fe} = \frac{P_{fe,ref}}{V_{ref}} \frac{D_e^2 - D_i^2}{4} \pi \tag{3.27}$$

So, the iron losses can be expressed as in (3.28).

$$P_i = k_{fe} L_{stk} \tag{3.28}$$

The dissipating power of the machine is given by (3.29) where $S_d = k_{al} k_l \pi D_e L_{stk}$ is the dissipating surface of the considered machine.

$$P_d = H_f S_d \tag{3.29}$$

To compute the dissipating surface some coefficients can be added in order to include also the fins and the fact the the length of the frame is major than the stack length. In this case, two coefficient are introduced: k_{al} that take into account the wings of the frame and k_l that increase the stack length accordingly to the frame length.

To respect the thermal equilibrium of the machine, the dissipating power of the machine should be major than the total losses (joule losses and iron losses), as in

(3.30).

$$P_d \geq P_j + P_i \tag{3.30}$$

So, converting the inequality into a mathematical equality, it is possible to find the expression of the maximum rms current density allowed by the machine's thermal limit independently from the stack length, as shown in (3.31).

$$j_{rms,max} = \sqrt{\frac{\pi D_e H_f - k_{fe}}{Q \rho S_{slot} k_{fill}}} \tag{3.31}$$

The trend of the current density as a function of the outer stator diameter is reported in Figure 3.3 (a).

Imposing this current density to the machine, the minimum stack length that allow to obtain the desired torque can be found. Starting from the torque expression, reported in (3.32), the stack length is obtained considering the maximum electric loading $\hat{K}_s$ computed using $j_{rms,max}$, as shown in (3.33).

$$T = \frac{1}{2} \hat{B}_g \hat{K}_s \frac{D_g}{2} D_g \pi L_{stk} \tag{3.32}$$

$$L_{stk} = \frac{2T}{\hat{B}_g \hat{K}_s \frac{D_g}{2} \pi} \tag{3.33}$$

In this way the machine with the minimum volume that allows to obtain the desired performance is found for different stator outer diameters. The resulting stack length are reported in Figure 3.3 (b) as a function of the outer stator diameter. The volume of the machines obtained considering different stator outer diameters is reported in Figure 3.3 (c). A first analytical estimation of the efficiency considering iron and joule losses is reported in Figure 3.3 (d) as a function of the external diameter.

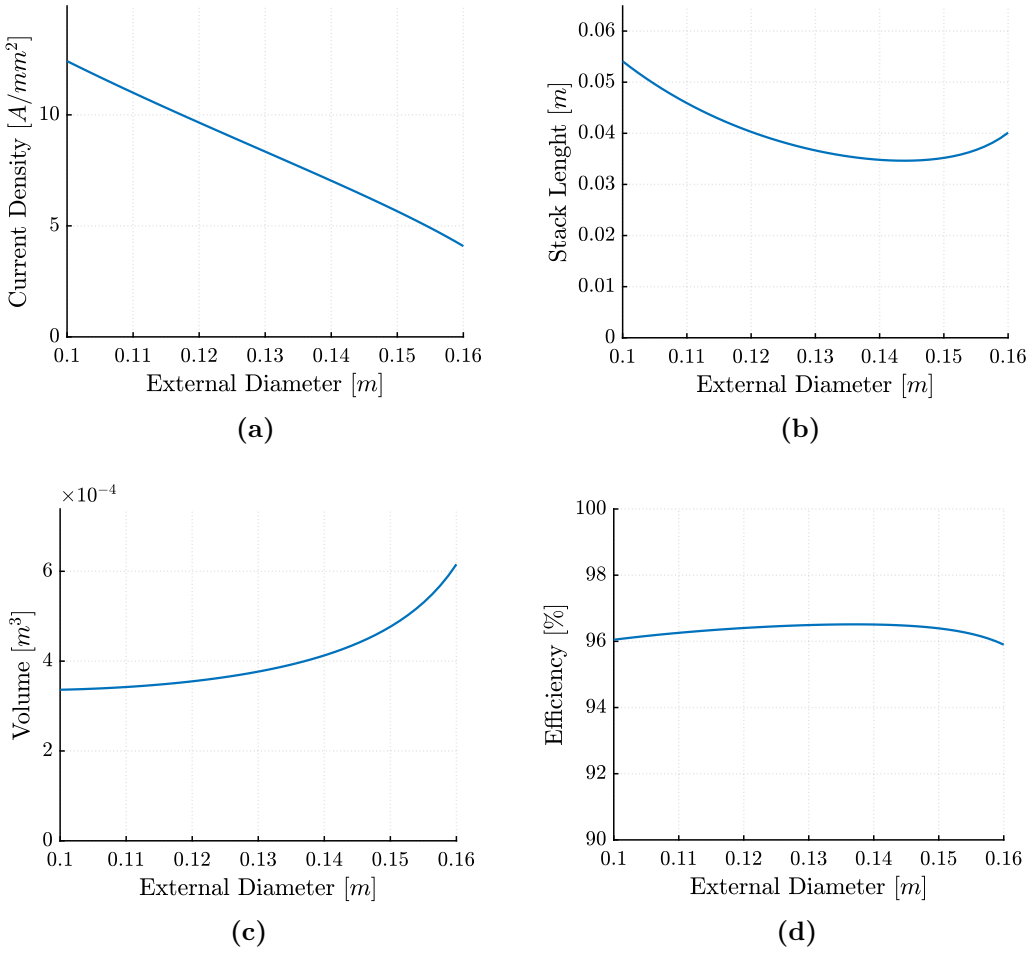

Figure 3.3: Current density (a), stack length (b), volume (c) and efficiency (d) for different stator outer diameters.

With this method a set of thermally feasible machines that allow to obtain the desired performance and minimize the volume is obtained. From these analytical consideration it is evident that the machine volume increase significantly with the outer stator diameter, so the power density is expected to decrease.

3.3.1 2D FEA Validation

In the following the results obtained from the analytical optimization are verified via 2D FEA. The machines simulated are reported in Figure 3.4. The nominal operating point is considered for all the motors.

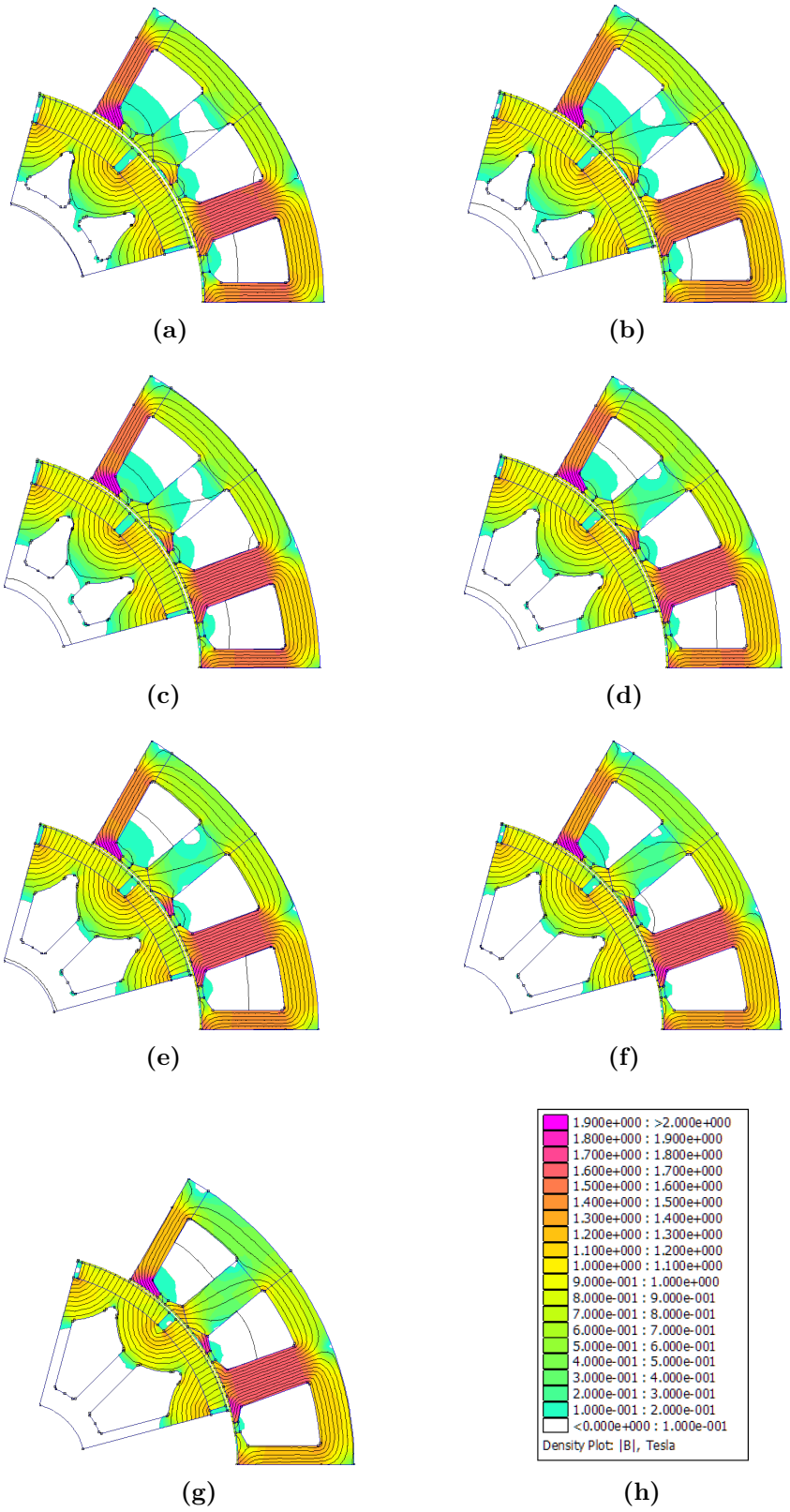

Figure 3.4: Simulated machines: a) $D_e = 100mm$, b) $D_e = 110mm$, c) $D_e = 120mm$, d) $D_e = 130mm$, e) $D_e = 140mm$, f) $D_e = 150mm$, g) $D_e = 160mm$, h) legend.

The iron operating point is the same for every motor, as imposed with the optimization design process.

For each machine the power density is computed. As expected from the analytical optimization, the machines with bigger diameters and shorter stack length have a higher volume, so higher mass (see Figure 3.3 (c)). As a consequence, their power density is lower compared to the ones with lower outer diameter and longer stack, as shown in Figure 3.5 (a).

Nevertheless, the machines with higher power density have lower efficiency and high current density in the slots. Figure 3.5 (b) shows a comparison between the efficiency obtained from the analytical optimization process and 2D FEA simulations.

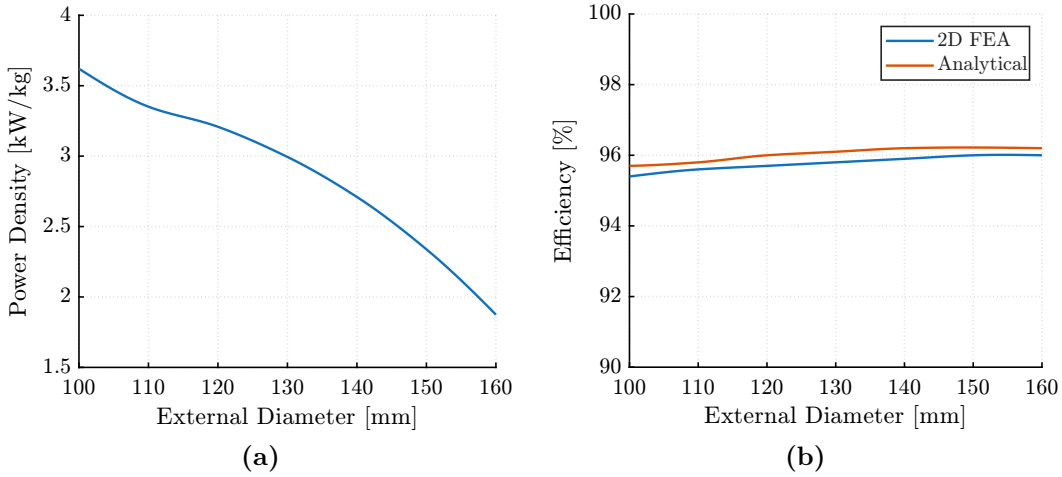

Figure 3.5: Power density (a) and efficiency comparison (b) of each machine for different stator outer diameters from 2D FEA.

Considering all the aspects analyzed, a good choice for the specific application would be the machine would be the machine shown in Figure 3.4 (d), the 130 mm outer stator diameter machine. This machine ensures 3 kW/kg power density, 95.8 % efficiency and 120.3 A rms phase current.

The main contributions of this analytical procedure are:

- The minimization of the total volume, so the weight, is obtained considering the thermal equilibrium for each machine with different stator outer diameter. Every machine design obtained through this method ensures the desired performance in terms of nominal operating point and thermal management.
- As a consequence of the previous point, the power density for every machine

design is maximized through this method.

- A good estimation of the efficiency of each machine is obtained analytically thanks to the inclusion of iron losses in the analysis.

3.4 References

[1] J. Benzaquen, J. He, and B. Mirafzal, «Toward more electric powertrains in aircraft: Technical challenges and advancements», *CES Transactions on Electrical Machines and Systems*, vol. 5, no. 3, pp. 177–193, 2021. DOI: 10.30941/CESTEMS.2021.00022.

[2] A. El-Refaie and M. Osama, «High specific power electrical machines: A system perspective», *CES Transactions on Electrical Machines and Systems*, vol. 3, no. 1, pp. 88–93, 2019. DOI: 10.30941/CESTEMS.2019.00012.

[3] B. Sarlioglu and C. T. Morris, «More electric aircraft: Review, challenges, and opportunities for commercial transport aircraft», *IEEE Transactions on Transportation Electrification*, vol. 1, no. 1, pp. 54–64, 2015. DOI: 10.1109/TTE.2015.2426499.

[4] V. Madonna, P. Giangrande, and M. Galea, «Electrical power generation in aircraft: Review, challenges, and opportunities», *IEEE Transactions on Transportation Electrification*, vol. 4, no. 3, pp. 646–659, 2018. DOI: 10.1109/TTE.2018.2834142.

[5] G. Devito, A. Theofanous, M. Galea, D. Barater, and S. Nuzzo, «Design optimization of a starter generator for more sustainable high power density aerospace applications», in *IECON 2024 - 50th Annual Conference of the IEEE Industrial Electronics Society*, 2024, pp. 1–6. DOI: 10.1109/IECON55916.2024.10905817.

[6] R. R. Moghaddam, S. Nategh, J. Islam, and A. Boglietti, «Different traction motor topologies used in e-mobility : Part ii: Magnet-based solutions», in *2020 International Conference on Electrical Machines (ICEM)*, vol. 1, 2020, pp. 138–143. DOI: 10.1109/ICEM49940.2020.9270938.

[7] C. J. Dalli, M. Galea, and J. Cilia, «Design considerations for an in-hub, direct drive traction motor for a formula sae race car», in *2024 International Conference on Electrical Machines (ICEM)*, 2024, pp. 1–6. DOI: 10.1109/ICEM60801.2024.10700291.

[8] E. Berg, «Turbine reduction gears versus electric propulsion for ships», *Journal of the American Institute of Electrical Engineers*, vol. 40, no. 9, pp. 724–729, 1921. DOI: 10.1109/JoAIEE.1921.6594006.

[9] J. Cilia, N. Azzopardi, M. Galea, and T. Sant, «Vessel considerations to support drive design for small harbour transport boats», in *2025 IEEE Workshop on Electrical Machines Design, Control and Diagnosis (WEMDCD)*, 2025, pp. 1–6. DOI: 10.1109/WEMDCD61816.2025.11014127.

[10] N. Arish, M. J. Kamper, and R. J. Wang, «Advancements in electrical marine propulsion technologies: A comprehensive overview», *SAIEE Africa Research Journal*, vol. 116, no. 1, pp. 14–29, 2025. DOI: 10.23919/SAIEE.2025.10755059.

[11] A. Del Pizzo, R. M. Polito, R. Rizzo, and P. Tricoli, «Design criteria of on-board propulsion for hybrid electric boats», in *The XIX International Conference on Electrical Machines - ICEM 2010*, 2010, pp. 1–6. DOI: 10.1109/ICELMACH.2010.5607817.

[12] R. Lakshmi Suresh Nimmana and A. Chiba, «Design of high power density motor for ev applications», in *2018 21st International Conference on Electrical Machines and Systems (ICEMS)*, 2018, pp. 104–108. DOI: 10.23919/ICEMS.2018.8549142.

[13] N. Soda and M. Enokizono, «Stator core shape design for low core loss and high power density of a small spm motor», in *2019 19th International Symposium on Electromagnetic Fields in Mechatronics, Electrical and Electronic Engineering (ISEF)*, 2019, pp. 1–2. DOI: 10.1109/ISEF45929.2019.9097017.

[14] S. B. Nicola Bianchi, *Metodologia di progettazione delle macchine elettriche*. cleup, 2001.

4. Additive Manufacturing Applied to Electrical Machines

Additive Manufacturing (AM), commonly known as 3D printing, has emerged as a manufacturing technology in the field of electrical machine design and production. By enabling layer-by-layer fabrication directly from digital models, AM allows the creation of complex geometries, customized components, and material distributions that are not achievable through conventional manufacturing methods. This opens new opportunities for improving the performance, efficiency, and compactness of electric motors.

In recent years, researchers have been exploring the potential of AM in producing key motor components such as stators, rotors, and cooling structures. Additive techniques enable optimized magnetic circuit topologies, improved thermal management, and the integration of multiple functionalities within a single part. Furthermore, the possibility of tailoring material properties (for example, through selective heat treatments or graded compositions) allows designers to better balance magnetic, mechanical, and thermal requirements.

However, despite its advantages, the application of additive manufacturing to electric motors still faces several challenges. Issues such as surface roughness, residual stresses, anisotropy of magnetic properties, and scalability of production need to be carefully addressed to ensure reliable and cost-effective implementation.

This chapter provides an overview of the current state and prospects of additive manufacturing for electric motor applications. It discusses the main AM processes suitable for magnetic materials, their influence on microstructure and magnetic performance, and how these aspects impact overall motor design and optimization.

4.1 General Overview

The expression AM includes a wide variety of techniques that create a component by layer deposition using different type of materials (e.g. plastics or metals). Focusing on EM manufacturing, the "Powder Bed Fusion" is the most employed method: it melts or sinters particles of metal powder (e.g. aluminium and titanium alloys, electric steels, soft magnetic composites, etc.) using a laser (e.g. SHS, SLM, SLS, DMLS) or electron beam (e.g. EBM) [1], [2].

The AM technologies mentioned before require an energy source which leads to a very high thermal gradient whose effects will be further explored in this Chapter.

From a theoretical standpoint, the efficiency of an electromechanical system is strictly bound by its magnetic flux distribution. Conventional manufacturing forces engineers to use simplified geometries (rectangles, circles, or laminations) that lead to flux leakage and suboptimal power density. AM allows for Topology Optimization (TO). By placing material only where the magnetic field lines require it, dead weight is minimized. This aligns with the fundamental principle of maximizing the magnetic loading while minimizing reluctance in the flux path.

From the point of view of iron losses, additive manufactured rotors or stators exhibit much higher losses than laminated ones because of the solid construction, which causes an increment of eddy currents induced in the part. All of these aspects are deepened in Chapter 4.

For this reasons some scientific papers are focused on methods to reduce the iron losses, in [3] a multi-material printing method is proposed to overcome iron losses drawback in AM rotors.

AM introduces inherent material anisotropy, which is particularly interesting for winding design in the case of high-frequency applications and for grain oriented magnetic synchronous reluctance rotors [4], [5].

As Naseer et al. point out. [6], by innovating materials and component fabrication technologies, it would be possible to make EMs with higher power density, increased efficiency, and reduced weight/volume. In addition, the greater freedom in the design and construction of complex geometries would allow the integration of heat dissipation into the structural components of the EM itself with consequent thermo-

mechanical benefit.

The construction of high-performance metal components by means of AM techniques has reached high levels of maturity in a relatively short time and with even good production volumes while still being relatively high in cost, which limits its application to high-tech industries [7], [8]. For example, GE Aviation [9] from 2015 to 2021 made by means of "Metal 3D-printing" 100'000 pieces of its fuel nozzle.

More recently, Porsche Industry [10] has produced entirely by SLM its electrical drive housing. It is a prototype, but compared with a weight reduction of 40% compared with the same component made by conventional mechanical technologies, the mechanical properties are almost the same. In addition, the production cycle promises to be leaner.

AM allows a freedom of design and construction previously unknown in EMs by paving the way toward entirely new geometries no longer constrained by previous planar-symmetry parameters.

In 2013 Aguilera et al.[11] constructed nonmetallic structural components within the active components such as magnets and windings can then be inserted.

The first "metal additive manufactured" rotors appear in 2016 as demonstrated by the attempt made by Selective Laser Melting (SLM) by Lammers et al. [12]. Due to the lack of specific materials, Lammers et al. chose H13, which was identified as the most suitable AM material and it is formed by adding alloying elements to carbon steel, to build their prototype to compare with a commercial target rotor in order to test its mechanical and electromagnetic properties in order to scientifically validate their method.

The poor magnetic properties were attributable to the martensitic microstructure with austenite parts of H13; however, by performing heat treatment in a furnace under "argon atmosphere" at 780°C for 20 minutes with subsequent slow cooling in the furnace, a significant improvement in the permeability of their prototype was possible. On the other hand, since the rotor was not structured with laminations the energy losses due to eddy currents became dominant as the frequency increased. Obvious were the mechanical advantages as they reduced the mass by 25% and the mass moment of inertia by 23%, which meant a restriction of the initial acceleration

transient by 23%.

Starting from 2018, there has been a strong acceleration of research in the field of AM applied to EMs as evidenced by the appearance of an increasing number of papers on the subject devoted to the design and implementation of new geometries for "active" and "passive" components and the development of hard or soft magnetic materials specific to the AM techniques. In [13], authors printed a full E-type transformer core, then they present a comparison between its properties and the ones of commercial FeSi alloys, with particular focus on iron losses generation. This aspect will be further analyzed in Section 4.4.

This push for scientific research can be attributed, according to Wrobel et al.[1], to the 18% growth that the AM market, to be understood as "hardware, materials, software, manufactured parts" related to the aerospace, biomedical, automotive etc. industries, has accomplished just in 2018, settling at $9.3 trillion and with even the future forecast to exceed $41 trillion in 2027.

AM offers the possibility to optimize the plunger geometry of reluctance tubular machines, as authors do in [14]. In Figure 4.1, the mock up prototype of machine's plunger pole is reported; thanks to additive manufacturing it was possible to explore more geometries with a different number of flux barriers, with the purpose of maximizing the performance of the machine.

Figure 4.1: Additively manufactured mock up prototype of the plunger pole of the synchronous tubular machine with five layers [14].

In addition, thanks to AM, it is possible to optimize the geometry of electrical machines windings, with the purpose of maximizing the slot filling factor and obtaining a better current distribution in the slots, leading to a maximization of the perfor-

mance of the machine, as shown in [15], [16] and [17]. Another important application of Am in electrical machines regards the cooling system, which can be optimized to reach the desired power dissipation, as shown in [18] and [19].

Taking a cursory look at the items selected and studied, it can be said that about half of them involve "Laser Powder Bed Fusion" (L-PBF), used in [20]. This is explained by virtue of the high manufacturing densities it provides. About one-fourth of the articles concern different extrusion methods that are well suited for the production of low-density parts and also of permanent magnets, by virtue of the advantages that the non-homogeneous structure can guarantee in PMs. Other AM techniques for metallic materials pioneered in the field of EMs are "Electron Beam Melting" (EBM, "Direct Energy Deposition" and "Bitter Jetting" (BJ).

AM application in the EM field has reached different grades of maturity. Large-scale production using AM is possible for the non-active assemblies for mechanical and thermal management. On the other hand, active parts such as windings, magnetic cores and permanent-magnets have a lower maturity. With AM, however, it is possible to design structures for these components that are impossible to realize through conventional manufacturing techniques [21].

The power density of a high-performance EM is not limited by its electromagnetics, but by its thermal limits. Heat dissipation is proportional to the surface area in contact with the coolant and AM enables the integration of internal cooling channels and lattice structures that exponentially increase the surface-to-volume ratio. This allows the system to operate at higher current densities (J) without exceeding the insulation's thermal class, effectively shifting the theoretical "thermal ceiling" of the machine.

4.2 AM Technologies

In general, the term "Additive Manufacturing" refers to those technologies of building layer upon layer from a 3D model in .STL format through seamless digital Computer Aided Design (CAD) and Computer Aided Manufacturing (CAM) integration; by varying the material used, the energy source and other macroparameters, different AM techniques can be specified. For the American Society for Testing and Standards (ASTM) [22] there are 7 types of AM:

1. Vat Photopolymerisation (VPP): the liquid photopolymer in a vat is selectively cured by light-activated polymerization;
2. Material Jetting (MJT): the droplets of build material are selectively deposed;
3. Binder Jetting (BJT): the liquid bonding agent is selectively deposited to join powder materials;
4. Material Extrusion (MEX): the material is selectively dispensed through a nozzle or orifice;
5. Powder Bed Fusion (PBF): the thermal energy selectively fuses regions of a powder bed;
6. Sheet Lamination (SL): the sheets of material are bonded to form an object;
7. Direct Energy Deposition (DED): the focused thermal energy is used to fuse materials by melting as they are being deposited.

Variable subclasses can also be identified for each of the previous 7 main classes based on the materials with which they operate.

4.2.1 AM for Polymers

As can be seen in Figure 4.2, taken from [23], PBF applied to polymeric materials includes "Multi Jet Fusion" (MJF) and "Selective Laser Sintering" (SLS).

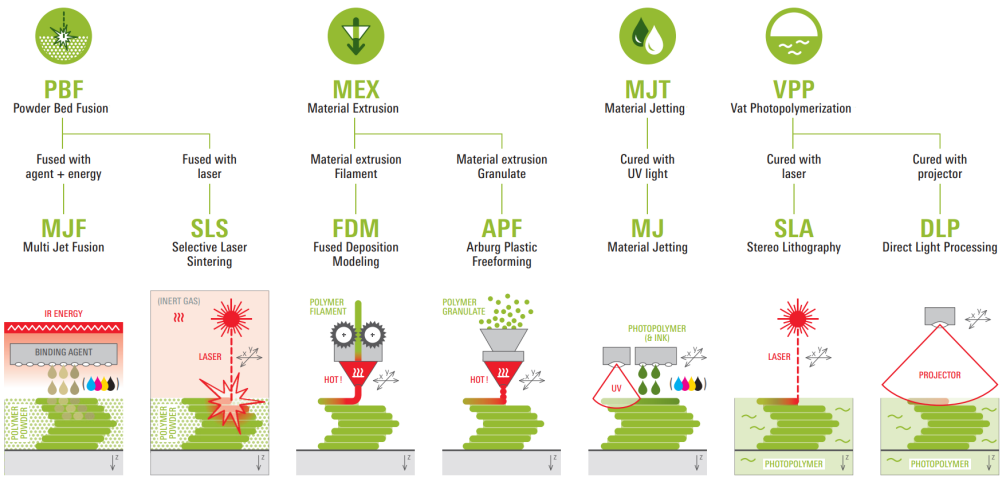

Figure 4.2: Schematic representation of AM technologies for polymers [23] (Graphics were created by Prof. Dr.-Ing. Steffen Ritter from Reutlingen University, Germany in cooperation with Formnext/Mesago Messe Frankfurt GmbH, Germany ©).

In MJF, the process begins from layer of polymer powder. Then, liquid droplets are applied to the powder layer and, thanks to a infrared source, the material is melt. The SLS exploits a movable laser beam which sinters the polymer powder locally layer by layer. The component is generated by solidifying its cross section in each layer.

MEX applied to polymers include the "Fused Deposition Modeling" (FDM), used in [24], and the "Arburg Plastic Freeforming" (APF). The FDM uses a hot nozzle unit to plasticize a polymer filament. The APF instead of a wire-shaped plastic uses a plastic granulate.

The "Material Jetting" for polymers (MJ) applies locally and layer by layer small droplets of photopolymer through many nozzles and, instantly, cures the viscous photopolymer by mean UV-light.

The "Stero Lithography" (SLA) and the "Direct Light Processing" (DLP) are two examples of VPP applied to polymers. The SLA cures selectively the viscous photopolymer in layers by means of a movable laser beam. The DLP polymerizes the exposed photopolimer layer by layer using a projector.

In [25] an interesting application, which uses 3D printed polymers, is presented for lightweight silicon photovoltaics technology.

4.2.2 AM for Metals

In Figure 4.3 there is a schematic recap of the AM technologies that could be applied to metals. About PBF, it's possible to recognise the "Selective Laser Melting" (SLM) and the "Electron Beam Melting". The SLM melts locally layer by layer the selected metal powder by means of a movable laser beam, thus solidifying a cross-section of the component. Compared to sintering there is a higher density of the component and a different microstructure due to the different process of consolidation which leads to greater mechanical characteristics for the same material used. The main challenges of this technology are deeply analyzed in [26]. The EBM works in the same way, but instead of a laser, it uses an electron beam to melt locally layer by layer the selected metal powder; for this reason the EMB can be used with only few metals (e.g. titanium, tungsten, Co-Cr, Inconel 718, etc.).

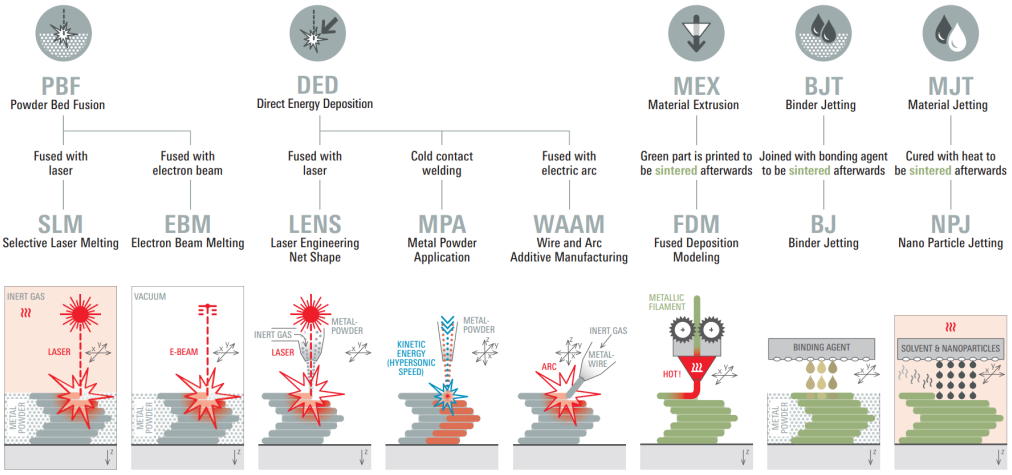

Figure 4.3: Schematic representation of AM technologies for metals [23] (Graphics were created by Prof. Dr.-Ing. Steffen Ritter from Reutlingen University, Germany in cooperation with Formnext/Mesago Messe Frankfurt GmbH, Germany ©).

The "Laser Engineering Net Shape" (LENS) [27], the "Metal Powder Application" (MPA) and the "Wire and Arc Additive Manufacturing" (WAAM) are DED technologies. The LENS applies and melts the metal material simultaneously by a laser beam. The solidification of the melt generates new layers.

The MPA, also called "Cold Spray", applies the metalic powder with very high kinetic energy layer by layer; in this way, the component is close to the final shape and it's also possible to combine more materials.

The WAAM applies locally and layer by layer the melted metal wire by means of the arc welding; in this way, it's possible to quickly produce near-net-shape metal components.

The MEX for metals is called "Fused Deposition Modeling" (FDM) and plasticizes a metalic filament by means of a hot mozzle unit and doses selectively the material layer by layer.

The "Binder Jetting" for metals (BJ) applies selectively tiny binder droplets onto metal powder by means of many nozzles to stick it layer by layer.

In the end, the MJT applied to metals is called "Nano Particle Jetting" (NPJ). The NPJ doses selectively and locally a solvent fluid cointaining nano-metal particles; when the solvent evaporates the nano-particles bond togheter. The components made by FDM, BJ and NPJ must be sintered afterwards.

4.2.3 AM for Other Materials

Watching the Figure 4.4, the tecnologies for other materials are pretty similar to those we have already discussed in the previous "subsection".

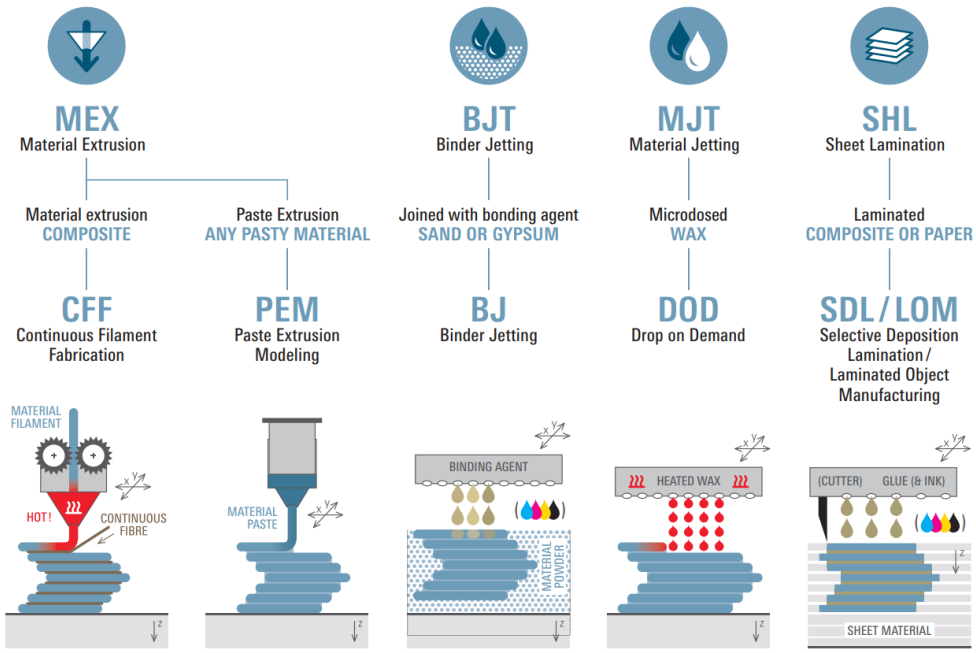

Figure 4.4: Schematic representation of AM technologies for other materials [23] (Graphics were created by Prof. Dr.-Ing. Steffen Ritter from Reutlingen University, Germany in cooperation with Formnext/Mesago Messe Frankfurt GmbH, Germany ©).

It's possible to add that the MEX of composite material is called "Continuous Filament Fabrication" (CFF) and uses a hot nozzle unit to plasticize selectively a wire-shaped plastic that is dosed layer by layer around continuously deposited reinforcing fibers. Another MEX technologies is the "Paste Extrusion Modeling" (PEM) which doses selectively layer by layer any pasty material by means of a piston-nozzle.

The BLT joins with a bonding agent sand or gypsum.

The MJT is called "Drop on Demand" because it microdoses selectively, through many nozzle, heated wax droplets layer by layer.

The SHL laminates composite or paper and is called "Selective Deposition Lamination" (SDL) or "Laminated Object Manufacturing" (LOM). Nozzles are devices that are designed to control the direction or characteristics of a fluid flow, usually to increase its velocity. In this application, they are used to guarantee a good level of

precision to apply locally adhesive to the respective material layer. Each level can be stacked and laminated directly or subsequently and, then, the finished component can be cut out along the contour. Nozzles are devices that are designed to control the direction or characteristics of a fluid flow, usually to increase its velocity. In this application, they are used to guarantee a good level of precision to apply locally adhesive to the respective material layer. Each level can be stacked and laminated directly or subsequently and, then, the finished component can be cut out along the contour.

4.2.4 AM for EMs

Focusing on EM manufacturing, the “Powder Bed Fusion” is the most employed method: it melts or sinters particles of metal powder (e.g. aluminium and titanium alloys, electric steels, soft magnetic composites, etc.) using a laser or electron beam. It is possible to classify the following PBF techniques:

- Direct Metal Laser Sintering (DMLS)
- Electron Beam Melting (EBM)
- Selective Heat Sintering (SHS)
- Selective Laser Melting (SLM)
- Selective Laser Sintering (SLS)

After the previous general review about the AM technologies for metal aditive manufacturing, a particular focus should be dedicated on the main ones among them that are used for fabricating permanent magnets, like cold spray.

Cold Spray, also called "Metal Powder Application", is recently applied to the fabrication of PMs. In a CS process, the fine magnetic particles, in a compressed gas stream, are hurled at high-velocity, in general higher than 300 m/s, throw a substrate or backing plate; they deform plastically so they can mechanically interlocking and metallurgically bond creating a layer.

The metalic powder remains solid state during the entire deposition process and, in this way, the thermal defects, e.g. oxidation and thermal stresses, are not seen in the PMs so made. Moreover, CS lets to spray on metalic surface as the rotor core. In this way, it possible to obtain complex near-net-shape geometry.

4.3 Origin of Mechanical Defects

There are different kind of defects that can be originated from distinct factors. Some of them can be related to the powder, such as trapped gas or surface contamination and oxidation. Besides, others can be related to the process, like the lack of fusion porosity, formation of columnar grains or surface finish and roughness [28].

It is also important to take into account the possibilities of defects generation after a post processing treatment, as it can be annealing, which can cause thermally induced porosity. Limiting the arise of these kind of defects is fundamental to obtain a part with the desired mechanical properties.

One important parameter to set in an additive manufacturing process is laser energy input, which can affect significantly the mechanical properties of the material. In fact, increasing the energy input brings to an improvement in powder melting and a reduction in melt-pool instabilities, so the part becomes more dense. Anyway, as said before, the increment of energy input leads to spherical pores and cracks generation, which cause difficulties for the part to reach full densification.

When the energy input is high the melt-pool shape changes from flat to protuberant, the conduction mode welding is replaced by key-hole welding. The surface vaporization of material brings to the formation of a key-hole. In this process, the gas bubbles generated can remain trapped inside the melt-pool during the solidification process.

Thermal stresses are the main cause which brings to the formation of cracks during SLM process. In fact, since SLM process bases its working principle in the concentrated application of high energy in a short time in the same point, tensile residual stresses could be introduced in the part.

Considering this and the low heat conductivity of the powder bed, an high thermal gradient is generated near to the laser spot. In these conditions, differential thermal expansion are generated, so the heat affected zone, that presents a reduction of the tendency to expand due to the surrounding material is inhibited by the surrounding material, could be plastically compressed. During cooling, tensile stresses are generated because of the upper layer's tendency to contract.

4.3.1 Effects of Annealing on FeSi6.9

Annealing is the process of heating a metal or alloy to a temperature below its melting point in order to improve its mechanical characteristics. In [29] authors investigate the effects of annealing on the properties of FeSi6.9 produced by SLM. Some sets of different samples were manufactured with different shapes: cubic, wall and ring. Then they were annealed in argon atmosphere for 1 h at four different temperatures (400 °C, 700 °C, 900 °C and 1150 °C) before furnace cooling. Authors noticed that, thanks to the annealing at 900°C, the melt-pool boundary lines disappear, probably because of the dissolution of silicon in the solid. At 1150°C, the sample has an homogenized microstructure, which presents a non-uniform grain size, so the recrystallization process has not finished yet.

The technique used to do these analysis is electron backscatter diffraction (EBSD), which is a scanning electron microscopy (SEM) technique for material characterization, in which the electron beam is scanned across the surface of a tilted crystalline sample; the diffracted electrons at each point form a pattern that can be detected and, then, analyzed with appropriate hardware and software.

The results obtained shows that annealing does not modify the $< 001 >$ texture induced by SLM in the building direction (BD), so it can be used to improve material's mechanical and magnetic properties without weakening the beneficial crystallographic texture induced by SLM. The properties obtained from the tests done on the as-built and annealed ring samples are resumed in the following points with a comparison with a commercial grade of electrical steel high-Si. These results shows that:

- The permeability grows with the increase of the annealing temperature, reaching the value of the commercial sample. This happens thanks to the fact that stress relief and grain growth reduce the amount of lattice defects, that cause permeability reduction since they act as pinning sites for the magnetic domain walls.
- Induction B_{10}, which is the flux density at an applied field strength $H = 1000 A/m$, increases with annealing temperature; otherwise, B_{50} is little affected by annealing, which means that the considered applied field is strong

enough to overcome most of the manufacturing-induced obstacles to magnetization.

- Hysteresis loss, expressed in terms of H_c, decreases with the increase of the annealing temperature.
- The remanence B_r has a non monotonic dependence with the annealing temperature. Its initial increase is due to the effect of the residual stress relief, but, then, thanks to grain enlargement, the defect density decreases, hindering demagnetization and leading to a reduction in Br at high annealing temperature.
- The total power loss decreases with increasing annealing temperature, with a trend similar to the one of H_c. This suggests that the eddy current loss component does not increase significantly with grain growth.

Materials produced by Selective Laser Melting (SLM) generally exhibit a very fine microstructure, owing to the rapid solidification rates that characterize the process. This results in a small grain size, which negatively affects the magnetic properties of the printed material. Indeed, the high density of grain boundaries hinders domain wall motion, leading to increased hysteresis losses and lower magnetic permeability. Consequently, as-printed SLM materials are often not suitable for practical electromagnetic applications without further post-processing. In this context, annealing treatment becomes essential, as it promotes grain enlargement and relieves the residual stresses generated during fabrication. These microstructural modifications improve the magnetic response of the material, making annealing a fundamental step for the effective use of SLM components in electrical machine applications.

4.3.2 Effects of Annealing on FeCo49V2

For FeCo49V2 produced by SLM, the heat treatment consists of pre-annealing at *700°C* for *2 hours*, followed by annealing at *820°C* for *10 hours*, as described in [30] and [31]. The two-stage approach optimizes the microstructure for improved magnetic performance, as reported in Section **??**, and allows to achieve more uniform and larger grain size which is known to be beneficial for reducing hysteresis losses and increasing permeability.

The as-built and heat-treated samples, illustrated in Figure 4.5, underwent tensile

testing to assess their mechanical properties and evaluate the material's printability under various conditions, such as variations in thickness, the presence of air gaps, and different laser building directions.

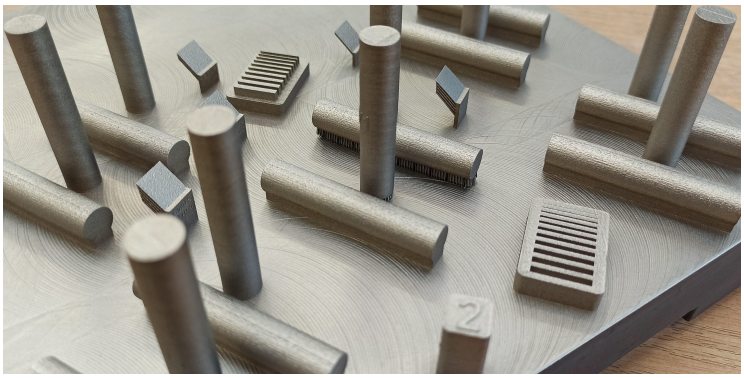

Figure 4.5: FeCo49V2 samples used for tensile testing to evaluate the mechanical proprieties of the additively manufactured material.

Table 4.1 summarizes the key findings of the tensile tests. The heat treatment significantly altered the mechanical properties of the FeCo49V2 alloy.

Table 4.1: Mechanical of as-built and heat-treated Fe-Co-V samples.

	Tensile strength R_m [N/mm²]	**Yield strength** $R_{p0.2}$ [N/mm²]	**Elongation at break** A_5 [%]
As built	900 - 1000	800 - 900	5 - 20
Heat-treated	250 - 280	290 - 330	2 - 15

The as-built samples exhibited high tensile strength (R_m) ranging from 900 to 1000 N/mm^2 and yield strength ($R_{p0.2}$) between 800 and 900 N/mm^2.

After heat treatment, both tensile and yield strength decreased, with tensile strength falling to 250-280 N/mm^2 and yield strength to 290-330 N/mm^2.

The observed reduction in strength is likely attributed to the relaxation of internal stresses during the heat treatment process and to the reduction of grain boundary strengthening associated with larger grain size.

Ductility, represented by the elongation at break (A_5), also exhibits notable changes. The as-built samples show elongation values between 5% and 20%, indicating moderate ductility, with variation possibly linked to microstructural heterogeneity. How-

ever, the heat-treated samples display a reduced elongation range of 2% to 15%, signifying a substantial loss in ductility that can be attributed to embrittlement mechanisms, grain boundary weakening, and/or the precipitation of brittle phases during heat treatment.

The observed results highlight the need for a careful balance between desired properties based on the intended application.

Table 4.2 summarizes the key magnetic properties extracted from the DC characterization of the FeCo49V2 samples. These properties are comparable to those of Fe-Co alloys [32], and also, in particular, to the Fe-Co-1.5V alloy produced by Laser Engineered Net Shaping (LENS) [33].

The data presented include the maximum applied magnetic field strength ($H_{\max}$), the corresponding magnetic flux density (B), the magnetic field strength at which maximum relative permeability occurs ($H_{\mu_{\max}}$), and the maximum relative permeability ($\mu_{\mathrm{rel,max}}$). These parameters are provided for each printing orientation 0°; 45°, and for the as-built (NO-h) and heat treatment (HT) conditions.

Table 4.2: Summary of DC magnetic properties

Sample	$H_{\mathbf{max}}$ **[A/m]**	B **[T]**	$H_{\mu_{\mathbf{max}}}$ **[A/m]**	$\mu_{\mathbf{rel,max}}$
0° NO-h	15005.55	1.883	2093.14	293.62
0° HT	14974.88	2.192	838.56	1415.50
45° NO-h	14998.01	1.805	1088.48	448.03
45° HT	14992.79	2.284	833.78	1475.76

The table indicates that heat treatment significantly enhances the magnetic properties, particularly the maximum relative permeability. For instance, the heat-treated sample exhibits a $\mu_{\mathrm{rel,max}}$ exceeding 1400, roughly four times greater than that of the non-heat-treated (as built) counterparts. It is noteworthy that between the heat-treated samples, the 45° build orientation yields the highest saturation magnetization. However, the building direction does not strongly affect the magnetic properties of the FeCo49V2 alloy.

Figure 4.6 compares the BH curves of the various samples.

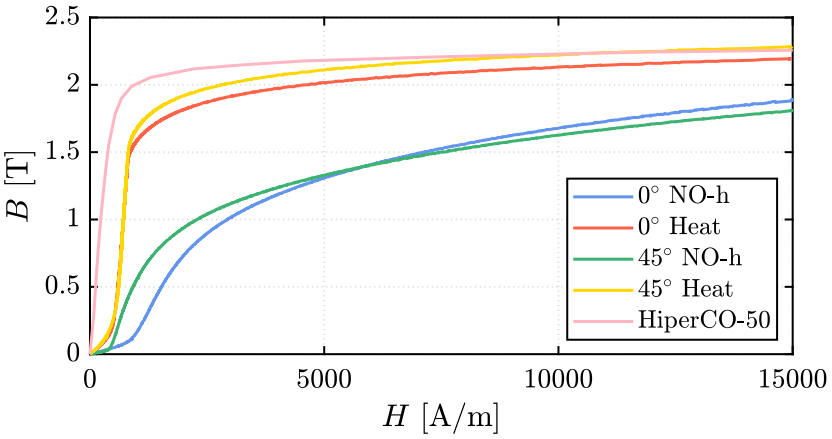

Figure 4.6: BH curves for the FeCo49V2 samples fabricated at 0° and 45° build orientations, with and without heat treatment, and for traditional Hiperco-50 alloy.

The as-built samples, 0° NO-h (blue curve) and 45° NO-h (green curve), exhibit a lower initial slope, indicating a lower initial permeability. In contrast, the heat-treated samples, 0° HT (red curve) and 45° HT (yellow curve), show a steeper initial slope, suggesting a substantial increase in initial permeability.

The heat-treated samples also demonstrate higher saturation magnetization, particularly the 45° HT sample, which reaches the highest saturation point. The curves for the heat-treated samples are nearly superimposed for the lowest field range, until 1000 A/m, and have the same qualitative trend at the highest applied fields, with a little difference in favor of the 45° HT sample compared to the 0° HT.

The heat treatment markedly improves the magnetic properties compared to the as-built samples, confirming its effectiveness in enhancing the performance of additively manufactured FeCo49V2. Differences between build orientations are less significant, especially in the initial magnetization region, suggesting a minor influence of build direction on the magnetic properties for these orientations.

Focusing on the results of Figure 4.7, the as-built (NO-h) samples (blue and green curves) exhibit low and relatively constant permeability as the magnetic field strength increases. In contrast, the heat-treated (HT) samples (red and yellow curves) demonstrate significantly higher permeability, especially at lower H values, indicating a superior ability to concentrate magnetic flux.

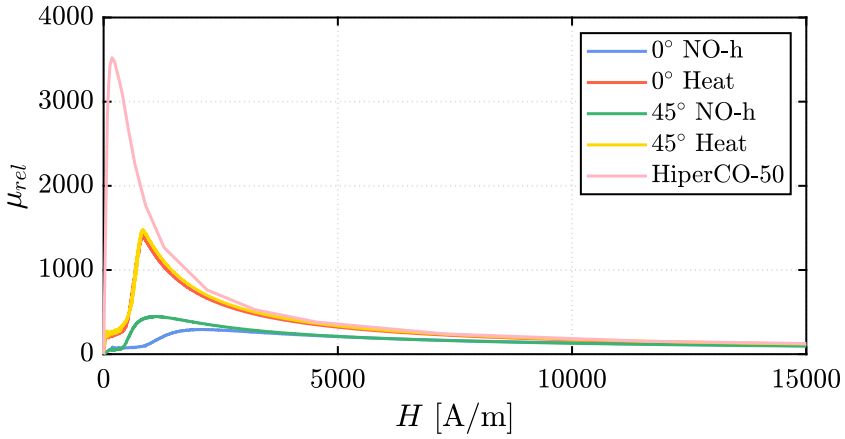

Figure 4.7: Relative permeability (μ_{rel}) versus magnetic field strength (H) for the FeCo49V2 samples fabricated at 0° and 45° build orientations, with and without heat treatment, and for traditional Hiperco-50 alloy.

This aligns with the microstructural changes induced by heat treatment, which likely promotes larger grain size and reduces defect density, thus hindering domain wall motion less.

The permeability peak observed in the heat-treated samples highlights the existence of an optimal operating range in which the magnetic responsiveness of the material is maximized. This suggests that the heat treatment effectively modifies the microstructure, enhancing domain wall mobility and thus improving the magnetic response under specific excitation conditions. Such behavior is particularly relevant for electrical machine applications, as it identifies the conditions under which the material can provide the highest magnetic performance.

Moreover, the limited influence of printing direction on permeability, especially after heat treatment, indicates that the optimized thermal treatment promotes a nearly isotropic magnetic behavior. Although additive manufacturing processes typically introduce directional anisotropies due to their layer-wise nature, the annealing treatment appears to reduce these effects by homogenizing the microstructure and relieving residual stresses. Consequently, the heat-treated material exhibits a more uniform magnetic response, which is a highly beneficial feature for practical electromagnetic applications.

Hiperco-50 alloy is considered as a reference traditional soft magnetic material. The chemical composition is the same of the powder used for the printed samples: it is

an iron-cobalt soft magnetic alloy comprised of 49 % cobalt, 2 % vanadium, balance iron. It still exhibits better magnetic performance, even compared with the annealed samples.

Figure 4.8 compares the DC hysteresis loops and the results are summarized in Table 4.3.

Table 4.3: Summary of DC hysteresis test for the FeCo49V2 samples fabricated at 0° and 45° build orientations, with and without heat treatment.

Sample	H_{max} **[A/m]**	B_{max} **[T]**	μ_r	J_r **[T]**	H_c **[A/m]**
0° NO-h	15024,86	1,885	99,85	0,892	1420,65
0° HEAT	15021,71	2,197	116,40	1,602	730,30
45° NO-h	15002,63	1,799	95,43	0,987	868,07
45° HEAT	14950,85	2,29	121,72	1,672	748,39

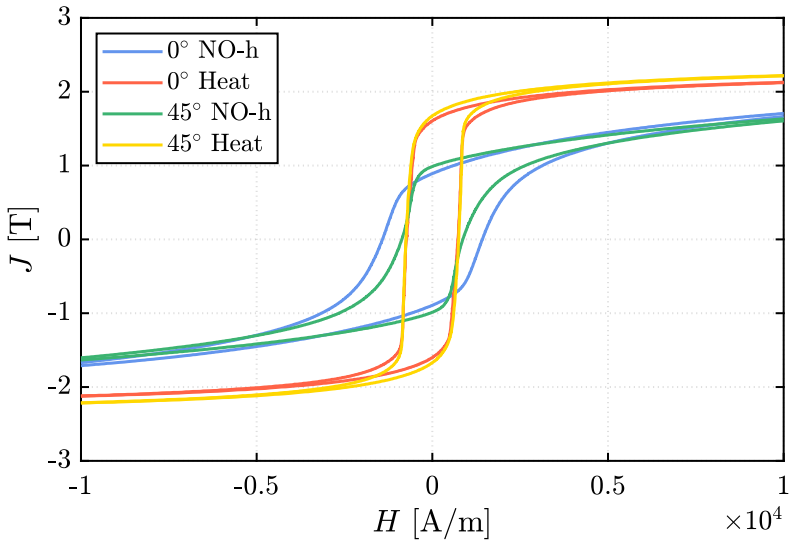

Figure 4.8: DC hysteresis loops for the FeCo49V2 samples fabricated at 0° and 45° build orientations, with and without heat treatment.

The NO-h samples show wider loops, indicating higher coercivity and hysteresis losses, likely due to a higher density of pinning sites, such as grain boundaries and defects, which impede domain wall movement. The HT samples exhibit narrower loops, meaning lower coercivity and reduced energy losses. This improvement can be attributed to the larger grain size and reduced defect density achieved through heat treatment, facilitating easier domain wall motion.

The narrower loops imply lower energy dissipation during magnetization reversal, making the HT samples more energy-efficient. The minimal effect of printing direction on the hysteresis loops, especially for the HT samples, further supports the largely isotropic magnetic response after heat treatment.

Table 4.4 summarizes the magnetic properties of the samples at 20 Hz and 50 Hz, highlighting the impact of heat treatment (HT) and build orientation (0° vs. 45°). The HT samples consistently demonstrate superior magnetic performance, exhibiting significantly higher relative permeability (μ_{rel}) and remanence (Jr) compared to the as-built (NO-h) samples. The specific losses (Ps) are higher for the heat-treated samples, reasonably ascribable to the higher values of the maximum flux density B_{max}. The influence of build orientation is minimal, particularly after heat treatment, supporting the conclusion that the optimized heat treatment effectively mitigates any significant anisotropy introduced during the L-PBF process.

Table 4.4: Magnetic Properties at 20 Hz and 50 Hz

Frequency [Hz]	**Sample**	$H_{\mathbf{max}}$ **[A/m]**	$B_{\mathbf{max}}$ **[T]**	$\mu_{\mathbf{rel}}$	$J_{\mathbf{r}}$ **[T]**	$H_{\mathbf{c}}$ **[A/m]**	$P_{\mathbf{spec}}$ **[W/kg]**
20	0° NO-h	6105.37	1.409	183.71	0.957	2536.13	28.19
	0° HEAT	4395.70	2.000	362.07	1.694	2443.05	46.85
	45° NO-h	5880.63	1.406	190.34	1.064	1988.48	26.87
	45° HEAT	3981.94	2.005	401.10	1.759	2328.53	44.18
50	0° NO-h	5823.85	1.205	165.02	0.952	3608.68	90.32
	0° HEAT	6180.02	1.703	219.93	1.571	3864.93	156.69
	45° NO-h	6170.77	1.303	168.22	1.076	3283.16	100.74
	45° HEAT	5545.67	1.699	244.48	1.573	3550.13	138.77

Figures 4.9 and 4.10 illustrate the AC hysteresis loops of the samples at *20Hz* and *50Hz* respectively. These measurements evaluate the dynamic magnetic properties of the additively manufactured material and assess the impact of heat treatment and build orientation on core losses under AC excitation.

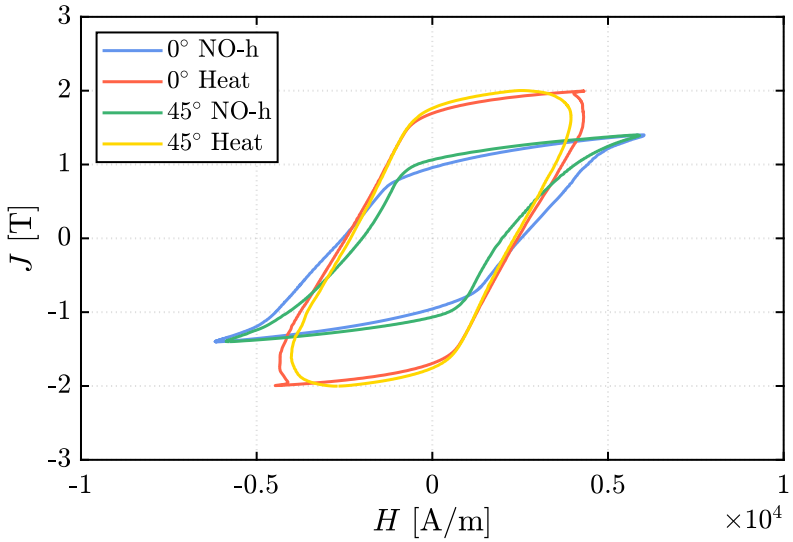

Figure 4.9: AC hysteresis loops measured at *20Hz* for the FeCo49V2 samples, comparing the effects of build orientation (0° and 45°) and heat treatment (HT and NO-h).

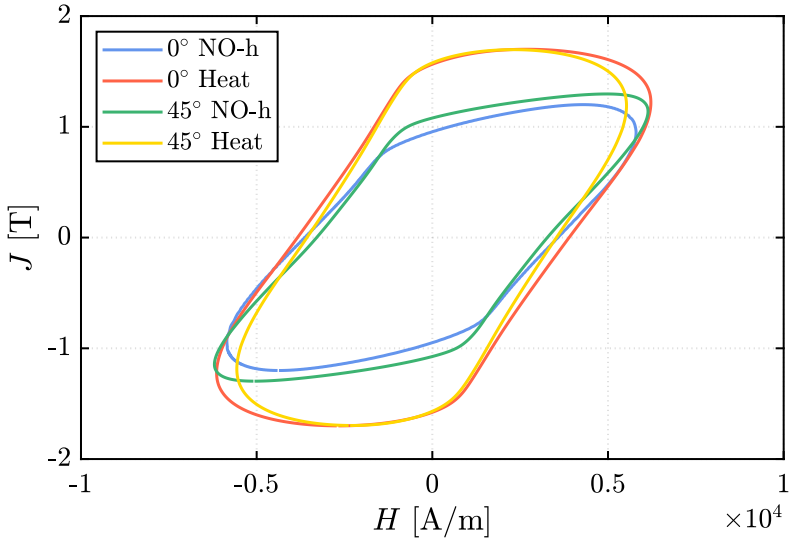

Figure 4.10: AC hysteresis loops measured at *50Hz* for the FeCo49V2 samples, comparing the effects of build orientation (0° and 45°) and heat treatment (HT and NO-h).

At 20 Hz (Figure 4.9), the NO-h samples (blue and green curves) exhibit significantly wider hysteresis loops than the HT samples (red and yellow curves). This indicates higher hysteresis losses in the NO-h samples, consistent with the DC hysteresis measurements. The larger loop areas suggest a greater density of pinning sites, hindering domain wall motion. The HT samples show narrower loops, implying

reduced hysteresis losses. At this frequency, the effect of build orientation is minimal, with both NO-h and HT curves for 0° and 45° orientations closely aligned.

At 50 Hz (Figure 4.10), the loop areas for all samples expand, indicating increased core losses due to the growing contribution of both hysteresis and eddy current losses. The HT samples maintain smaller loop areas than the NO-h samples, confirming the continued benefits of heat treatment. Interestingly, while build orientation had a minimal effect at 20 Hz, at 50 Hz the curves of the HT samples are almost superimposed, whereas a slight difference emerges between the NO-h samples. The green curve (45° NO-h) is slightly wider than the blue curve (0° NO-h), suggesting a minor degree of anisotropy in the as-built material that becomes more apparent at higher frequencies, possibly related to microstructural variations from the L-PBF process.

The same measurements were performed at higher excitation frequencies. As an example, the test at 500 Hz is reported, with the resulting hysteresis loop shown in Figure 4.11. As expected, the loop areas increase for both the HT and the NO-h samples.

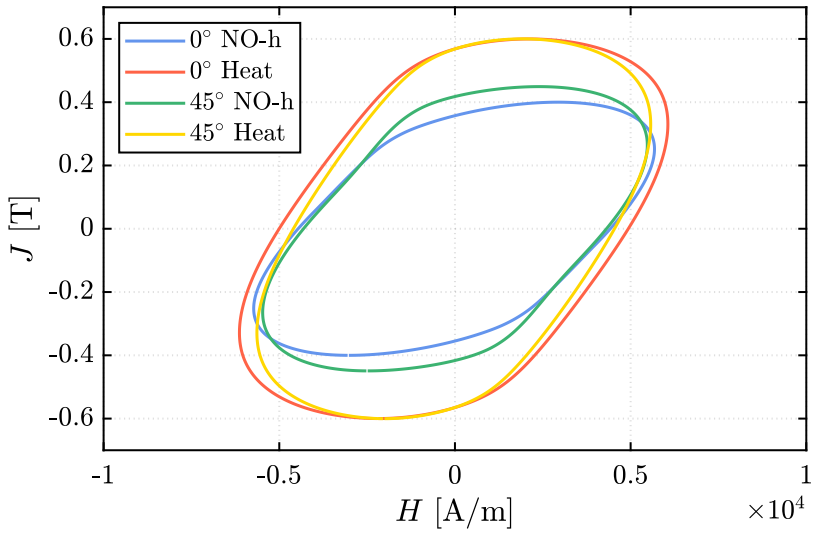

Figure 4.11: AC hysteresis loops measured at *500Hz* for the FeCo49V2 samples, comparing the effects of build orientation (0° and 45°) and heat treatment (HT and NO-h).

Collectively, these AC hysteresis measurements highlight the effectiveness of heat treatment in improving the dynamic magnetic performance of additively manufac-

tured FeCo49V2, especially at relatively low frequencies.

4.3.3 Relationship between laser energy input, microstructures and magnetic properties of soft ferromagnetic materials

Laser energy input is an important parameter which must be defined in a proper way to obtain the desired performance from the material. With the purpose of defining the better way to produce a part, it is a good starting point to analyze the correlation between construction parameters and magnetic end mechanical properties of the generated material.

Authors in [34] defined the main SLM parameters as recommended by the Realizer SLM-50 manufacturer, which is an industrial desktop 3D printer made by ReaLizer, for processing stainless steel powders (Figure 4.12); in this way, the thermal and optical properties of the material obtained are expected to be the closest to those of silicon steel. Varying the scan speed (v), the effect of energy input $E = \frac{P}{v}$ on the material properties can be studied. The energy input is a very important parameter, which can affect a lot the crystallographic structure of a component generated using AM, modifying its mechanical and magnetic properties.

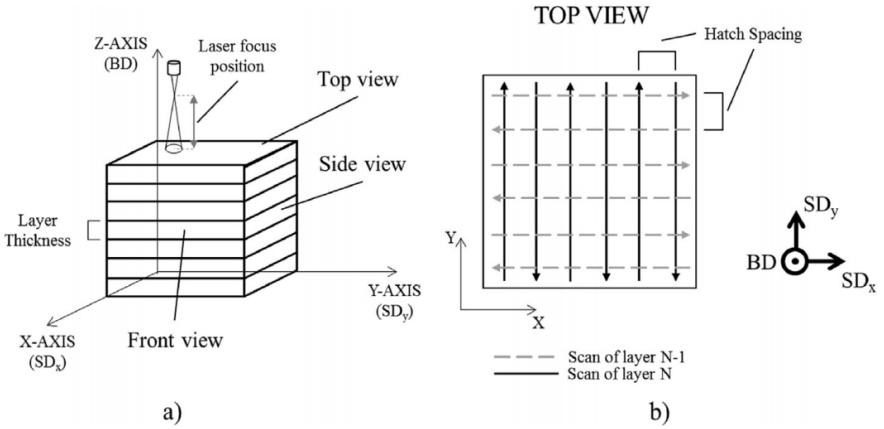

Figure 4.12: Overview of the SLM processing parameters and laser scan strategy. The build (BD) and scan directions (SDx and SDy) are indicated with respect to the sample coordinates. In (a) the different views of the cubic sample are indicated and the definitions of layer thickness and layer focus position are represented. Top view of the sample with the bidirectional scan vectors is provided in (b) by Garibaldi et al. [34]

In Figure 4.13 (a) the porosity and pore morphology obtained in the samples are reported, showing effects of the laser energy input. According to the results reported, the samples obtained with laser energy input $E < 280\frac{J}{m}$ are characterized by large pores with an irregular shape. Increasing the energy input, the pores present a more regular shape, but crack generation is induced;in fact, considering $E \geq 420\frac{J}{m}$ little spherical pores come out and crack formation is promoted.

As shown in Figure 4.13 the samples which ensure the best compromise between part densification and crack formation are S_{140} and S_{280}. Considering samples S_{140} and S_{280}, in Figure 4.14 the results of PFs are reported, which quantify the texture intensities for the three crystallographic direction families $< 001 >$, $< 101 >$ and $< 111 >$. Both samples have a $< 001 >$ texture along the building direction (BD). Increasing the energy input to 280 J/m, the fiber texture in sample S_{140} becomes a cube texture.

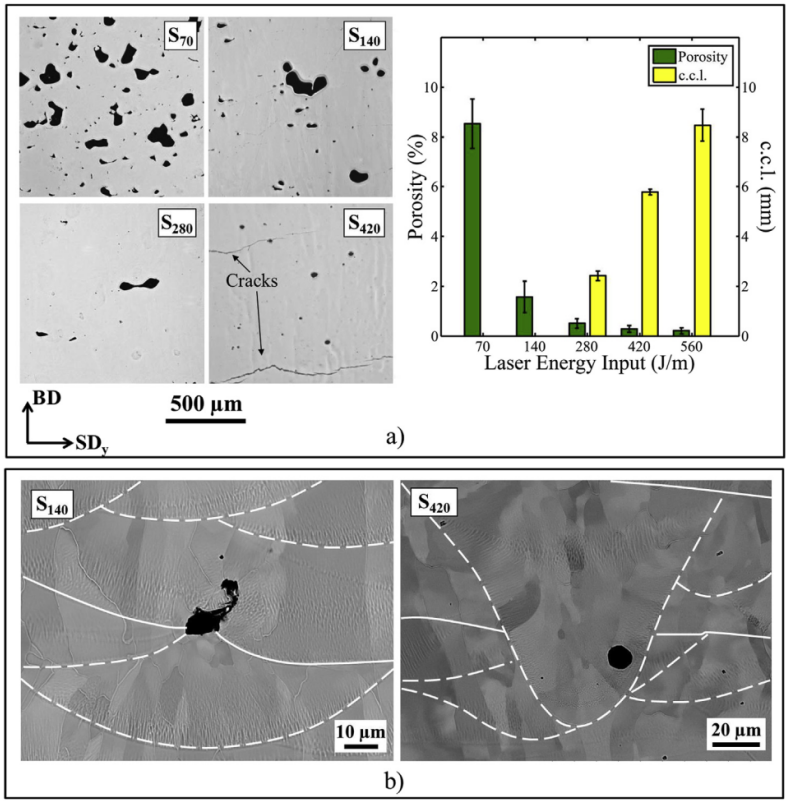

Figure 4.13: Effect of processing laser energy input on sample porosity. In (a) the optical micrographs of different SLM samples are shown (left), alongside the values of percent porosity and c.c.l. plotted against laser energy input (right). The SEM micrographs in (b) show two examples of irregular (left) and spherical pores (right). The dashed and solid lines indicate the transversal and longitudinal melt-pool cross-sections, respectively by Garibaldi et al. [34]

So, the laser energy input largely affects the intensity of the texture, intensifying the crystallographic texture along the BD; this is due to the amount of partial remelting, which has increased, and the improved smoothness of the deposited layers, which occurs when the energy input of the scanning laser is increased. Having a great quantity of optimally oriented grains will lead to stronger texture intensities.

Furthermore, augmenting the energy input from 140 J/m to 280 J/m modifies the $< 001 >$ fibre-texture into a cubic texture, as shown in Figure 4.14.

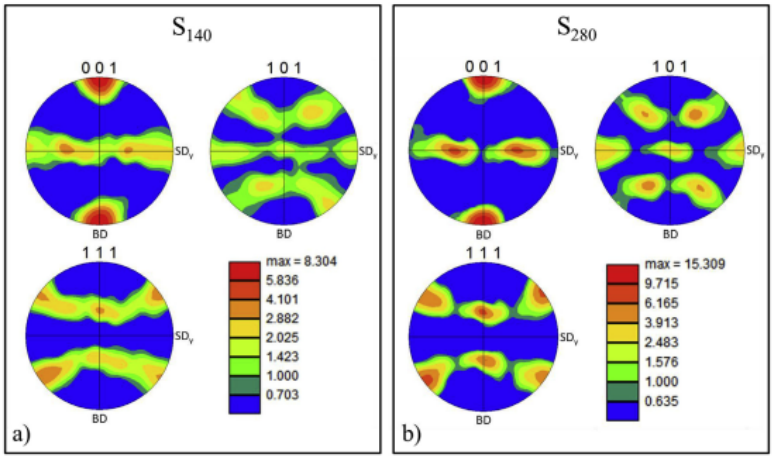

Figure 4.14: Pole figures (PF) showing the preferred orientation of the $< 001 >$ crystallographic direction for samples S_{280} and S_{140} and for three samples views (front, side and top) by Garibaldi et al. [34]

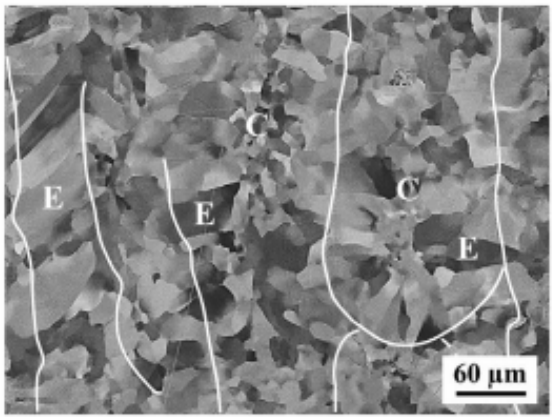

Figure 4.15: SEM micrographs for the top view of sample S_{280} the letter E and C indicate regions of elongated and equiaxed grains, respectively by Garibaldi et al. [34]

As a consequence, deeper melt-pools are generated, leading to a shift of about 90° in the growth direction of the cellulardendritic solidification structure. In the

scanning plane, some grains have been produced with an elongated cross-section and oriented following the solidification front normal. The morphological orientation has also prompted a crystallographic texture and the EBSD results have shown that in the scanning plane the $< 001 >$ crystallographic axes follow the morphological orientation of the grains.

The most common soft magnetic material used for the manufacture of electrical machines is FeSi electrical steel [4]. In these alloys, there can be a different percentage of silicon, depending on the purpose of the specific application. Silicon is a substitutional element which increases the resistivity of the alloy and reduces the coercive field, so it leads to lower energy losses per (de)magnetization cycle. Thanks to silicon's properties, FeSi alloy is a very good soft magnetic material for electrical machines, where it is responsible for carrying and amplifying the magnetic flux density B. One of the most important properties for a soft magnetic material is the magnetic relative permeability μ, which strongly depends on the crystal direction of the electrical steel; usually, in FeSi based alloys a preferential $< 100 >$ crystal orientation is obtained with a dedicated thermomechanical processing, which generates a textured material (known as grain oriented electrical steel).

The magnetic relative permeability is optimum along any of the crystal direction $< 100 >$. Compared to grain non oriented steels, grain oriented ones present a magnetic relative permeability which is twice higher and much lower magnetic losses (about one order of magnitude). Anyway, until now, grain oriented electrical steel have been mainly used in transformers application, because the locked $< 100 >$ crystal direction cannot be optimal for the requested B path in application which include a rotating field. To make these materials attractive for variable direction magnetic flux applications, author in [4] propose a methodology to change the flux direction according to specific boundary conditions.

A material that can combine the best crystallographic texture and the optimized anisotropy synergy has high potential in terms of machine's performance. In Figure 4.16 a comparison of the total core losses of the printed samples and commercial materials is shown. The figure presents core losses measured at 50–60 Hz, at magnetic polarization of 1 T (10 kGauss), because of the overall lower polarization that can be obtained from the printed samples. Since the total core losses depend on

the geometry of the sample, the physical dimensions are considered through a normalized geometric parameter. Most measurements have been conducted on ring samples, which have an outer dimension that goes from 28 to 60 mm. For solid printed samples, core losses are significant, up to approximately 10 W/kg ($W_{10,50}$), but by refining sample topologies, lower losses were obtained.

The refined samples were built with the introduction of internal airgaps, both parallel and perpendicular to the build direction. In comparison, for typical commercial materials, the total core losses are significantly lower. For NO JNEX super core laminations 0.5 W/kg, for NO 3% FeSi laminations 0.8 W/kg, and for SMC 5 W/kg. The superiority of 3D printed soft magnetic cores to SMC cores is evident per weight. In fact, considering the per volume value, the conclusion made before would not be true, since in 3D printed parts airgaps were introduced with the purpose of reducing the eddy current component, but they increment the volume of the sample.

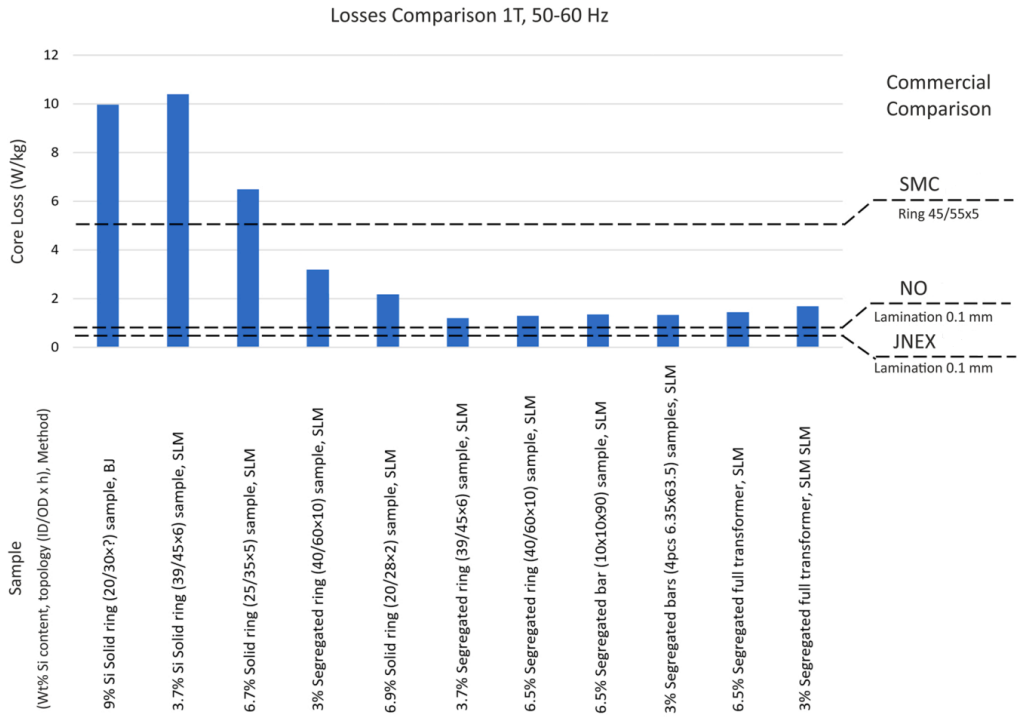

Figure 4.16: Comparison of total core losses of additively manufactured soft magnetic FeSi cores and typical commercial materials from the literature. (ID/OD x h) denotes the topology of the sample – inner diameter/outer diameter x h [35].

Authors in [36] made magnetic measurements on ring samples and the results obtained are resumed below, in function of the laser energy input. It can be noticed

that:

- The maximum permeability is not affected by the first two value of energy input but it starts decreasing when E=420 J/m.
- The μ_{40}, which is the relative magnetic permeability at an applied field strength H=40 A/m, has a non-monotonous behavior with maximum value at E=280 J/m.
- The B_{50}, which is the flux density at an applied field strength H=5000 A/m, has a non-monotonous behavior with maximum value at E=280 J/m.
- The remanence B_r decrease slightly with the increment of the energy input.
- H_c has a non-monotonous behavior with minimum value at E=280 J/m.
- The total power losses have a non-monotonous trend with minimum value at E=280 J/m.

It is evident that in soft magnetic materials a compromise between finer grain structure and large grains should be found. The first one leads to a poorer quasistatic magnetization properties and higher hysteresis losses, otherwise larger grains cause eddy losses to increase. In fact, eddy losses depend on the grain size, since their increment worsens superficial roughness, leading to undesired electrical shorting between walls. In addition, as stated in [37], the optimal grain size depends on the working conditions of the material, such as frequency or working induction.

Manufacturing defects represent pinning sites, which leads to an increment of the coercivity and hysteresis losses and a decreasing of permeability. If large enough, pores and cracks represent airgaps from which demagnetization fields emanate, resulting in sheared B-H curves. As shown in [34], when the energy input is high the sample porosity decreases, so cracks are generated in the part. The crystallographic texture can help to clarify the magnetic behavior of the material treated at high laser energy inputs. As a consequence, the horizontal plane loses its isotropic character. The small grain size obtained with SLM is the factor limiting the magnetic performance of the printed material, for this reason a grain enlargement obtained with an heat treatment, like annealing described before, becomes fundamental for practical applications.

4.4 Hysteresis and Eddy Current Losses

Considering high motor speed, the magnetic losses of electrical machines increase, so magnetic components generate more heat that must be dissipated in the environment, causing an increment of machine's internal temperatures. Focusing on soft magnetic materials application in electrical machines [38], [39], the losses generated inside them can be divided into:

- Hysteresis losses, which are directly related to grain size, texture and structural disorder in the material.
- Eddy current losses, that are generated from induction currents in the core and depends on the electric resistivity of the material.

Eddy currents development is promoted in the material when its size is larger than the skin depth, which can be found according to (4.1).

$$\delta = \frac{1}{(\pi f \sigma \mu)^{0.5}} \tag{4.1}$$

Where σ is the electrical conductivity [S/m]; f is the frequency [Hz]; μ is the magnetic permeability [Vs/Am].

Gargalis et al. in [40] realized an electrical machine with additively manufactured rotor and compared its performance with a conventionally laminated rotor, considering different operating conditions. In the low speed region the behaviour of the two machine was comparable, while at high speed core losses have a significant increment. The optimized geometry of the rotor leads to high efficiency and elevated performance of the machine, but when the speed increase, it is necessary to implement some strategies to reduce the losses generated.

In traditionally manufactured FeSi devices, laminated sheet metal are used; thanks to this configuration, eddy current development is limited and so are its associated power losses. The purpose of authors in [41] is to understand the impact of additively manufactured geometries on power losses. As seen in previous sections the grain structure affects a lot the magnetic performance of soft ferromagnetic materials, so geometries must be designed considering also grain structure development. Eddy

current development should be modeled as a function of cross-sectional geometry and the heat conduction during AM process.

From the schematics of the scan patterns used for additively manufactured thin wall structures by Plotkowski et al. it can be noticed that the scan pattern is rotated by 67° between each layer. In order to increase the energy deposited per layer, a double scan was performed: this technique include a second scan pattern which perform a first scan on each layer equal to the first sample and a second scan oriented paralelly to the sample edge (this procedure should be adopted for all layers).

The solidification cooling rates can be decreased by increasing the energy stored per layer. Then, annealing procedure at 1150 °C was performed, with the purpose of eliminating any residual porosity and enable recrystallization and grain growth to increase the magnetic performance. In [41], the authors could characterize the behavior of the tested components by describing the total losses using the approximated formula reported in (4.2), which comes from Steinmetz law [42].

$$P_{cycle} = c_{hyst}(B)f + c_{eddy}(B)f^2 \tag{4.2}$$

Where P_{cycle} is the total power loss per cycle, f is frequency, c_{hyst} is a coefficient associated with hysteresis (materials) losses and c_{eddy} is a coefficient associated with eddy current losses.

The linear last-square fit performed on the data based on [41] is obtained using (4.3).

$$E_{cycle} = c_{hyst}(B) + c_{eddy}(B)f \tag{4.3}$$

Where E_{cycle} is the total energy loss for a given cycle that is equal to the integrated area of the hysteresis loop.

The linear trend described by (4.3) represents the loss behaviour depending on frequency, showing that this approach can be used to decompose the origins of the energy losses for this material. Using the coefficient c_{hyst} and c_{eddy} as quantitative indicators of the material and eddy current losses, the fraction of power losses due

to eddy current can be computed as follows.

$$F_{eddy} = \frac{c_{eddy} f}{c_{hyst} + c_{eddy} f} \tag{4.4}$$

Plotkowski et al. in [41] compares the ESBD of the bulk cross-sections, highlighting that the single scan pattern shows a chaotic structure with many small grains, while in the double scan pattern an orientation of the $< 100 >$ type crystallographic direction is conserved with larger grains.

The magnetic test results show that the double scan pattern has lower hysteresis loss coefficients, because of the increased strength of the fiber texture which grant a more convenient magnetizing direction. Using (4.4) the fraction of power losses due to eddy current is computed; even if the double scan pattern improves the material properties, it leads to very small improvements in the overall efficiency on a device value. In fact, conventionally, soft magnetic components are produced using laminated sheet metal to confine eddy current loops to the sheet thickness.

To obtain performance similar to the one obtained with laminated configurations, AM should be used to produce thin wall structures. In this way the arising of eddy currents in the material is restrained.

Plotkowski et al. in [41] realized samples of different shape and thickness and did an experimental comparison between the loss behaviour for bulk, thin wall and mesh cross section; the mesh and the bulk components show a similar behaviour, but the mesh one is characterized by a lower saturation inductance.

The structure that shows a lower level of performance is the mesh one; otherwise, the Hilbert structured sample shows a significant improvement, leading to lower values of eddy current loss coefficient.

An heat treatment was made to the samples considered in [41], with the purpose of studying the trend of the loss behaviour after that. The treatment chosen in this case is hot isostatic pressing; after the treatment, it can be noticed a reduction of the hysteresis loss coefficients, and, at the same time, an increment of the eddy current loss coefficient, which is more evident in the thin wall sample with 13 parallel plates. The Hilbert structures seems to be the best one, since it has the lowest eddy current

and hysteresis loss coefficient. Nevertheless, the increase in eddy current losses, the heat treatment brought to a net decrease in power losses. Moreover, thanks to the heat treatment it can be observed also an increment in the effective permeability.

Heat treated samples exhibit an increase in maximum effective permeability and a decrease in the total loss density at an applied field of 3000 A/m. As shown in previous section, heat treatments bring to a grain growth, so that confirm the evidence which shows an increment in permeability (leading to and increment in eddy current losses) and a reduction in hysteresis losses, since materials with larger grains can be magnetized and demagnetized easily.

These factors bring to a reduction of the skin depth, according to (4.1). The results obtained suggests also that the influence of geometry is greater than the effect of manufacturing an ideal composition, since the loss density shows an increment with the increase of the sample mass. In particular, the Hilbert structure sample showed a very good response to heat treatment, being the sample with the lowest loss density and one of the best sample in terms of permeability.

Also in [43], the Hilbert structure is the one which shows the lowest losses compared with other samples and it was used to produce the prototype of a transformer core in AM. Test results showed performance comparable to the conventional non-oriented sheet, as shown in Figure 4.17.

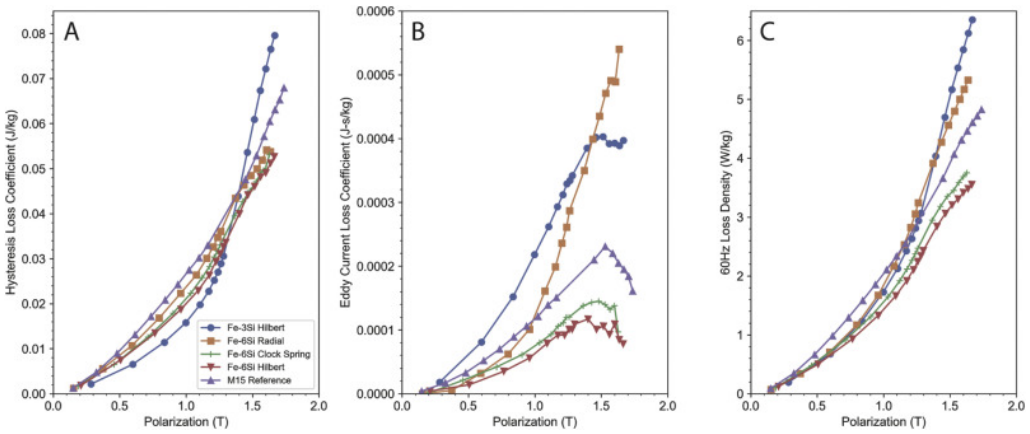

Figure 4.17: Comparison of magnetic performance for the three FeSi6 designs to an FeSi3 Hilbert cross-section and a conventionally laminated non-oriented steel (M15), showing (a) the measured hysteresis loss coefficients and (b) eddy current loss coefficients, as well as (c) the power loss per unit mass for 60 Hz operation by Plotkowski et al. [43]

Anyway, in particular for the FeSi6 alloy, fractures were induced in the AM core due to the high silicon content. It is also important to notice that the 54% of this AM core is made of air, so the majority of the losses generated are due to this pure air insulating, represented in Figure 4.18.

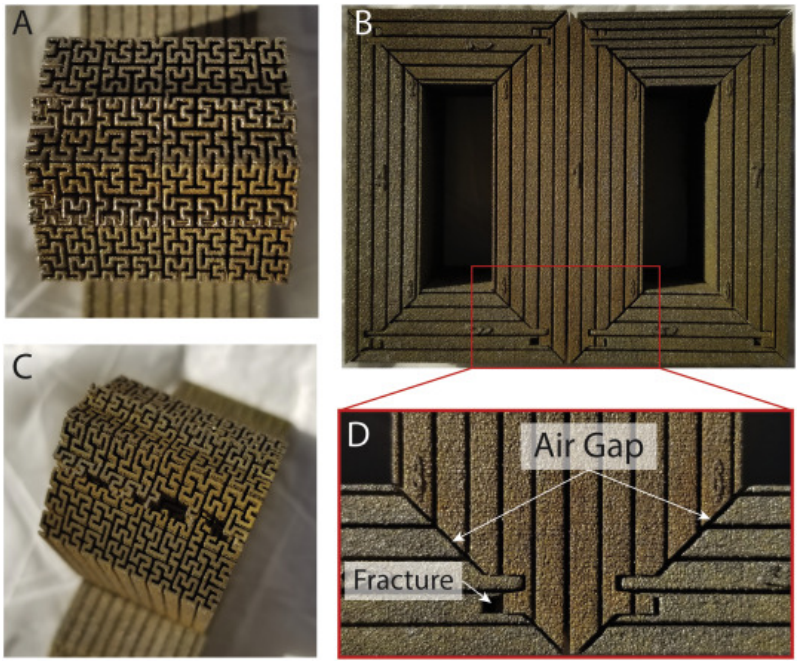

Figure 4.18: Example of one of the FeSi6 transformer cores showing (a) the Hilbert inspired cross-section, (b) the assembled core, (c) examples of fractured features that occurred during machining, and (d) examples of the air gaps at the leg joints by Plotkowski et al. [43]

In [44], the properties of additively manufactured electric steel powder cores with increased Si content, obtained by the definition of the best laser powder bed fusion printing conditions, are presented and compared with commercial FeSi alloys. The analysis shows promising results regarding the magnetic behaviour of FeSi6.5 samples.

In the following, the magnetic characterization of other two FeSi alloys with different silicon content is presented.

4.4.1 Magnetic characterization of FeSi4

In [45] samples from FeSi4 powder were fabricated using SLM to do the magnetic characterization of the material and compare its properties with commercial samples.

The powder used to make the toroidal specimens by SLM is gas-atomized pre-alloyed powder of FeSi with an average silicon content of 3.8-4.1 % and 1.1-1.3% of chronium content, which slightly low magnetic saturation magnetization of the material. In order to achieve less than 2% porosity and avoid macroscopic defects, such as visible cracks, delaminations or uneven growth and photographed in Figure 4.19, the technique of "laser re-melting" was applied, which consists of making two consecutive scans of the same layer before proceeding the fresh powder and making the next layer. This study showed excellent DC magnetic properties, comparable to commercial soft ferromagnetic materials at low magnetization. After the annealing, the Hysteresis losses decrease, but eddy currents increase a lot when the material gets into saturation region. These losses can be reduced introducing some airgaps by realizing a split material internal structure.

Two issues were found in the powder coating of toroidal samples:

- Uneven growth (Figure 4.19 (a)) due to powder balling, caused by uneven powder deposition, which was solved brushing away the excess powder.
- Delaminations (Figure 4.19 (b)), that are generated because of an excessive powder deposition on the printed part.

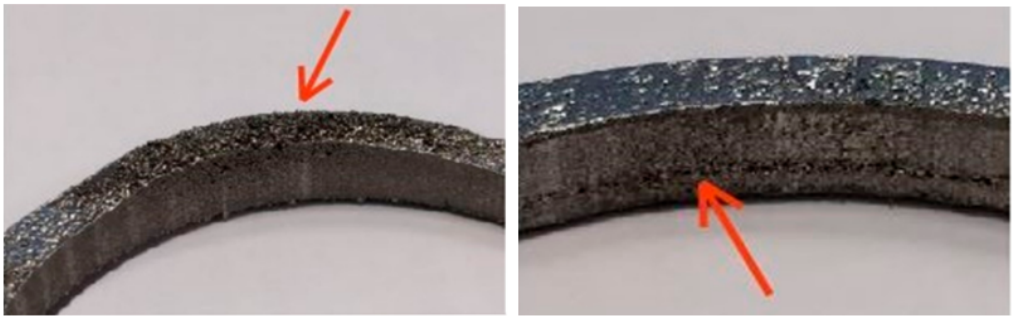

Figure 4.19: Toroid printed with uneven growth and toroid printed with a delaminated layer by Tiismus et al. [45]

In [46], the ring method was used for the measurements of printed material magnetic properties, considering different frequencies: 25 mHz (quasi-static), 1 Hz, 10 Hz and 50 Hz in the magnetizing range of 0.9-1.6 T. The setup was organized in a way similar to [45] and its schematic is reported in Figure 4.20.

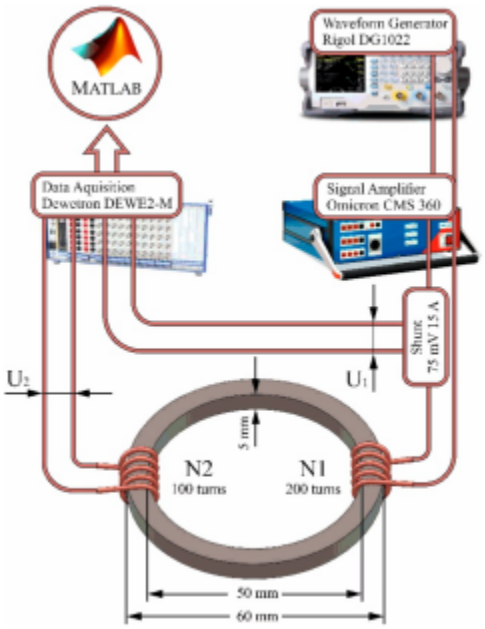

Figure 4.20: Toroid dimensions and the schematic of the hysteris measurements by Tiismus et al. [45]

Where N_1 is the number of turns of the primary coil, N_2 is the number of turns of the secondary coil, I is the instantaneous current value, e is the instantaneous induced electromotive force, l_t is the toroid average length and S is the toroid cross-section area. The magnetic field and the average flux density can be found as follows:

$$H = \frac{N_1 i}{l_t} \tag{4.5}$$

$$B = \frac{1}{N_2 S} \int^t e(t)\, dt \tag{4.6}$$

After constructing the hysteresis curves for measured data, the specific iron losses Ps were calculated as a subtraction of the curve areas and can be expressed as:

$$P_s = \frac{1}{T\varrho} \left(\int_0^T H_1\, dB_1 - \int_0^T H_2\, dB_2 \right) \tag{4.7}$$

Where ϱ is the average density and T is the period. Quasi-static measurements of the sample are presented in Figure 4.21. The sample shows DC magnetic properties that are comparable to commercial and 3D printed soft ferromagnetic materials from the literature. Anyway, it has a low value of saturation (1.3 T at 5000 A/m), while the commercial materials usually has 1.6 T-1.7 T at 5000 A/m. The reduction in saturation magnetization comes from the pinning effect of intragranular porosities on the large recrystallized grains.

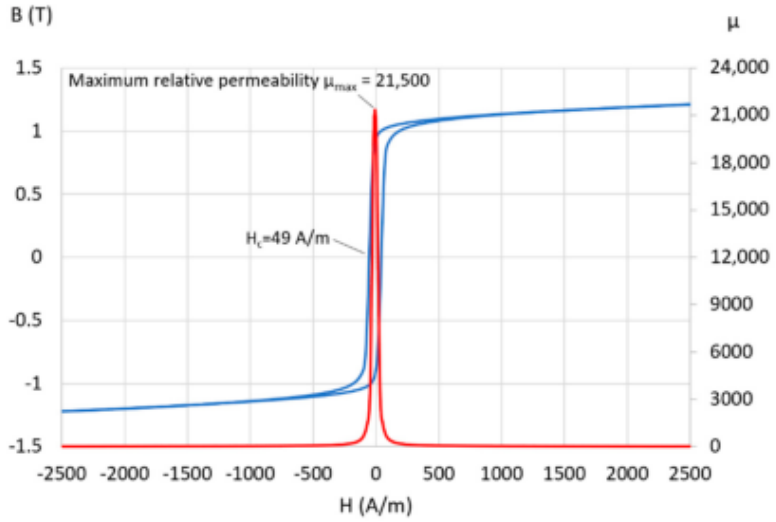

Figure 4.21: Quasi-static hysteresis curve and permeability of the toroid (annealed), Measured with sinusoidal excitation of $2500 A/m$ at $25 mHz$ by Tiismus et al. [45]

A comparison between some parameters obtained in the study and SLM-fabricated FeSi6.7 and FeSi6.9 found in the literature is proposed in Table 6.1.

Table 4.5: Parameters comparison

Parameters	**Component**	
	FeSi4	**FeSi6.7 - FeSi6.9**
Relative permeability	21500	25000-31000
Coercivity [A/m]	49	16
Total iron losses [W/kg]	7-9	0.5-0.7

AC measurements confirmed an increase in iron losses, which are dominated by eddy current losses. Besides, the losses augment their value when the material saturates;

in fact, the losses coefficient goes from 8.17 W/kg (at 1 T) to 83.7 W/kg (at 1.5 T) with the increment of the saturation of the material for the ring sample after the annealing.

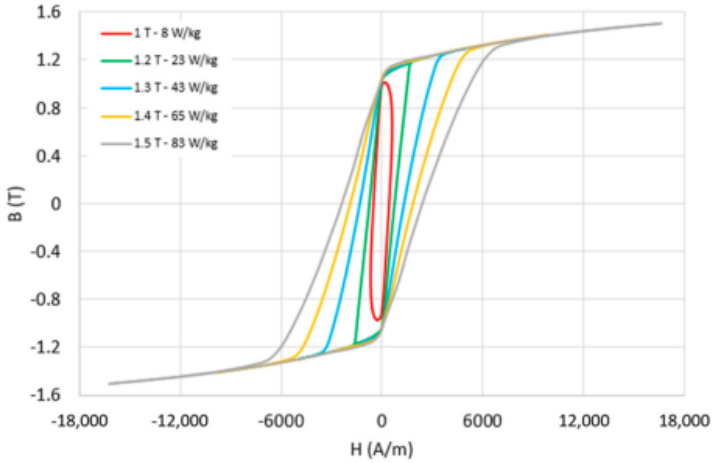

Figure 4.22: Hysteresis curves measured at 50 Hz in the magnetization range of 1-1.5 T (annealed) by Tiismus et al. [45]

4.4.2 Magnetic characterization of FeSi6.7

High silicon FeSi alloy impose strict constraint concerning AM production parameters. As shown in the previous sections and in [34] for high laser energy input, cracks can occur, which negatively affect the magnetic and mechanical properties of the component. In order to obtain an optimized microstructure and good magnetic properties, AM parameters must be properly defined, united with post annealing parameters. In [38], prototypes using FeSi6.7 were realized to do the magnetic characterization of the material.

Heat treatment like annealing showed a positive effect on the hysteresis losses generated by the material. In fact, the hysteresis losses decrease with the increasing of the laser power only for the annealed material; on the other side, for the as built sample the opposite effect is encountered. This can be explained by the fact that with higher laser power, the cooling rate decreases, leading to a larger average grain size and, consequently, lower losses. Anyway, a good balance between laser power and optimized magnetic performance should be found, since with a too high laser power the material tends to generate residual stresses and therefore crack formation is enhanced.

The maximum permeability reached by the FeSi6.7 is 31000 at H=24 A/m for the optimized sample. This value is much higher than the one reported in literature for FeSi6.9 (24000) [29]. The core losses are also studied and they can be separated into hysteresis losses P_h and eddy current losses P_e; both of them increase with the increment of the frequency. It is evident that to obtain good performance in high frequency applications, the eddy current losses must be reduced significantly.

Then the DC hysteresis loop of additively manufactured FeSi6.7 (optimized) is compared with common commercial electrical steel and SMC material. The additively manufactured sample showed the lowest value of coercivity ($H_c = 16\frac{A}{m}$), the highest maximum permeability (31000) and largest remanence ($J_r = 1.26T$). So, the DC properties of additively manufactured FeSi6.7 can compete with conventional electrical steel.

4.4.3 Adding boron to FeSi alloys

It is known that high iron loss due to eddy current affects the additive manufactured bulk iron cores. Pham et al. [47] have already showed that adding boron for binder jet printing of FeSi reduces the hysteresis losses, so S.N.Foster et al. [48] found a nonlinear relation between boron particle size and magnetic properties.

For their studies S.N.Foster et al. used three binder jetting printed samples with the same identical boron content but with different boron particle size:

- boron particle size of sample 1: 0.1 μm;
- boron particle size of sample 2: 0.5 μm;
- boron particle size of sample 3: 1.0 μm.

The experimental results of the quasi-static at 1Hz testing for DC characterization show that the maximum relative permeability $\mu_{r,max}$, the magnetic flux density B_5, B_{25} and B_{100} (at 500, 2500 and 10000 A/m respectively) are pretty the same even if the particle size changes; otherwise, the intrinsic coercivity H_c and the correspondent hysteresis losses per cycle, P_h/f , change non-linearly with the boron particle size changing.

The core loss density are maximum for the sample with the biggest boron particle size for all frequencies and for all magnetic flux density. So, decreasing the boron particle

size is possible to reduce the core losses, even if there isn't a linear correspondence between the specific core losses reducing and the boron particle size.

S.N.Foster et al. simulated also a 48-slot/8-pole interior permanent magnet machine with the BJP core made of, alternatively, of the three material studied and the 2D FEA simulation confirms what experimental tests showed. Indeed, the combined hysteresis loss as function of the speed decreases with the growing of the boron particle size, while the combined eddy current loss as function of the speed increases with the growing of the boron particle size.

In the end, comparing the simulated iron loss at the maximum torque in the speed range the IPM machine with smallest boron particle size shows the lowest iron loss and the highest efficiency.

4.5 Multi Material Additive Manufacturing

The initial adoption of AM in electrical machine design focused on the geometric optimization of single component, such as integrated heat exchangers or variable-section windings, but the true technological frontier is represented by Multi-Material Additive Manufacturing (MMAM). This approach enables the simultaneous or sequential deposition of materials with divergent physical properties (conductors, insulators, and ferromagnetic materials) within a single production process.

A primary limitation of conventional electric motors lies in the discrete nature of their components. The mechanical assembly of copper, magnetic steel, and polymeric or ceramic insulators introduces contact thermal resistances and mechanical parasitic effects.

MMAM offers the potential to overcome these barriers through:

- functionally graded materials: creating gradual transitions between dissimilar metals (e.g., copper and steel) to mitigate residual stresses arising from differences in the coefficients of thermal expansion (α);
- integrated insulation: depositing dielectric ceramic layers directly onto the conductors during the build process. This eliminates the need for traditional impregnation resins and significantly increases the slot fill factor (k_{cu}).

In addition, the ability to locally vary material composition allows for tailoring the magnetic properties of the core. Utilizing techniques such as Directed Energy Deposition or multi-material Binder Jetting, it is possible to achieve eddy current mitigation and active thermal management.

In this context, authors in [49] provide a significant benchmark for the application of multi-material additive manufacturing to electrical machines. By investigating a Permanent Magnet (PM) generator, the authors demonstrate that the simultaneous deposition of shaped-profile copper conductors and ceramic insulation layers allows for a radical departure from traditional winding constraints. Their study highlights that the direct integration of ceramic dielectrics—which possess a thermal conductivity significantly higher than conventional organic resins—enables a superior heat dissipation path. Furthermore, the use of 'shaped-profile' geometries tailored to the magnetic flux lines facilitates a simultaneous reduction in AC proximity losses and an increase in the slot fill factor. According to their findings, this multi-material approach not only improves the thermal envelope, potentially reducing hot-spot temperatures by up to 30°C, but also enhances the overall power density and efficiency of the machine across its operating range.

Complementary to the optimization of windings, the strategic application of Multi-Material Additive Manufacturing (MMAM) in rotor structures offers a transformative approach to electromagnetic performance, as demonstrated by [50]. Their research focuses on Synchronous Reluctance Machines (SynRMs), specifically addressing the critical role of rotor edge bridges. Traditionally, these bridges are necessary for structural integrity but act as leakage paths for magnetic flux, thereby increasing quadrature inductance (L_q) and limiting the saliency ratio. By employing MMAM to strategically combine magnetic and non-magnetic materials within the rotor's architecture, authors illustrate how local material tailoring can suppress these parasitic flux paths. This localized material functionalization leads to a significant enhancement of the machine's torque density and efficiency. Their findings underscore that MMAM is not merely a geometric tool but a means to achieve a superior electromagnetic design that is physically unattainable through conventional single-material subtractive or formative manufacturing processes.

Despite its potential, applying MMAM to electric motors faces non-trivial metal-

lurgical challenges. Disparities in optical reflectivity (in laser-based processes) and differing melting/sintering temperatures can lead to:

- brittle intermetallic phases at the interface of dissimilar materials;
- localized porosity caused by the distinct dynamics of the melt pool for each material.

4.6 Conclusions

In this chapter a general presentation of the state-of-the-art of additive manufacturing applied to electric motors is presented. Post-processing treatments such as annealing are very important since they give the material better mechanical and magnetic properties. In fact, the crystallographic structure and grain dimensions of the material, which are highly influenced by post-processing treatments and the AM input parameters, are fundamental to obtain the best material properties in terms of mechanical resistance and magnetic performance. In the last section of the paper, the problem of eddy currents' development and hysteresis losses was explored, and the magnetic characterization of some common alloys was proposed. The main problem in losses' generation is due to the fact that the AM material is generated as a block, so eddy current development is favored. The main solutions found in the literature propose finding an optimal laminated structure that can lead to a reduction of the power losses' generation in the material by exploiting the main advantage of AM, which is the possibility to produce optimized geometries. In the end potentialities and challenges of multi material additive manufacturing applied to electric motors are presented and discussed.

To conclude, AM is a promising technique for EM fabrication since it allows obtaining optimized geometries for particular motors, and by focusing on the study of the losses' development, also a good compromise can be found that can limit their generation inside the material.

4.7 References

[1] R. Wrobel and B. Mecrow, «A comprehensive review of additive manufacturing in construction of electrical machines», *IEEE Transactions on*

Energy Conversion, vol. 35, no. 2, pp. 1054–1064, 2020, doi:10.1109/TEC.2020.2964942.

[2] A. Selema, M. N. Ibrahim, and P. Sergeant, «Metal additive manufacturing for electrical machines: Technology review and latest advancements», *Energies*, vol. 15, no. 3, 2022, doi:10.3390/en15031076, ISSN: 1996-1073.

[3] H. Tiismus, A. Kallaste, T. Vaimann, and A. Rassõlkin, «State of the art of additively manufactured electromagnetic materials for topology optimized electrical machines», *Additive Manufacturing*, vol. 55, p. 102 778, 2022, ISSN: 2214-8604.

[4] E. A. Périgo and D. Tremelling, «Grain-oriented magnetic particles for energy applications», *IEEE Magnetics Letters*, vol. 9, pp. 1–4, 2018.

[5] S. Hussain, A. Kallaste, and T. Vaimann, «Recent trends in additive manufacturing and topology optimization of reluctance machines», *Energies*, vol. 16, no. 9, 2023, doi:10.3390/en16093840, ISSN: 1996-1073.

[6] M. U. Naseer, A. Kallaste, B. Asad, T. Vaimann, and A. Rassõlkin, «A review on additive manufacturing possibilities for electrical machines», *Energies*, vol. 14, no. 7, p. 1940, Mar. 2021, doi:10.1109/TIE.2018.2801805, ISSN: 1996-1073.

[7] G. Stornelli, P. Folgarait, M. R. Ridolfi, *et al.*, «Feasibility study of ferromagnetic cores fabrication by additive manufacturing process», *Materials Proceedings*, vol. 3, no. 1, 2021, doi:10.3390/IEC2M-09241, ISSN: 2673-4605.

[8] B. Khatri, K. Lappe, D. Noetzel, K. Pursche, and T. Hanemann, «A 3D-Printable polymer-metal soft-magnetic functional composite—development and characterization», *Materials*, vol. 11, no. 2, 2018, doi:10.3390/ma11020189, ISSN: 1996-1944.

[9] S. Saunders, *GE Aviation Announces 100,000th 3D Printed Fuel Nozzle Shipped from Auburn Plant*, August 18, 2021.

[10] Web-redactor, *Porsche present 40% lighter 3d printed electric drive housing*, `https://additiv-tech.ru/en/news/porsche-present-40-lighter-3d-printed-electric-drive-housing.html`, Dec. 2020.

[11] E. Aguilera, J. Ramos, D. Espalin, *et al.*, «3d printing of electro mechanical system», *International Solid Freeform Fabrication Symposium. University of Texas at Austin.*, 2013, http://dx.doi.org/10.26153/tsw/15649.

[12] S. Lammers, G. Adam, H. J. Schmid, *et al.*, «Additive manufacturing of a lightweight rotor for a permanent magnet synchronous machine», in *2016 6th International Electric Drives Production Conference (EDPC)*, doi:10.1109/EDPC.2016.7851312, 2016, pp. 41–45.

[13] H. Tiismus, A. Kallaste, A. Belahcen, A. Rassolkin, T. Vaimann, and P. Shams Ghahfarokhi, «Additive manufacturing and performance of e-type transformer core», *Energies*, vol. 14, no. 11, 2021, doi:10.3390/en14113278, ISSN: 1996-1073.

[14] C. Bianchini, G. Sala, A. Torreggiani, *et al.*, «Synchronous reluctance tubular machine by means of additive manufacturing», in *2022 International Conference on Electrical Machines (ICEM)*, doi:10.1109/ICEM51905.2022.9910808, 2022, pp. 921–927.

[15] A. Selema, M. N. Ibrahim, and P. Sergeant, «Development of novel semi-stranded windings for high speed electrical machines enabled by additive manufacturing», *Applied Sciences*, vol. 13, no. 3, 2023, doi:10.3390/app13031653, ISSN: 2076-3417.

[16] J. Robinson, S. P. Munagala, A. Arjunan, *et al.*, «Electrical conductivity of additively manufactured copper and silver for electrical winding applications», *Materials*, vol. 15, no. 21, 2022, doi:10.3390/ma15217563, ISSN: 1996-1944.

[17] V. E. Vavilov, F. R. Ismagilov, E. I. Zaynagutdinova, *et al.*, «Improving the processibility of manufacturing windings of electrical machines using additive manufacturing methods: Experience of using A1Si10Mg and carbon nanotubes», in *2021 International Conference on Electrotechnical Complexes and Systems (ICOECS)*, doi:10.1109/ICOECS52783.2021.9657373, 2021, pp. 636–641.

[18] L. Szabó, «Survey on applying 3d printing in manufacturing the cooling systems of electrical machines», in *2022 IEEE International Conference on Automation, Quality and Testing, Robotics (AQTR)*, doi:10.1109/AQTR55203.2022.9801983, 2022, pp. 1–6.

[19] M. Sarap, A. Kallaste, P. Shams Ghahfarokhi, H. Tiismus, and T. Vaimann, «Utilization of additive manufacturing in the thermal design of electrical machines: A review», *Machines*, vol. 10, no. 4, 2022, doi:10.3390/machines10040251, ISSN: 2075-1702.

[20] K. Gruber, I. Smolina, M. Kasprowicz, and T. Kurzynowski, «Evaluation of inconel 718 metallic powder to optimize the reuse of powder and to improve the performance and sustainability of the laser powder bed fusion (lpbf) process», *Materials*, vol. 14, no. 6, 2021, doi:10.3390/ma14061538, ISSN: 1996-1944.

[21] A. Selema, M. N. Ibrahim, and P. Sergeant, «Development of novel semi-stranded windings for high speed electrical machines enabled by additive manufacturing», *Applied Sciences*, vol. 13, no. 3, 2023, doi:10.3390/app13031653, ISSN: 2076-3417.

[22] ASTM, *Additive manufacturing — General principles — Fundamentals and vocabulary*, ISO/ASTM52900-21, Mar. 2022.

[23] Mesago, *AM Field Guide Compact*, published with the collaboration of Reutlingen University, find more information at formnext.com, September, 2022.

[24] M. K. H. R., M. G. M. Benal, P. K. G. S., *et al.*, «Influence of short glass fibre reinforcement on mechanical properties of 3d printed abs-based polymer composites», *Polymers*, vol. 14, no. 6, 2022, doi:10.3390/polym14061182, ISSN: 2073-4360.

[25] A. S. Budiman, R. Sahay, K. Agarwal, *et al.*, «Modeling impact mechanics of 3d helicoidally architected polymer composites enabled by additive manufacturing for lightweight silicon photovoltaics technology», *Polymers*, vol. 14, no. 6, 2022, ISSN: 2073-4360.

[26] H. Tiismus, A. Kallaste, A. Belahcen, A. Rassõlkin, and T. Vaimann, «Challenges of additive manufacturing of electrical machines», in *2019 IEEE 12th International Symposium on Diagnostics for Electrical Machines, Power Electronics and Drives (SDEMPED)*, doi:10.1109/DEMPED.2019.8864850, 2019, pp. 44–48.

[27] C. Sirisathitkul and Y. Sirisathitkul, «Recent developments in 3d printing of rare-earth-free permanent magnets», *Inventions*, vol. 7, no. 3, 2022, ISSN: 2411-5134.

[28] A. Mostafaei, C. Zhao, Y. He, *et al.*, «Defects and anomalies in powder bed fusion metal additive manufacturing», *Current Opinion in Solid State and Materials Science*, vol. 26, no. 2, p. 100 974, 2022, doi.org/10.1016/j.cossms.2021.100974, ISSN: 1359-0286.

[29] M. Garibaldi, I. Ashcroft, J. Lemke, M. Simonelli, and R. Hague, «Effect of annealing on the microstructure and magnetic properties of soft magnetic fe-si produced via laser additive manufacturing», *Scripta Materialia*, vol. 142, pp. 121–125, 2018, doi:10.1016/j.scriptamat.2017.08.042, ISSN: 1359-6462.

[30] T. Riipinen, S. Metsä-Kortelainen, T. Lindroos, J. Keränen, A. Manninen, and J. Pippuri-Mäkeläinen, «Properties of soft magnetic fe-co-v alloy produced by laser powder bed fusion», *Rapid Prototyping Journal*, vol. 25, no. 4, pp. 699–707, 2019.

[31] T. Lindroos, T. Riipinen, S. Metsä-Kortelainen, J. Pippuri-Mäkeläinen, and A. Manninen, «Lessons learnt-additive manufacturing of iron cobalt based soft magnetic materials», *Journal of Magnetism and Magnetic Materials*, vol. 563, p. 169 977, 2022.

[32] R. Sundar and S. Deevi, «Soft magnetic feco alloys: Alloy development, processing, and properties», *International Materials Reviews*, vol. 50, no. 3, pp. 157–192, 2005. DOI: 10.1179/174328005X14339.

[33] M. De Campos, F. Landgraf, N. da Silva, E. da Costa, N. Cheung, and A. Baddorf, «On the optimal grain size for minimizing the total power loss in electrical steels», *Journal of Magnetism and Magnetic Materials*, vol. 424, pp. 304–310, 2017, ISSN: 0304-8853. DOI: https://doi.org/10.1016/j.jmmm.2016.10.014.

[34] M. Garibaldi, I. Ashcroft, M. Simonelli, and R. Hague, «Metallurgy of high-silicon steel parts produced using selective laser melting», *Acta Materialia*, vol. 110, pp. 207–216, 2016, https://doi.org/10.1016/j.actamat.2016.03.037, ISSN: 1359-6454.

[35] ®. S. M. Composites, *technical data smc*, August 26, 2021.

[36] M. Garibaldi, I. Ashcroft, N. Hillier, S. Harmon, and R. Hague, «Relationship between laser energy input, microstructures and magnetic properties of selective laser melted fe-6.9%wt si soft magnets», *Materials Characterization*, vol. 143, pp. 144–151, 2018, https://doi.org/10.1016/j.matchar.2018.01.016, ISSN: 1044-5803.

[37] M. de Campos, J. Teixeira, and F. Landgraf, «The optimum grain size for minimizing energy losses in iron», *Journal of Magnetism and Magnetic Materials*, vol. 301, no. 1, pp. 94–99, 2006, doi:10.1016/j.jmmm.2005.06.014, ISSN: 0304-8853.

[38] D. Goll, D. Schuller, G. Martinek, *et al.*, «Additive manufacturing of soft magnetic materials and components», *Additive Manufacturing*, vol. 27, pp. 428–439, 2019, https://doi.org/10.1016/j.addma.2019.02.021, ISSN: 2214-8604.

[39] H. Tiismus, A. Kallaste, A. Belahcen, *et al.*, «Ac magnetic loss reduction of slm processed fe-si for additive manufacturing of electrical machines», *Energies*, vol. 14, no. 5, 2021, doi:10.3390/en14051241, ISSN: 1996-1073.

[40] L. Gargalis, V. Madonna, P. Giangrande, *et al.*, «Additive manufacturing and testing of a soft magnetic rotor for a switched reluctance motor», *IEEE Access*, vol. 8, Nov. 2020, doi:10.1109/ACCESS.2020.3037190.

[41] A. Plotkowski, J. Pries, F. List, *et al.*, «Influence of scan pattern and geometry on the microstructure and soft-magnetic performance of additively manufactured fe-si», *Additive Manufacturing*, vol. 29, p. 100 781, 2019, https://doi.org/10.1016/j.addma.2019.100781, ISSN: 2214-8604.

[42] C. Steinmetz, «On the law of hysteresis», *Proceedings of the IEEE*, vol. 72, no. 2, pp. 197–221, 1984, doi:10.1109/PROC.1984.12842.

[43] A. Plotkowski, K. Carver, F. List, *et al.*, «Design and performance of an additively manufactured high-si transformer core», *Materials & Design*, vol. 194, p. 108 894, 2020, doi.org/10.1016/j.matdes.2020.108894, ISSN: 0264-1275.

[44] G. Stornelli, A. Faba, A. Di Schino, *et al.*, «Properties of additively manufactured electric steel powder cores with increased si content», *Materials*, vol. 14, no. 6, 2021, doi:10.3390/ma14061489, ISSN: 1996-1944.

[45] H. Tiismus, A. Kallaste, A. Belahcen, T. Vaimann, A. Rassõlkin, and D. Lukichev, «Hysteresis measurements and numerical losses segregation of additively manufactured silicon steel for 3d printing electrical machines», *Applied Sciences*, vol. 10, no. 18, 2020, doi:10.3390/app10186515, ISSN: 2076-3417.

[46] H. Tiismus, A. Kallaste, A. Belahcen, *et al.*, «Ac magnetic loss reduction of slm processed fe-si for additive manufacturing of electrical machines», *Energies*, vol. 14, no. 5, 2021, doi:10.3390/en14051241, ISSN: 1996-1073.

[47] T. Q. Pham, H. Suen, P. Kwon, and S. N. Foster, «Reduction in hysteresis loss of binder jet printed iron silicon», in *2020 International Conference on Electrical Machines (ICEM)*, doi:10.1109/ICEM49940.2020.9270774, Gothenburg: IEEE Press, 2020, pp. 1669–1675.

[48] K. J. Islam, T. Q. Pham, H. Suen, *et al.*, «Eddy current loss reduction in binder jet printed iron silicon», pp. 01–07, 2022, doi:10.1109/ECCE50734.2022.9947593.

[49] N. Simpson, J. Jung, A. Helm, and P. Mellor, «Additive manufacturing of a conformal hybrid-strand concentrated winding topology for minimal ac loss in electrical machines», in *2021 IEEE Energy Conversion Congress and Exposition (ECCE)*, 2021, pp. 3844–3851. DOI: 10.1109/ECCE47101.2021.9595059.

[50] S. Akbar, Y. T. Bekele, A. Ebrahimi, and B. Ponick, «Enhanced design and electromagnetic analysis of synchronous reluctance machines using multi-material additive manufacturing», in *2025 IEEE International Electric Machines Drives Conference (IEMDC)*, 2025, pp. 396–401. DOI: 10.1109/IEMDC60492.2025.11061042.

5. Synchronous Reluctance Tubular Machine by means of Additive Manufacturing: Analytical Model, 2D FEA Simulations and Experimental results

Tubular electric motors represent a specific class of linear actuators characterized by their cylindrical geometry, which provides compactness, symmetry, and high force density. Among them, Permanent Magnet Tubular Motors are particularly attractive due to their excellent dynamic performance, high efficiency, and direct linear motion without mechanical transmission elements. These machines are widely employed in precision applications such as robotics, medical devices, and transportation systems where smooth force production and fast response are essential.

However, the performance advantages of permanent magnet machines rely heavily on the use of rare-earth materials, such as neodymium or dysprosium, which exhibit high remanence and coercivity. The limited availability and geopolitical concentration of these materials lead to supply risks and cost fluctuations, motivating the search for alternative motor technologies that can maintain high performance while reducing or eliminating rare-earth dependence. Furthermore, environmental and economic considerations are encouraging researchers and manufacturers to explore more sustainable design solutions.

In this context, tubular reluctance motors have emerged as a promising alternative. These machines operate without permanent magnets, relying instead on the variation of magnetic reluctance to generate motion. Synchronous tubular reluctance machine are characterized by a complex magnetic structures and intricate geometries, which lead to significant manufacturing challenges when using traditional production techniques.

Recent progress in Additive Manufacturing offers a compelling solution to this problem. The layer-by-layer fabrication approach of AM enables the realization of so-

phisticated flux paths, optimized topologies, and integrated cooling or structural features that were previously impractical. As a result, the combination of reluctance motor design and additive manufacturing opens new possibilities for creating efficient, sustainable, and compact tubular actuators suitable for next-generation electromechanical systems.

This chapter deals with the design and optimization of a synchronous tubular reluctance machine, whose plunger is fabricated through additive manufacturing. In the end a feasibility assessment and some experimental results are reported to validate the proposed design and the analytical modeling.

5.1 General Overview

Tubular linear electrical machines (TL) are a particular subset of linear machines. Linear machines present many advantages with respect to their rotating counterparts such as direct motion (e.g no need of additional mechanical parts), resulting in high dynamic and position accuracy. In addition to the aforementioned advantages, the axial-symmetry geometry of the TL machine ensures theoretically null radial force components, thus only the axial oriented force is produced, simplifying plunger bearing support structures requirements.

The most studied TL topology is the permanent-magnet machine (TL-PM) because of its high force density and high dynamic performance. In [1], the authors present accurate analytical models to analyze and design different topologies of TP-PM (e.g. surface and interior permanent-magnet and Halback rotor). Further analysis on the TL-PM motors were carried out on the influence of the inner to outer diameter ratio on the output force [2]. An analytical study on different TL-PM topologies is presented and validated via 2-D and 3-D finite element analysis (FEA).

In literature another studied TL topology is the switched reluctance (SR) one. The authors of [3] present an optimal design approach for SR-TL motor adopting both reluctance network modeling and 2-D FEA. A comparison between PM-TL and SR-TL motor in terms of static force production capability is addressed in [4].

The pure reluctance (SynR) topology for TL was not fully investigated because of the high complexity of the plunger's geometry and the lower force density with respect

to the TL-PM. The resulting intricate rotor geometry affects the manufacturing process since it results in complex fabrication and longer construction times, higher material waste and low stiffness [5].

The metal addictive manufacturing (AM) techniques could help to overcome the manufacturing drawbacks related with the SynR-TL topology, in addition by virtue of freedom of the AM more optimized rotor geometries can be adopted to increase SynR-TL performance.

In addition, the interest towards electrical machines without permanent-magnets (PMs), particularly the ones with rare-earths (REs) composition, has remarkably increased in the last decade.

Rare-earths PMs entered in the market around 1980s and introduced a revolution for the EM sector because of their high energy density with respect to the existing hard magnetic materials. Rare-earths, however, present a series of drawbacks related to cost, availability and sustainability.

The most widespread hard magnetic materials are: Neodynium-Iron-Boron ($NdFeB$), Samarium-Cobalt ($Sm2Co17$), ferrite and alnico. Among them, $NdFeB$ is the most common one in consequence of its superior magnetic properties, but it is listed as a critical material because of its high risk in supply [6].

The most critical drawbacks of REs magnets are their future availability and the related environmental footprint [7]. Moreover, the high price uncertainty [8] and efforts in energy efficiency policies [9],[10] moved the interest of electrical machine manufacturers towards EMs with a lower amount of REs or even without REs.

In this context, synchronous reluctance motors (SynR) are gaining the industry's attention, thanks to theirs high efficiency and the absence of PMs. SynR allows not only to meet the aforementioned requirements of low cost and sustainability, but also to increase efficiency using cost-effective solutions [8], [11].

The biggest motor manufacturers and research institutions are working on the reluctance alternative and the industrial acceptance of the SynR is a matter of time [12].

In the following, the optimal design of a SynR tubular linear machine via 2-D finite element analysis along with its effective realization by means of Additive Manufac-

turing (AM) is presented. The proposed linear actuator is specifically designed for integration into an industrial oven environment. The target force is 60 N and the geometrical constraints are maximum 50 mm for the external diameter and maximum 200 mm for the total length of the actuator.

Figure 5.1 shows the proposed machine geometry.

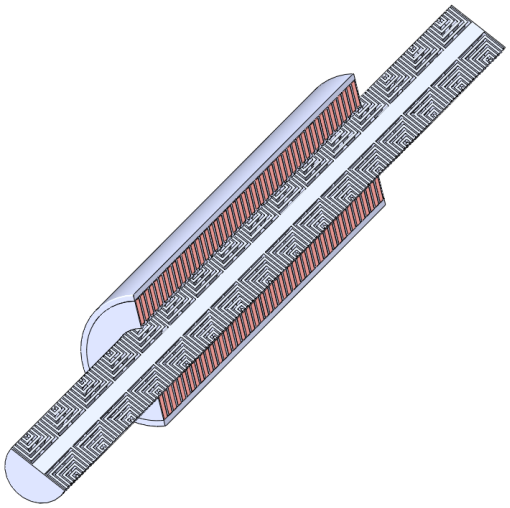

Figure 5.1: Cross-section of the 3-D rendering of the proposed SynR-TL actuator.

5.2 Synchronous Reluctance Machine Design

Synchronous reluctance motors exploit magnetic reluctance to produce torque. The big difference with PM electrical machines seen previously is that they do not have permanent magnets in the rotor, but there are some grooves which are called flux barriers and are essential to guide the magnetic flux in the direction of the direct axis (see Figure 5.2). Flux barriers can be filled with resins to increase mechanical rigidity.

Rotor rotates at a speed which is synchronous with the magnetic field with no current conductive parts. Rotor losses are minimized compared to the one generated in an induction machine. One motivation to develop synchronous reluctance motors is to assess its suitability as an alternative actuator for high precision tools. Permanent magnets are a high-cost components and they also attract metallic swarf in a harsh environment such as in a machine tool.

The most used hard magnetic materials are Neodymium-Iron-Boron (NdFeB),

Figure 5.2: Example of a pure reluctance rotor.

Samarium-Cobalt (Sm2Co17), ferrite and AlNiCo. Among them, Neodymium-Iron-Boron is the most common thanks to its superior magnetic properties, but both Nd and Dy, needed to increase the magnet's stability at higher temperatures, are rare-earths (REs), so presents a series of drawbacks related to cost, availability and sustainability.

The most critical drawbacks of REs magnets are their future availability and the related environmental footprint. In fact, their sourcing and manufacturing processes are very carbon intensive, and their recycling is still immature. The high price uncertainty and efforts in energy efficiency policies, moved the interest of electrical machine manufacturers towards electrical machines with a lower amount of REs or even without REs.

In this context, synchronous reluctance motors are gaining industry's attention, thanks to their high efficiency and the absence of permanent magnets. In fact, they allow not only to meet the previously mentioned requirements of low cost and sustainability, but also to increase efficiency using cost-effective solutions. Another advantage of synchronous reluctance motors is that they can be more easily tolerated under overload conditions, because, since they do not have permanent magnets, there is no risk of demagnetization. Generally, to generate higher torque, anisotropy is needed. In order to obtain anisotropy, it is convenient to have a lot of flux barriers; for this reason, additive manufacturing can be a very useful technology to produce these geometries, which can become more and more complex when a high number of flux barriers is required.

5.2.1 *D-Q* Axis Reference Frame for Synchronous Reluctance Machine

The convention used for synchronous reluctance machines (SyR) states that the d-axis is oriented along the direction of maximum inductance of the rotor ($L_d > L_q$). This convention is generally used for SyR and PMASR (Permanent Magnet Assisted Synchronous Reluctance) motors, in which the magnet flux vector λ_m is oriented along the negative direction of q-axis.

So, the two-axis rotational reference of pure reluctance synchronous machines has a different convention, with respect to the general axis convention of PM synchronous machines, corresponding to an axis rotation of 90° of the conventional d-q reference.

According to this, the role of the synchronous inductances $L_d - L_q$ is reversed; thus, the direct axis corresponds to the plunger magnetic path with the lowest reluctance for each pole. In the following discussion, the two-axis rotational frame of SyR machines will be denoted with capitol letters $D - Q$ in order to distinguish it from the one used for PM machines (see Figure 5.3).

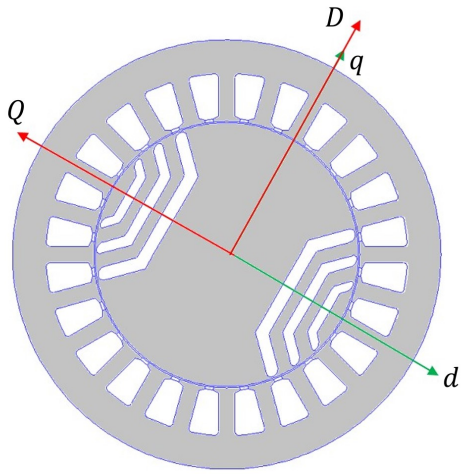

Figure 5.3: Two-axis rotational reference frame of pure synchronous reluctance machine compared against the classic PM reference frame.

Accordingly to the 90° rotation, inductances should be referred to the D-Q axis reference.

$$L_D = L_q \tag{5.1}$$

$$L_Q = L_d \tag{5.2}$$

The 90° rotation modifies the expression of the saliency ratio ξ as denoted in (5.3), which for synchronous reluctance machines is greater than 1. In fact, synchronous reluctance machines and permanent magnet assisted machines are anisotropic because there are magnetic paths with different magnetic permeance values, given by the flux barriers, which build preferential paths for the magnetic linkage flux. Generally, to generate higher torque, anisotropy is needed. In order to get anisotropy, it is convenient to introduce a number of flux barriers and additive manufacturing can be a very useful technology to produce these intricate geometries, which can become more and more complex when a high number of flux barriers is required.

$$\xi = \frac{L_D}{L_Q} \tag{5.3}$$

The expression of the torque for synchronous reluctance machines can be written using the D-Q axis reference. The ideal SynR machine has an infinite permeance on the D-axis and infinite reluctance on the Q-axis, as shown in the following figure: this leads to a torque angle of 90° and unitary power factor. In real situations, however, the actual SyR machine has a magnetization current and a flux along q-axis different from zero.

$$T_{electr} = \frac{3}{2}(L_D - L_Q) i_D i_Q \tag{5.4}$$

The D and Q inductances can be split in two terms: the magnetizing inductance L_m and a leakage inductance L_σ.

$$\begin{cases} L_{sD} = L_\sigma + L_{mD} \\ L_{sQ} = L_\sigma + L_{mQ} \end{cases} \tag{5.5}$$

The leakage term L_σ can be omitted in (5.4), since the leakage flux does not contribute to torque production, therefore the torque equation could be expressed by the magnetizing terms only as in (5.6).

$$T_{electr} = \frac{3}{2}(L_{mD} - L_{mQ}) i_D i_Q \tag{5.6}$$

5.2.2 D-Axis Inductance Computation

To compute the magnetizing inductance on the D-axis, the winding function should be introduced. The winding function $N(\theta)$ is a numerical function that can be used to model the machine winding and the airgap. It can be found from the counting function $n(\theta)$, which depends on the number of wires in the machine.

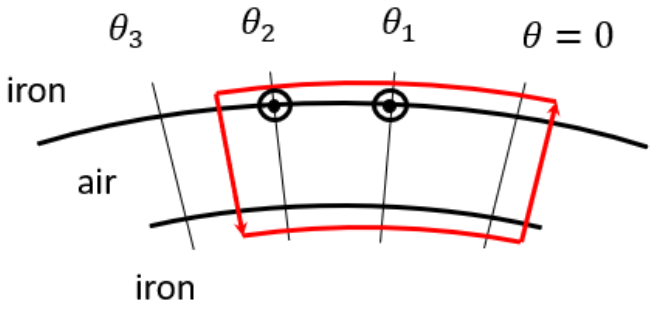

Figure 5.4: Flux path in an example machine.

Applying the Ampère's law to the path reported in Figure 5.4, the counting function should be used. It is ecpressed as in (5.7) where g is the mechanical airgap of the machine.

$$H(\theta) \cdot g - H(0) \cdot g = n(\theta) \cdot i \tag{5.7}$$

The counting function is a staircase function always positive, so with a non-zero mean value, that depends on the starting point which is considered.

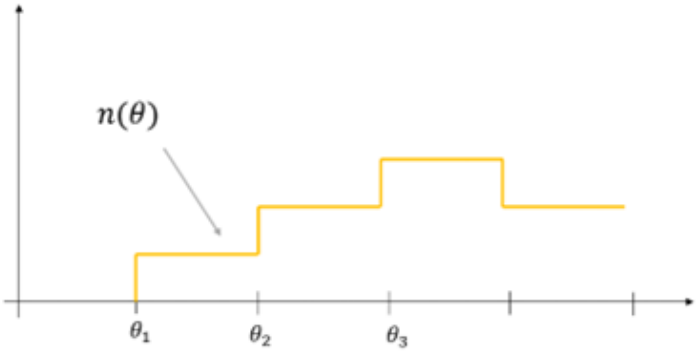

Figure 5.5: Counting function.

From (5.7), the value of the magnetic field at θ can be obtained.

$$H(\theta) = \frac{n(\theta)\, i}{g} H(0) \tag{5.8}$$

The magnetic field $H(\theta)$ depends on the considered starting point$H(0)$ which can be found applying the Gauss' law.

$$\oint_A \vec{B} \cdot d\vec{A} = \int_0^l \int_0^{2\pi} B(\theta)\, r_0 d\theta dz = \mu_0 l r_0 \int_0^{2\pi} H(\theta)\, d\theta = 0 \tag{5.9}$$

Substituting (5.8) in (5.9), the expression for $H(0)$ can be obtained.

$$H(0) = -\frac{i}{g} avg\left[n(\theta)\right] \tag{5.10}$$

Where $avg\left[n(\theta)\right] = \frac{1}{2\pi}\int_0^{2\pi} n(\theta)\, d\theta$ is the mean value of the counting function. So now the winding function can be defined as in (5.11).

$$N(\theta) = n(\theta) - avg\left[n(\theta)\right] \tag{5.11}$$

Thus, the magnetic field can be rewritten using the winding function $N(\theta)$ that has a mean value equal to zero and does not depend on the starting point.

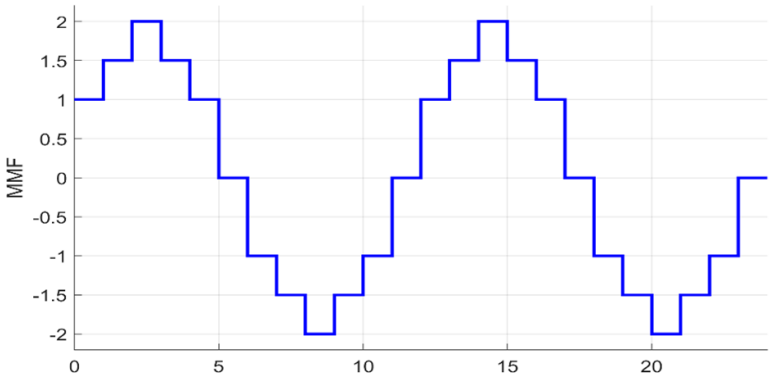

Figure 5.6: Winding function.

$$H(\theta) = \frac{i}{g} N(\theta) \tag{5.12}$$

Once the winding function is defined, it is possible to find the flux along the D-axis, from which the expression of the magnetizing inductance L_{mD} can be written. In the proposed approach, a square wave winding function is considered (as in Figure 5.7).

$$\Lambda_D = i_D \cdot L_{mD} = r L_{stk} \int_{-\pi}^{\pi} B_g \frac{N}{2p} \cos\theta d\theta \tag{5.13}$$

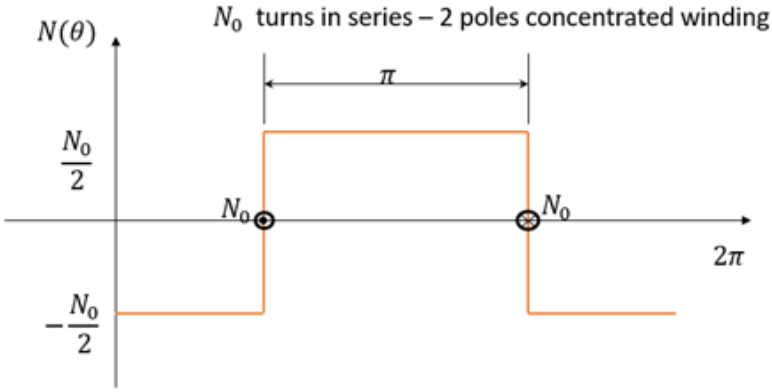

Figure 5.7: Square winding function when p=1.

Where $B_g = i_D \frac{\mu_0 N(\theta)}{2pk_c g}$, so the equation becomes:

$$\Lambda_D = i_D \cdot L_{mD} = \frac{rL_{stk}}{2pk_c g}\mu_0 \left(\frac{N}{2p}\right)^2 i_D \int_{-\pi}^{\pi} \cos\theta^2 d\theta \tag{5.14}$$

Solving the integral and simplifying i_D, the magnetizing inductance on the D-axis can be expressed as follows.

$$L_{mD} = \frac{\pi}{2}\mu_0 \left(\frac{N}{p}\right)^2 \frac{rL_{stk}}{k_c g} \tag{5.15}$$

Where N is the number of turns in series per phase, k_c is Carter's coefficient and r is rotor radius. In order to obtain optimal values of L_{mD}, some guidelines are suggested, such as:

- Small airgap, generally smaller than 1/100 of the pole pitch;
- Appropriate thickness of the rotor back iron, generally bigger or equal than the one of stator back iron.

Otherwise, premature saturation of the rotor occurs, causing unwanted reduction of L_{mD} and increase of the D current component.

5.2.3 Q-axis Magnetic Circuit Model

The magnetizing inductance on the Q-axis is given by the sum of two terms, that are:

- The circulating term c, which includes the field lines circulating in the tips of the rotor flux guides;
- The flow-through term f, which includes the field lines crossing the flux barriers.

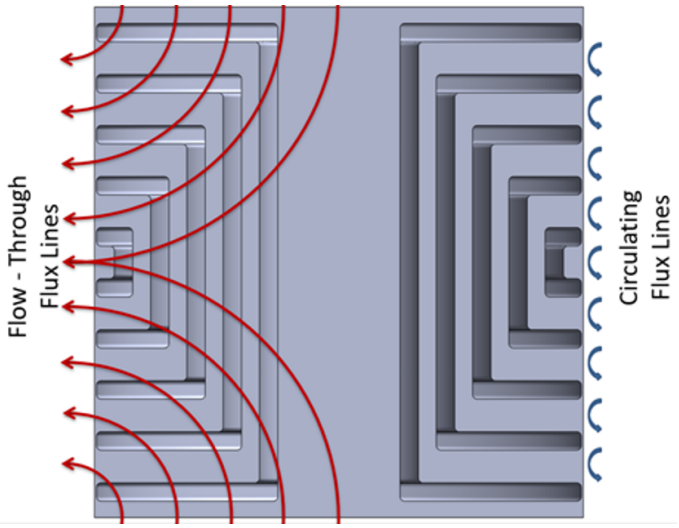

Figure 5.8: Scheme of the circulating term, in blue, and the flow-through term, in red.

$$L_{mQ} = L_{cQ} + L_{fQ} \tag{5.16}$$

These two terms are generated from the distribution of the Q-axis flux, from which the inductances are derived. Every flux barrier has a different magnetic potential, which is constant into the barrier, in fact the circulating flux lines λ_{cQ} are generated from the difference between the magnetic potential in two consecutive flux barriers.

The circulating inductance term L_{cQ} depends on n_{lay}, so from the number of equivalent rotor slots.

A magnetic circuit model is used in [13] and [14] for evaluating the Q-axis flux linkage and, therefore, L_{mQ}. Here, a five flux barriers tubular machine is taken into account, in order to minimize the force ripple generated, according to [15], [16].

Since the magnetic circuit model for a pole pitch is symmetric, only half of the pole pitch will be considered to simplify the model.

The MMF generators represent the Q-axis component of the stator MMF, while the net of permeances stands for barriers (p_b) and airgap flux tubes corresponding to the flux guides ends (p_g). In this simplification, steel is considered as a magnetic short-circuit, so there is no MMF drop. Since a regular rotor pitch is considered, the airgap flux tubes and then the permeances ($p_{g1} = p_{g2} = p_{g3} = p_{g4} = p_{g5} = p_g$) are

all the same. The Q-axis stator MMF, considering one phase only, is a sinusoidal wave of amplitude:

$$\hat{F} = \frac{4}{\pi}F = \frac{4}{\pi}\frac{k_w 2Ni_Q}{4p} = \frac{k_w 2Ni_Q}{\pi p} \tag{5.17}$$

Where $\frac{4}{\pi}$ is the factor needed to pass from a square wave to a sinusoidal one and F is the peak value of the MMF's square wave. It is possible to approximate (5.17), considering a form factor which derives from the distance of the conductor and include the winding factor, simplifying the formula as in (5.18).

$$\hat{F} = \frac{3}{2}\frac{Ni_Q}{\sqrt{3}p} \tag{5.18}$$

All the components in the proposed Q-axis magnetic circuit model are normalized with different bases:

- For the MMF, the base is its amplitude $\hat{F}$;
- For the permeances, the base is $\mu_0 L_{stk}$;
- For the magnetic fluxes, the base is $\mu_0 \hat{F} L_{stk}$.

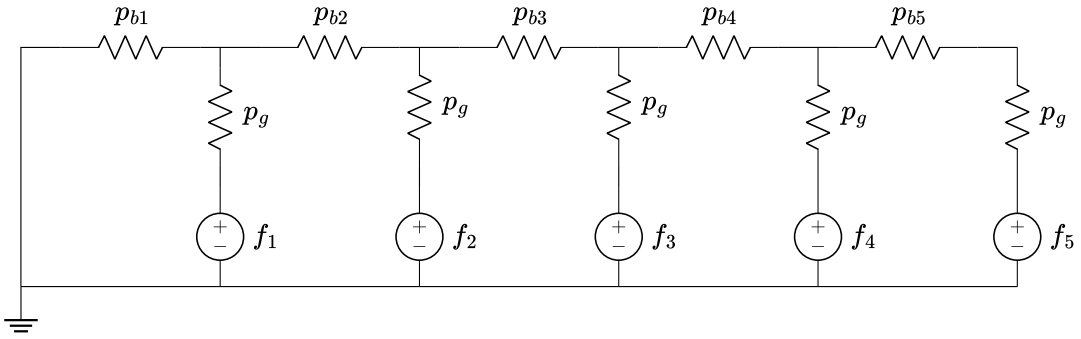

Figure 5.9: Normalized Q-axis magnetic circuit model.

The MMF generators f_1, f_2, f_3, f_4, f_5 are the average values of the sinusoid over the angular span of each rotor flux guide. The more are the layers, the more are the steps of the staircase.

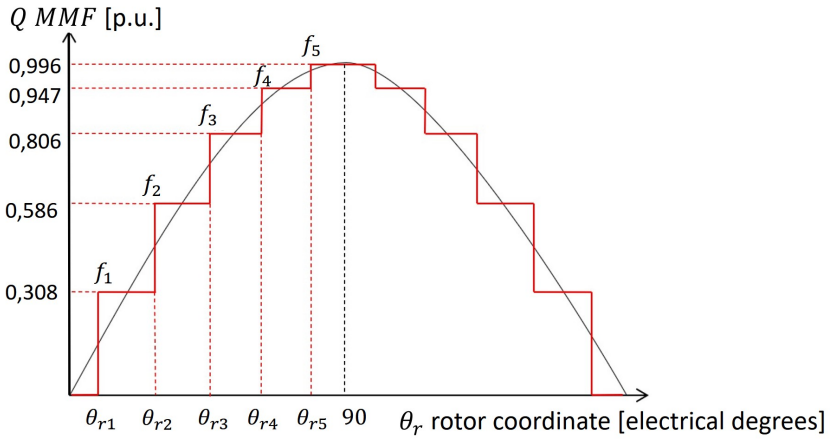

Figure 5.10: Q-axis MMF staircase for the definition of MMF generators.

The values of f_k can be found as follows.

$$f_k = \frac{1}{\Delta\theta_{rk}} \int_{\theta_{rk}}^{\theta_{r(k+1)}} \sin\theta_r d\theta_r = \frac{\cos\theta_{rk} - \cos\theta_{r(k+1)}}{\Delta\theta_{rk}} \tag{5.19}$$

For k=1,2,3,4,5. Where $\Delta\theta_{rk} = \theta_{r(k+1)} - \theta_{rk}$ and represent the electric angle between two consecutive MMF generators. The sinusoidal MMF is split into two components:

- The just defined staircase, which is the one that supplies the flow-through flux;
- The residual MMF, given by the difference between the sinusoid and the staircase, which is the one that generates the circulating component.

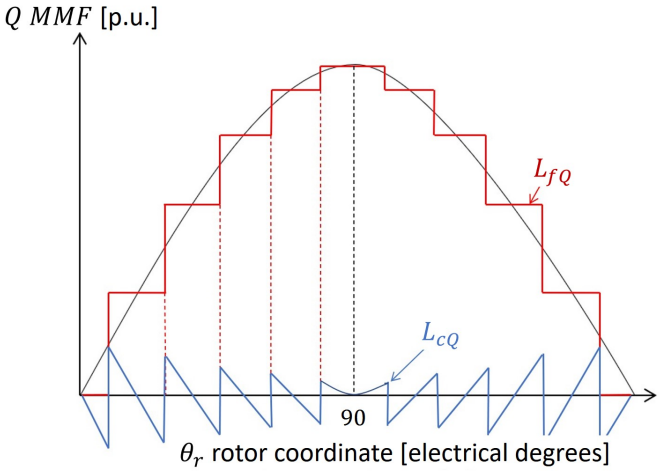

Figure 5.11: Stator MMF and its two components.

Assuming a sinusoidal stator MMF as in Figure 5.11, the circulating term L_{cQ} can be found as follows.

$$L_{cQ} = 4C \sum_{k=1}^{nlay} \int_{\theta_{rk}}^{\theta_{r(k+1)}} \sin\theta_r \left(\sin\left(\theta_r - f_k\right)\right) d\theta_r \tag{5.20}$$

Integrating and substituting the expression of L_{mD} found in (5.15) a simplified form can be obtained.

$$\frac{L_{cQ}}{L_{mD}} = 1 - \frac{4}{\pi} \sum_{k=1}^{nlay} f_k^2 \Delta\theta_{rk} \tag{5.21}$$

The ratio between L_{cQ} and L_{mD} should be as small as possible and it decreases when the number of layers increases.

A rotor with more layers produces a staircase that is more similar to the MMF sinusoidal waveform and it has a reduced MMF harmonic content; in fact, this is reflected by the circulating flux linkage term. Usually, for $n_{lay} > 3$, such inductance component is steadily low and a high saliency value is granted.

To determine the value of the flow-through flux component L_{fQ}, the magnetic circuit model must be resolved. Given the airgap thickness and the flux barrier's dimensions, the permeances' value of the model in per unit can be easily found. Then the magnetic circuit model can be resolved using Kirchhoff's laws and finding the values of the magnetic fluxes and the potentials at the nodes. Considering the two components of stator MMF sinusoid, represented in Figure 5.11, the flow-through inductance component can be found.

$$L_{fQ} = 4C \sum_{k=1}^{nlay} f_k \left(f_k - r_k\right) \Delta\theta_{rk} \tag{5.22}$$

Which can be rewritten in per unit.

$$\frac{L_{fQ}}{L_{mD}} = \frac{4}{\pi} \sum_{k=1}^{nlay} f_k \left(f_k - r_k\right) \Delta\theta_{rk} \tag{5.23}$$

Where r_k is the magnetic potential at node k. It is also possible to write (5.23) in function of the airgap magnetic fluxes, that can be found resolving the magnetic circuit model. In fact, knowing that the airgap magnetic flux can be expressed as:

$$\varphi = \left(f_k - r_k\right) \frac{s_{gk}}{g} \tag{5.24}$$

Where $s_{gk} = \frac{r\Delta\theta_{rk}}{p}$, in which r is mover radius. The expression found in (5.23) can be rewritten as follows.

$$\frac{L_{fQ}}{L_{mD}} = \frac{4}{\pi} p \frac{g}{r} \sum_{k=1}^{nlay} f_k \varphi_k \tag{5.25}$$

It is also possible to pass from airgap magnetic fluxes to barrier magnetic fluxes, applying the simplified hypothesis that the potential drop in the airgap is negligible.

$$\frac{L_{fQ}}{L_{mD}} = \frac{4}{\pi} p \frac{g}{r} \sum_{k=1}^{nlay} p_{bk} \left(\Delta f_k\right)^2 \tag{5.26}$$

So, the torque produced by the motor can be computed using (5.6), which can also be written as:

$$T_{mec} = \frac{3}{2} p k_{dq} \lambda_{md} i_Q \tag{5.27}$$

Where:

- p is the number of pole pairs;
- $k_{dq} = 1 - \frac{L_m Q}{L_m D}$ is the anisotropy factor, or torque coefficient;

- $\lambda_{mD} = L_{mD} i_D$ is the magnetic flux, representative of magnetic loading and airgap surface.

The components that generates the magnetizing inductance on Q axis can be summed according to (5.16), where the two components can be found rearranging (5.21) and (5.23).

$$L_{cQ} = L_{mD} \left(1 - \frac{4}{\pi} \sum_{k=1}^{n_{lay}} f_k^2 \Delta\theta_{rk} \right) \tag{5.28}$$

$$L_{fQ} = L_{mD} \left(\frac{4}{\pi} \sum_{k=1}^{n_{lay}} f_k (f_k - r_k) \Delta\theta_{rk} \right) \tag{5.29}$$

With the purpose of maximizing the torque generated by the motor, torque coefficient k_{dq} should be maximized. This can be pursued by:

- A small airgap, that maximizes L_{mD};
- At least three layers per pole, which minimizes L_{cQ};
- A maximized insulation, provided that the rotor core is compatible with the stator core size, imposed by design parameters.

Considering the power factor of synchronous reluctance machines, maximizing k_{dq} contributes to increase the power factor, so there is nothing better to do from the rotor design standpoint.

$$\cos\varphi \leq \frac{L_D - L_Q}{L_D + L_Q} = \frac{k_{dq}}{1 + \frac{L_{mQ} + 2L_\sigma}{L_{mD}}} \tag{5.30}$$

5.3 Permeances computation for tubular reluctance machine

The previously presented lumped parameter model can be adapted to the different configuration of tubular machines with some corrections. Generally speaking, the permeances value can be computed as follows.

$$P = \mu_0 \frac{A}{l_f} \tag{5.31}$$

Where μ_0 is the permeability of air, A is the area of the section considered, l_f is the length of the flux path. In the lumped parameter model considered, everything is in per unit; in particular, permeances are in per unit of $\mu_0 l_{stk}$. Referring to the flux barrier k, the value of its permeance in per unit can be expressed as follows.

$$p_{bk} = \frac{l_k}{s_{hk}} \tag{5.32}$$

Where l_k is the total length of the flux barrier (considering only half pole pitch) and s_{hk} is the thickness of the flux barrier. Since the machine considered is tubular, the value of l_{stk} corresponds to the perimeter of the circle with radius the distance between the axis of the machine and the considered point, so this value is not constant in every part of the machine. In order to obtain the same model in per unit, a coefficient which considers the reduction of the l_{stk} of the machine should be introduced in permeances' computation. As reference value for $l_{stk,ref}$, the length of the stack at the airgap is considered, because the airgap is where the electromagnetic phenomena occurs.

Figure 5.12 represents the section of the tubular machine:

- The green dashed line represents the 'stack lenght' of the point in which the permeance is computed;
- The red dashed line represents the 'stack length' taken as a reference, which corresponds to the circumference at the airgap and can be computed according

to (5.33).

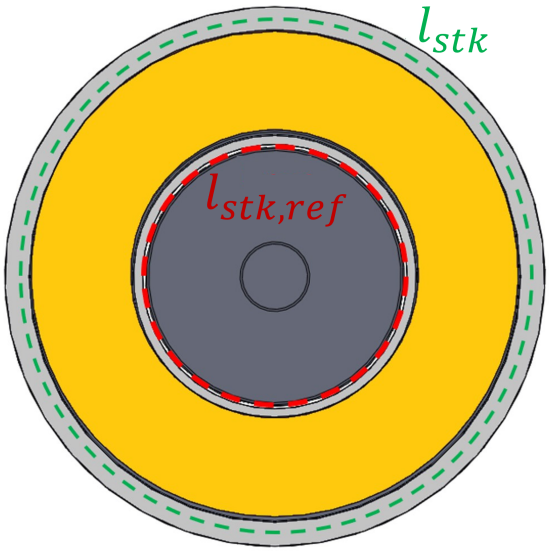

Figure 5.12: Section of the motor to highlight the differences between each circumference value.

$$l_{stk,ref} = 2\pi r_{rot} \tag{5.33}$$

The coefficient δ_k will state the following relationship between the reference value of the length of the stack and the value considered in the specific point in which the permeance should be computed.

$$l_{stk,k} = l_{stk,ref}\delta_k \tag{5.34}$$

So, the computation of the generic permeance in per unit becomes:

$$p_{bk} = \frac{1}{\mu_0 l_{stk,ref}}\mu_0 \frac{A_k}{s_{hk}} = \frac{l_k}{s_{hk}}\delta_k \tag{5.35}$$

Where $A_k = l_k l_{stk,k}$ is the reference area of the flux barrier considered.

5.4 Application to a synchronous tubular reluctance machine

To minimize the force ripple and maximize the thrust force for the chosen configuration, a five mover layers machine is taken into account, in accordance with [16]. Since the plunger geometry will be obtained by means of additive manufacturing, the material considered for the analysis is the alloy FeCo49V2, which is a new metal powder studied for AM applications.

As the computation of each permeances is equivalent, the complete procedure is reported just for the first one, the external one. The figure below highlights the main considered parameters. The required parameters are measured in reference to half pole pitch, as in the magnetic model represented in Figure 5.9. Axial and longitudinal cross sections of the machine are depicted in Figure 5.12 and Figure 5.13 respectively.

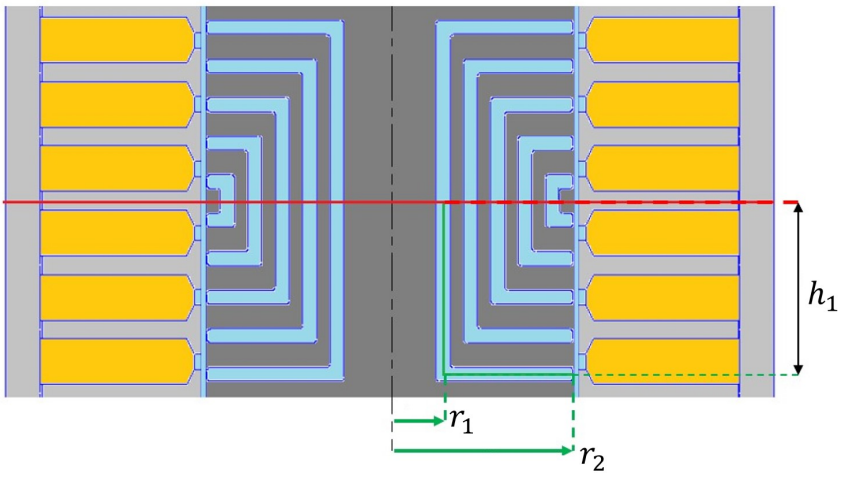

Figure 5.13: Main parameters for permeances computation.

The previously described lumped parameter model has been expanded to include the iron located between the end of each flux barrier and the airgap, the stator tooth, and the second airgap at each stator tooth's end. These elements were added due to mechanical constraints. To accommodate these features, permeances associated with the iron layer were added in parallel to those tied to the flux barriers, while the tooth and gap permeances were placed in series with the airgap ones, as shown in Figure 5.14.

Table 5.1: Machine Dimensions and Parameters.

Parameter Symbol	Machine Parameter	Value	U. M.
l	Length of the machine	200	mm
D_e	External Diameter	50	mm
D_g	Airgap Diameter	24	mm
s_h	Thickness of the flux barriers	0.9	mm
d_h	Thickness of the iron	0.1	mm
Q	Number of Slot	48	-
p	Number of pole	8	-
q	Number of slots per pole per phase	2	-
n_c	Number of conductors	100	-
n_{lay}	Number of flux barriers	5	-

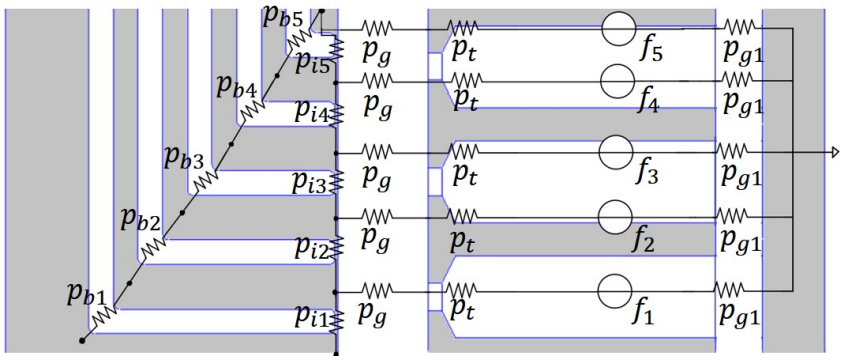

Figure 5.14: Half pole sketch with the new permeances introduced.

The newly proposed lumped parameter model is illustrated in Figure 5.15. The permeance of the flux barrier is divided into two parts: one for the vertical section and another for the horizontal section. For each section, a coefficient is calculated representing the considered barrier's circumference, which is crucial for accurately determining the total permeance.

Initially, end effects were considered but were found not to significantly impact the machine's overall performance. However, including them would greatly complicate the analytical model due to the asymmetry they introduce. Thus, end effects were excluded from the analytical model proposed in this study.

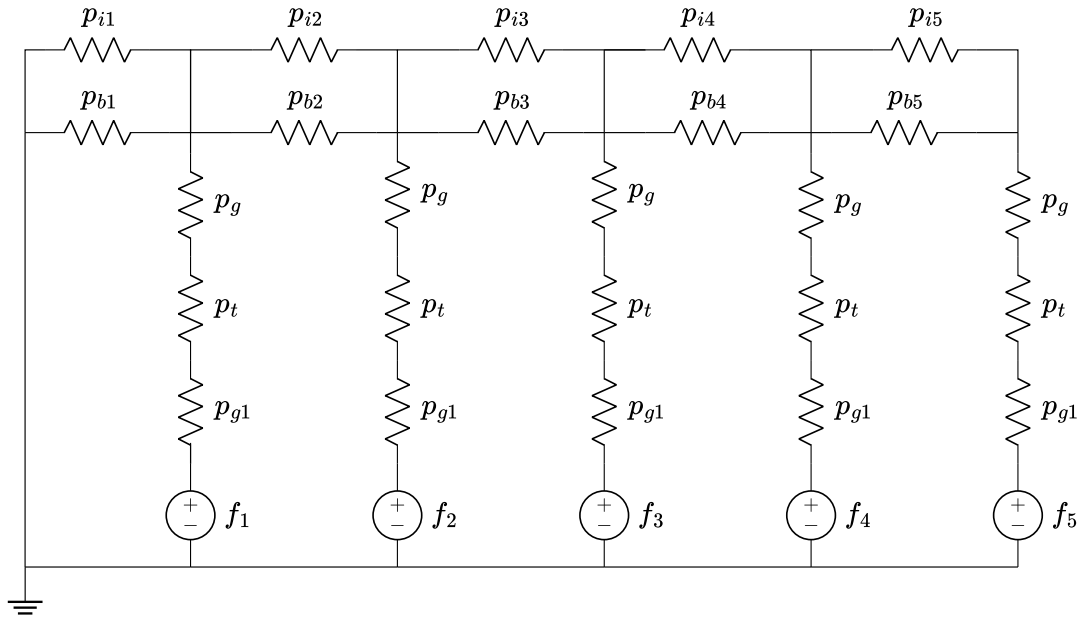

Figure 5.15: Lumped parameter model of the tubular machine.

In order to solve the circuit model, first, the total area of the flux barrier is computed. For simplicity, the middle segment of the mover layer is considered, as shown with green lines in Figure 5.13. Considering the parameters shown in Figure 5.13, the area can be computed as the sum of two surfaces:

- The first one is the external lateral surface of the cylinder obtained from the revolution of the vertical segment along the axisymmetry axis;
- The second one is the surface given by the circular crown with external radius r_2 and internal radius r_1.

$$A_1 = 2\pi r_1 h_1 + \pi(r_2^2 - r_1^2) \tag{5.36}$$

Since the two surfaces are different, it is appropriate to split the computation of the permeance into two components, a vertical one, consisting of a cylidrical shape, and an horizontal one, having a ring shape; each of them will have a different coefficient for the correct computation of the circumferential length, because they have a different radius. Considering, at first, the vertical segment of length h_1, the vertical coefficient is computed as the ratio between the external circumference of radius r_1, which corresponds to the length of the stack at the considered point, and

the length of the stack at the airgap taken as reference.

$$l_{stk,ref} = \pi D_g \tag{5.37}$$

$$\delta_{1,v} = \frac{2\pi r_1}{l_{stk,ref}} \tag{5.38}$$

Now the value of the permeance corresponding to the vertical segment of the flux barrier can be computed considering the coefficient just obtained. The thickness of each flux barrier s_h is equal to 1.1 mm.

$$p_{b1,v} = \frac{h_1}{s_h}\delta_{1,v} \tag{5.39}$$

The same procedure is repeated for the computation of the permeance corresponding to the horizontal segment, for which a new coefficient must be calculated considering the length of the stack at the middle point of the segment.

$$\delta_{1,o} = \frac{2\pi \frac{r_1+r_2}{2}}{l_{stk,ref}} \tag{5.40}$$

Where $\frac{r_1+r_2}{2}$ is the radius at the middle point of the horizontal segment considered. The computation of the desired permeance in per unit can be done, including the corrective coefficient just found.

$$p_{b1,o} = \frac{r_2 - r_1}{s_h}\delta_{1,o} \tag{5.41}$$

The correspondent value of reluctance is found from its definition as the inverse of the total permeance, given by the sum of the vertical and the horizontal component, since they are connected in parallel.

The same methodology is applied to determine all the necessary permeances for accurately solving the magnetic model. Additional permeances (and corresponding reluctances) are calculated relative to the original model, as it did not account for the iron situated between each flux barrier and the air gap. Although this iron section has minimal thickness, it does not reach a saturation level that allows it to be ignored in the proposed model for this machine configuration. Consequently, the permeances of the teeth and the secondary gap between the teeth and the stator yoke are considered. Now, the entire magnetic circuit can be addressed using Kirchhoff's voltage and current laws to determine the magnetic fluxes and potentials at each node, facilitating the calculation of inductance values along the D and Q axes by applying the equations previously mentioned and adapted for tubular electrical machines. The magnetizing inductance along the D-axis can be calculated using (5.15).

This computation allows to obtain a good estimation of the value of L_{mD} when premature saturation of the mover does not occur; on the contrary, an unwanted reduction of L_{mD} is generated and, consequently, an increase of D-current component occurs. Nevertheless, in tubular electrical machines the mover often saturates in some points, because of its geometrical features, since in this case the mover is reduced to a cylindrical plunger. In order to obtain a better estimation of the inductances, a new coefficient should be introduced: the saturation coefficient k_{sat}, which is obtained as the ratio between the sum of the MMF of all the paths in the magnetic circuit and the MMF in the airgap. Each MMF values are computed as the voltage drop in each of the resistors of the lumped parameter model shown in Figure 5.15.

$$k_{sat} = \frac{\Sigma MMF_b + \Sigma MMF_i + \Sigma MMF_g + \Sigma MMF_t + \Sigma MMF_{g1}}{\Sigma MMF_g} \tag{5.42}$$

Thanks to this coefficient, an equivalent magnetic airgap which takes into account saturation phenomena inside the motor can be computed and used to increase the performance of the analytical model. So (5.15) can be rearranged as shown in (5.43).

$$L_{mD} = \frac{\pi}{2}\mu_0 \left(\frac{N}{p}\right)^2 \frac{rl}{k_c k_{sat} g} \tag{5.43}$$

The magnetizing inductance along Q axis can be computed using (5.16). Where the value of the circulating term L_{cQ} can be found applying (5.20) and the flow-through term using (5.22). It is important to highlight that the expression in (**??**) cannot be used in case of tubular machines, since in this case the electric angle spanned by two consecutive flux barriers cannot be used to find the airgap flux considering only the rotor radius, because the machine is linear. In fact, the definition of airgap magnetic flux in the model in per unit, reported in (**??**) for rotative machine, should be modified according to the tubular configuration, by introducing the correct coefficient which takes into account the gradual decrease of the circumference of the section considered and the fact that the iron has a non constant thickness in the magnetic path. According to that, the expression found in (**??**) should be rearranged as shown in the following, by introducing the γ coefficient and considering the correct dimension concerning the tubular configuration.

$$L_{fQ} = L_{mD} \frac{4}{\pi} p \frac{g}{\gamma \frac{l}{2\pi}} \sum_{k=1}^{n_{lay}} f_k \phi_k \tag{5.44}$$

Then L_{cQ} component can be found from the model, according to (5.28). Then, the slot leakage inductance $L_{\sigma,slot}$ and the zigzag inductance $L_{\sigma,zz}$ are computed according to the following equations.

$$L_{\sigma,slot} = q2p\mu_0 l_{stk,ref} n_c^2 k_{slot} \tag{5.45}$$

$$L_{\sigma,zz} = q2p\mu_0 l_{stk,ref} n_c^2 k_w^2 k_{zz} \tag{5.46}$$

Where k_w is the winding fator, k_{slot} is a coefficient which takes into account the

shape of the slot (5.47) and k_{zz} is the zigzag coefficient (5.48).

$$k_{slot} = \frac{h_{so}}{w_{so}} + \frac{h_{wed}}{w_s - w_{so}} \ln \frac{w_s}{w_{so}} + \frac{h_{si}}{w_{se}} \tag{5.47}$$

Where $h_{si} = h_s - h_{wed} - h_{so}$.

$$k_{zz} = \frac{1}{m} \frac{1}{g} \frac{(w_{tr} + w_{ts})^2}{4\,(p_{sr} + p_s)} \tag{5.48}$$

Where p_s and p_{sr} are respectively the slot step and the polar step, w_{ts} and w_{tr} are respectively the iron width at the airgap respectively for the stator and the mover.

So the total inductance value along D and Q axis can be found as follows.

$$L_\sigma = L_{\sigma,slot} + L_{\sigma,zz} \tag{5.49}$$

$$L_D = L_{mD} + L_\sigma \tag{5.50}$$

$$L_Q = L_{mQ} + L_\sigma \tag{5.51}$$

5.5 Materials

The FeCo49V2 alloy was chosen for the prototyping test phase. Magnetic properties of the material were evaluated using full ring samples with a Brockhaus MPG 200 system.

Comprehensive information on the measurements and the experimental setup can be found in [17]. The findings, shown in Figure 5.16, were incorporated into the 2D-FEA software to conduct simulations with the final material. The annealing

process significantly enhances the alloy's magnetic capabilities, achieving saturation similar to conventional FeCo lamination stock. The sample in its initial state has a lower initial slope, indicating reduced initial permeability, whereas the heat-treated sample presents a steeper initial slope, reflecting a marked improvement in initial permeability. The BH curve of the annealed FeCo49V2 sample is employed for the simulations.

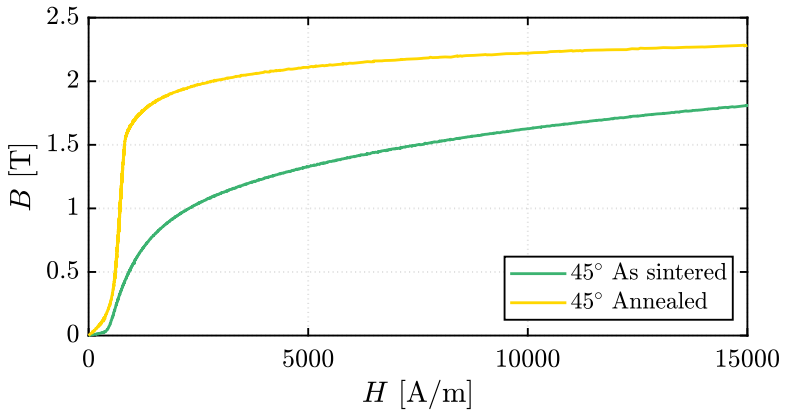

Figure 5.16: BH curve of FeCo49V2 sample: as sintered (green line) and after annealing (yellow line).

5.6 Comparison with simulations' results

In order to verify the accuracy of the proposed model, the obtained results were compared with 2D FEA simulations results from MatlabFEMM toolbox. Simulations were performed by considering a current density of 7.5 $\frac{A}{mm^2}$. The AM material considered for the mover is a metal powder of FeCo49V2, which is a new metal powder studied for AM: it exhibits interesting magnetic properties, but research activity is focused on how to improve its mechanical properties and to reduce internal residual stress which could also affect magnetic properties.

In [18], a comparison of the performance of the machine obtained considering traditional laminated material and AM material is presented, showing a slight decrease in the thrust force with the proposed solution. Nevertheless, the solution with traditionally laminated material is not feasible for this configuration so this slight loss in performance is acceptable. As shown in Figure 5.17, a thrust force of 62.95 N is obtained from the load simulation.

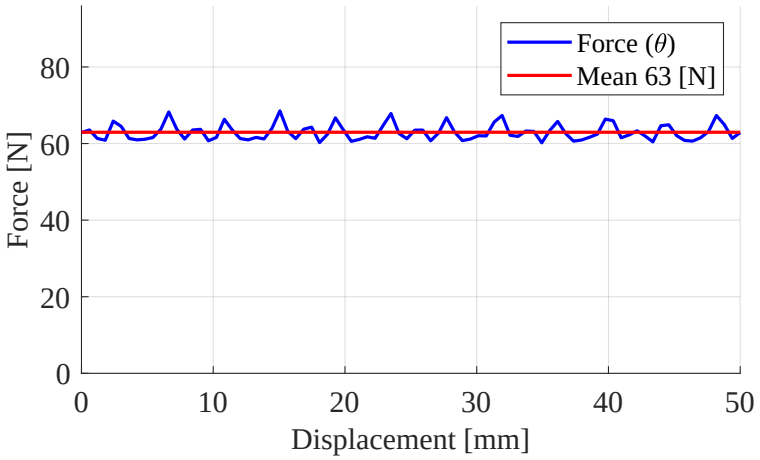

Figure 5.17: Thrust force obtained with 2D FEA simulations.

Figure 5.18 shows the mesh used for the analysis together with the visualization of the flux lines and flux density of the machine obtained in the 2D FEA post processor. Due to the tubular configuration, the mover is brought to saturation more easily than in conventional rotative machines. Hence, saturation is a phenomena which must be taken into account in the analytical design phase.

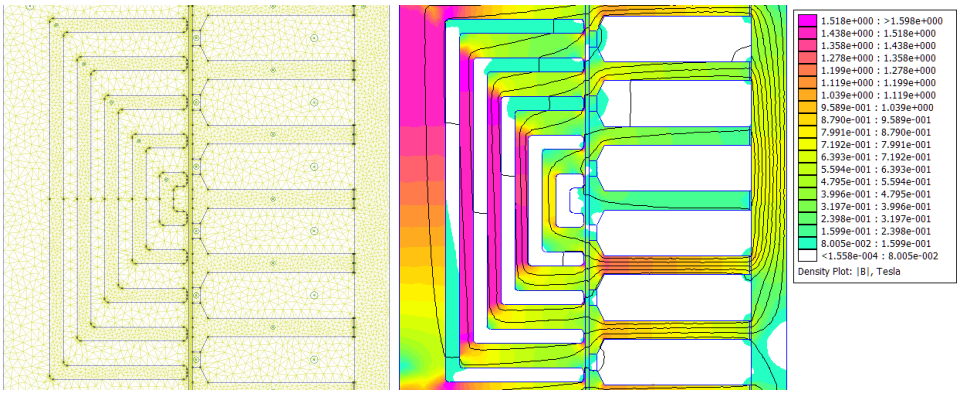

Figure 5.18: 2D FEA mesh (on the left) and post processor (on the right).

Considering the equality between electrical and mechanical power, an analytical expression of the thrust force produced by the tubular machine can be obtained:

$$P_m = P_e \tag{5.52}$$

$$Fv = mEI \tag{5.53}$$

Where v is the linear velocity of the machine, m is the number of phases, E is the electromotive force and I is the total current. Hence, the thrust force can be expressed as follows:

$$F = \frac{3}{2}\frac{\pi}{\tau}\left(L_{mD} - L_{mQ}\right) i_D i_Q \tag{5.54}$$

Where τ is the polar pitch.

The value of the inductance value along D axis decreases with the increase of the current density. However, L_{mD} was first estimated with (5.15), which considers only the potential drop in the airgap and neglects the one in the iron. This is correct only for low values of j because, when the mover saturates, the potential drop in mover iron causes a reduction of L_{mD} and cannot be neglected. This phenomena can be represented by adding the saturation coefficient k_{sat}, according to (5.43). Figure 5.19 shows the trend of the inductances along D and Q axis, comparing the estimation using 2D FEA simulations against the analytical model results.

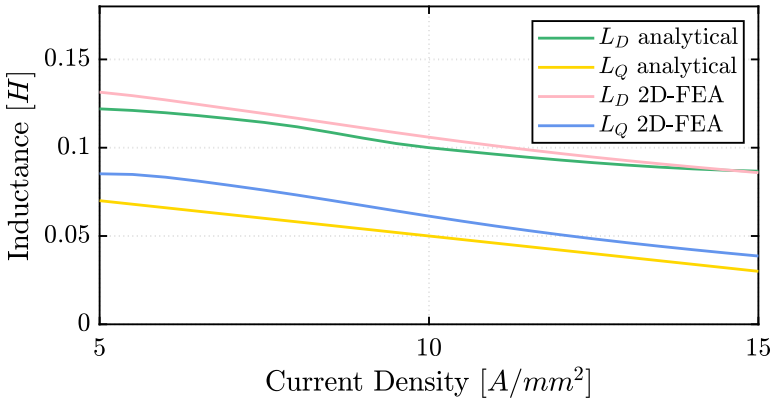

Figure 5.19: Inductances along D and Q axis obtained with 2D FEA simulations and analytical model.

The leakage inductance component is included in both the computed values for L_D

and L_Q. It is important to notice that in the computation of the total leakage inductance reported in (5.49), the belt inductance was neglected. However, with the increasing of saturation level of the machine, this component can become an important factor, causing a different increment in D-axis and Q-axis leakage inductances, as shown in the different FFT of the flux density in the gap computed for D and Q axis (respectively Figure 5.20 and Figure 5.21).

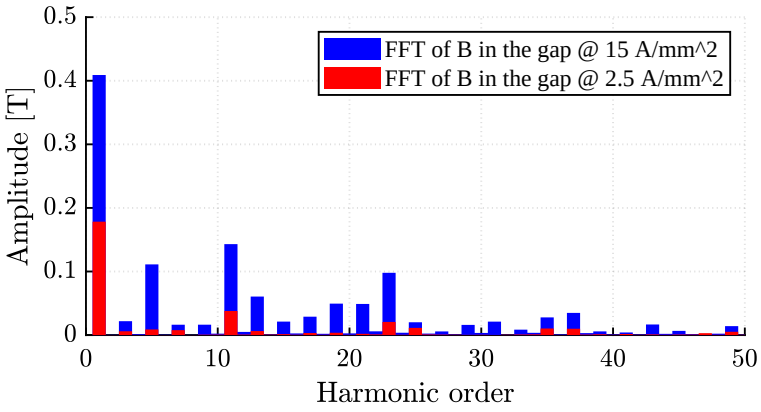

Figure 5.20: FFT of the flux density in the gap comparison at 2.5 and 15A/mm^2 (D axis).

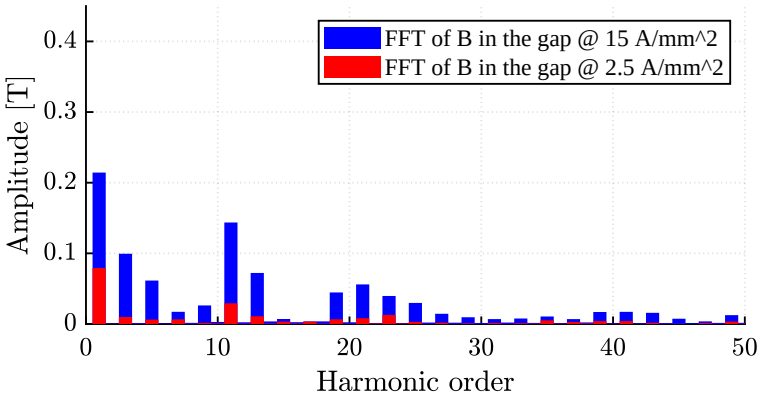

Figure 5.21: FFT of the flux density in the gap comparison at 2.5 and 15A/mm^2 (Q axis).

5.7 Machine Design Optimization

The optimization of a tubular synchronous reluctance motor requires an integrated approach combining analytical modeling and numerical simulation. In the first stage, an analytical investigation is carried out to determine the optimal ratio between the

outer diameter and the air-gap diameter, aiming to maximize the electromagnetic and mechanical performance of the machine. Subsequently, finite element simulations are performed to conduct a detailed parametric analysis, allowing the evaluation of the influence of additional geometric parameters and the global optimization of the motor design.

5.7.1 Optimal Diameters Ratio

Some preliminary analytical considerations help to identify the optimal ratio between the external and air gap diameters of the machine. The force produced by the linear actuator is give by (5.55), where S_g is the air gap surface, B is the magnetic loading and A is the electric load.

$$\mid F \mid \propto S_g B A \tag{5.55}$$

The produced force can be written as function of the external and air gap diameters as in (5.56).

$$\mid F \mid \propto L \pi D_g \left(D_e^2 - D_g^2 \right) \tag{5.56}$$

Defining the air gap to external diameters ratio as in (5.57).

$$\chi = \frac{D_g}{D_e} \tag{5.57}$$

The force expression of (5.56) can be rewritten as follows:

$$\mid F \mid \propto \chi D_e^3 \left(1 - \chi^2 \right) \tag{5.58}$$

The maximum force is achieved by an optimal diameter that is computed by setting to zero the derivative of (5.58) with respect to the diameters ratio χ, as in (5.59).

The optimal value of χ corresponds to 0.58 according to (5.60).

$$\frac{d \mid F \mid}{d\chi} = \left(1 - \chi^2\right) - 2\chi^2 = 0 \tag{5.59}$$

$$\chi = \frac{\sqrt{3}}{3} \simeq 0.58 \tag{5.60}$$

To validate the effectiveness of the proposed analytical approach, a set of 2-D FEA simulations on the reference SynR-TL machine was performed. For a given external diameter, the air gap diameter will affect the slot area. Hence, for a fair comparison, the slot current density was adapted consequently with the aim of keeping the Joule losses at a constant reference value. The current density can be computed considering the expression of the Joule losses of (5.61).

$$P_j \propto RI^2 \tag{5.61}$$

Considering the SynR diameters the phase resistance R and phase current I can be expressed as follows:

$$R = \rho\frac{l}{S} \propto \rho\frac{\left(\frac{D_e - D_g}{2} + D - i\right)}{\left(D_e^2 - D_g^2\right)\frac{\pi}{4}} \tag{5.62}$$

$$I = jk_{fill}S = jk_{fill}\left(D_e^2 - D_g^2\right)\frac{\pi}{4} \tag{5.63}$$

where k_{fill} is the slot filling factor. Substituting (5.62) and (5.63) in (5.61), Joule losses can be expressed as:

$$P_j \propto \rho \frac{\left(\frac{D_e - D_g}{2} + D_i\right)\pi}{\left(D_e^2 - D_g^2\right)\frac{\pi}{4}} \left(j k_{fill} \frac{D_e^2 - D_g^2}{4}\pi\right)^2 \tag{5.64}$$

Introducing the diameter ratio in (5.64), Joule losses can be rewritten as:

$$P_j \propto j^2 D_e^3 \left(1 - \chi^2 + \chi - \chi^3\right) \tag{5.65}$$

For the purpose of keeping constant Joule losses the right-hand side of (5.65) must be set equal to a constant value Ψ, thus Joule losses can be rewritten as in (5.66).

$$\Psi = j^2 D_e^3 \left(1 - \chi^2 + \chi - \chi^3\right) \tag{5.66}$$

Finally, the expression of the current density can be obtained as follows:

$$j = \sqrt{\frac{\Psi}{D_e^3 \left(1 - \chi^2 + \chi - \chi^3\right)}} \tag{5.67}$$

The trend of the current density of the reference SynR-TL machine versus the diameters ratio χ is reported in Figure 5.22.

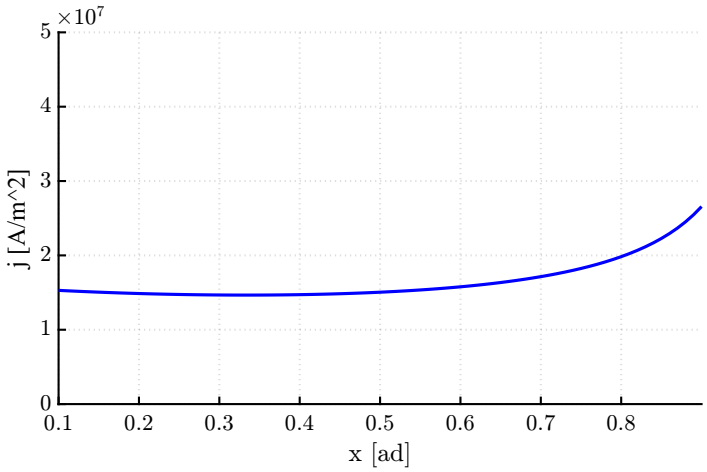

Figure 5.22: Current density as a function of diameter ratio χ.

The per-unit force as a function of the diameter ratio is reported in Figure 5.23.

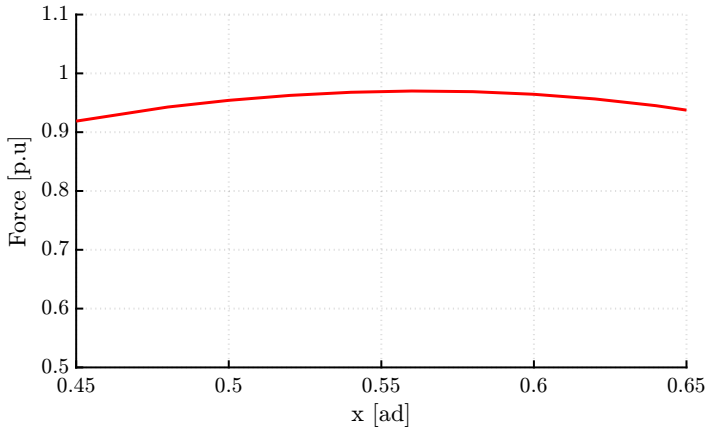

Figure 5.23: Thrust force as a function of diameter ratio χ.

5.7.2 Design Optimization via 2-D Finite Element Analysis

The simulations were carried out on the reference SynR-TL machine, whose parameters are summarized in table 5.1 and the optimization analysis was conducted with regards to plunger's parameters to find the best plunger configuration.

Two types of material were assigned to the rotor: traditional C40 iron steel and metal powder FeSi6.9 for AM. C40 is well-established material for laminated machines, but unsuitable for the proposed SynR-TL motor. FeSi6.9 is a new metal powder studied for AM: it exhibits interesting magnetic properties, but research activity is focused on how to improve its mechanical properties to reduce internal residual stress which could also affects magnetic properties [19].

The first part of 2-D FEA optimization was aimed to validate the optimal diameter ratio of (5.60); for this analysis a 4-layer plunger has been designed. As shown in Figure 5.24, the analytical approach leads to an optimal diameter ratio close to the 2-D FEA one, respectively, 0.58 with analytic approach and 0.54 with the 2-D FEA one.

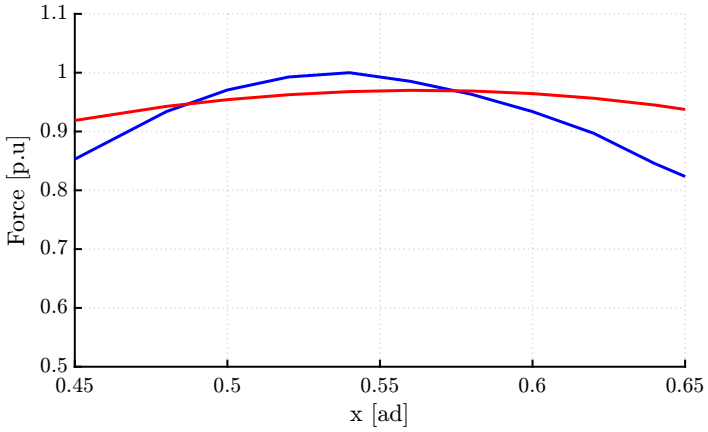

Figure 5.24: Thrust force as a function of diameter ratio χ: red line represents the analytical results and blue line represents simulation results.

Figure 5.25 shows the force ripple (a) and the thrust force (b) of the 4-layer SynR-TL machine as a function of diameters ratio. The SynR-TL machine with AM rotor exhibits a higher force ripple than the SynR-TL one with C40 rotor.

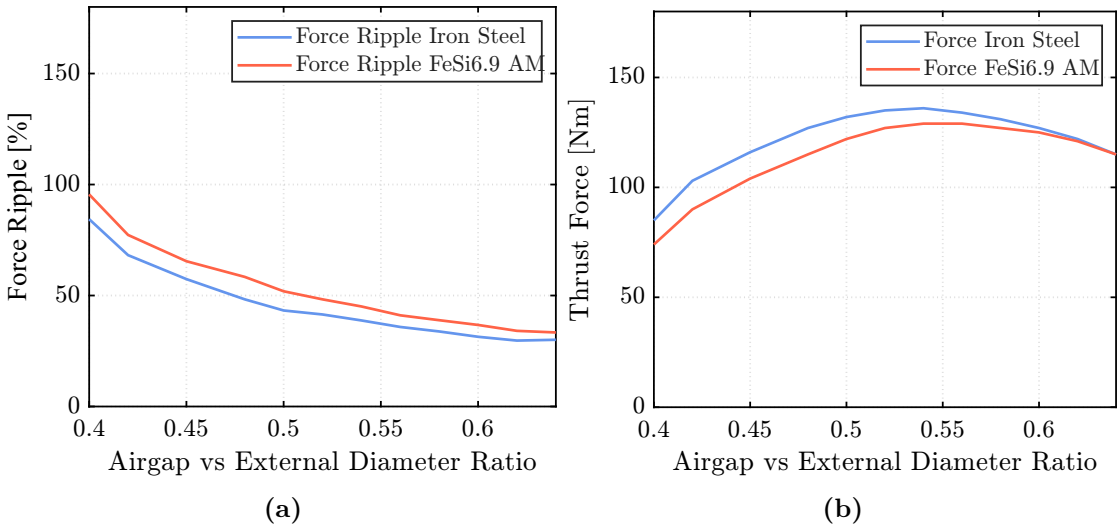

Figure 5.25: Force ripple (a) and thrust force (b) of the 4-layers SynR-TL machine as a function of diameter ratio χ.

The second part of the optimization was aimed at determining the optimal number of plunger layers. As explained earlier, the number of flux barriers per pole affects the L_Q inductance and the plunger spatial harmonics, therefore it has an impact on the average thrust force and the force ripple.

These simulations were carried out assuming the same percentage of plunger air

quantity, where the thickness of flux barrier was set equal to 35% of the pole pitch τ for every configuration of the machine. A peak current density of 15 A/mm^2 was chosen, assuming an intermittent periodic duty.

Figure 5.26 (b) shows the thrust force as a function of the number of plunger layers and as expected the thrust force tends to increase as the number layers increase. According to 2-D FEA, 4-layer and 5-layer SynR-TL machines exhibit similar performance of thrust force and force ripple (see Figure 5.26 (a)). As expected, the 3-layers there SynR-TL machine exhibit a quite high thrust force, but its force ripple is the highest due to the interaction of stator and plunger harmonic orders. The SynR-TL machine with AM rotor has a thrust force of 10% lower than SynR-TL one with C40 iron steel.

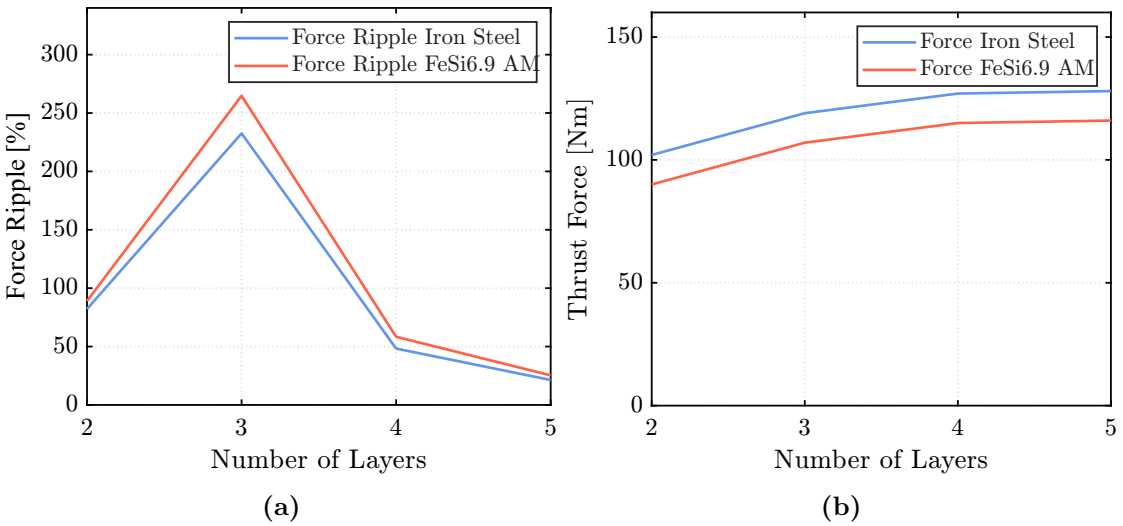

Figure 5.26: Force ripple (a) and thrust force (b) with $j = 15$ (A/mm^2) and different number of layers.

The 4-layer SynR-TL machine was chosen for subsequent evaluations to avoid too low thickness of plunger flux barriers.

Then, the optimization analysis was focused on the choice of the best thickness of the plunger layers and the current density was maintained equal to 15 A/mm^2. Figure 5.27 shows the thrust force as a function of the plunger barrier thickness, expressed in *per unit* with respect to half of the polar pitch ($\frac{\tau}{2}$). According Figure 5.27 (b), the SynR-TL configuration with the maximum force corresponds to a flux barriers thickness equal to the 22 % of the half pole pitch.

Figure 5.27 (a) shows the trend of the force ripple as a function of the plunger barrier thickness.The percentage of the force ripple was computes as the ratio of the peak-to-peak value to the mean one. As shown, the force ripple increases as the plunger air quantity increases due the saturation of plunger iron paths.

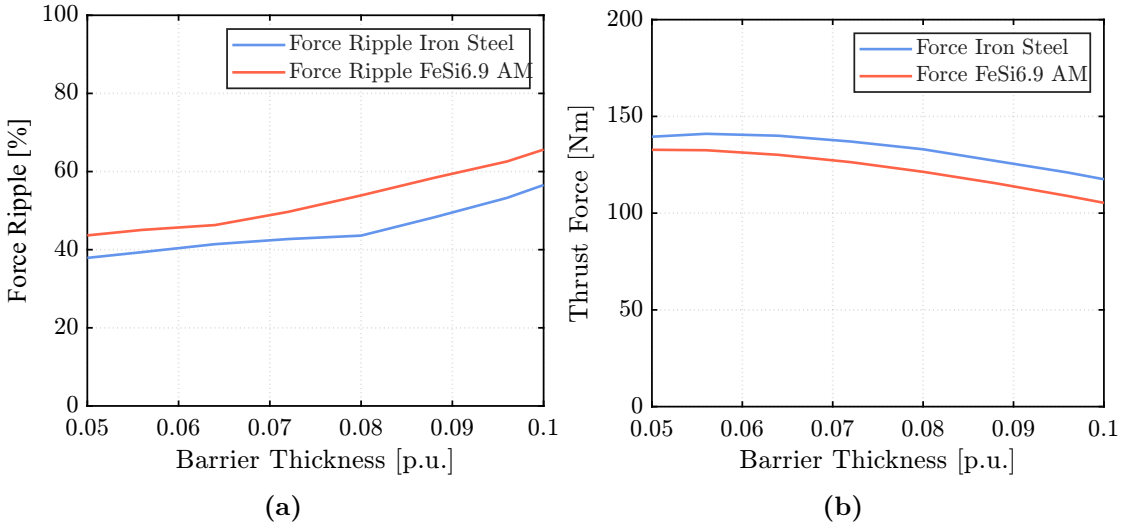

Figure 5.27: Force ripple (a) and thrust force (b) of the 4-layers SynR-TL machine as a function of plunger barrier thickness with $j = 15$ (A/mm^2).

The previous analysis was carried out also with a current density equal to 30 A/mm^2, thrust force and force ripple profiles are reported in Figures 5.28 (a) and (b).

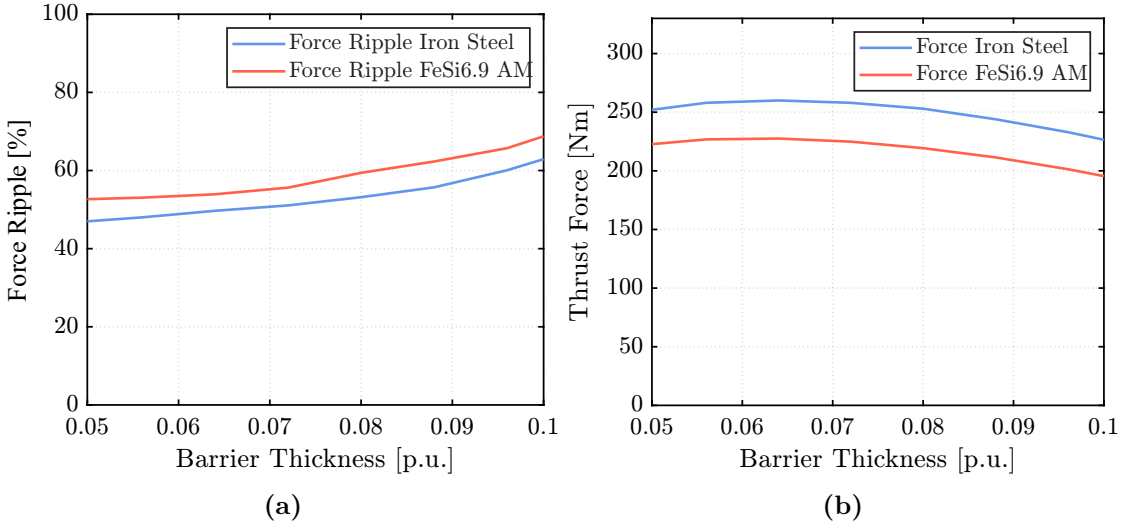

Figure 5.28: Force ripple (a) and thrust force (b) of the 4-layers SynR-TL machine as a function of plunger barrier thickness with $j = 30$ (A/mm^2).

5.8 Metal Additive Manufacturing Feasibility Validation

To assess the feasibility of producing the proposed plunger design, a segment of the mover's pole pitch was fabricated using a 3D printing technique with mild steel powder. The printed model incorporates a 270° cutaway for direct examination and evaluation of the internal layout of the flux barriers. Despite the slim flux barrier thickness of 1.9 mm, the design was manufacturable via Selective Laser Melting (SLM), which yielded well-defined barriers.

SLM is a metal additive process that uses a moving laser beam to melt metal powder layer-by-layer, creating solid cross-sections of the part. This method is prevalently used in fabricating electrical machine components as it produces parts with enhanced density and microstructure in contrast to sintering. The distinct consolidation process results in improved mechanical properties compared to traditional methods for the same material [20].

As depicted in Figure 5.29 (a), an example of a 3D-printed mover pole is illustrated, wherein the rib thickness was increased from 0.1 mm to 0.5 mm. Figure 5.29 (b) showcases the full mover prototype.

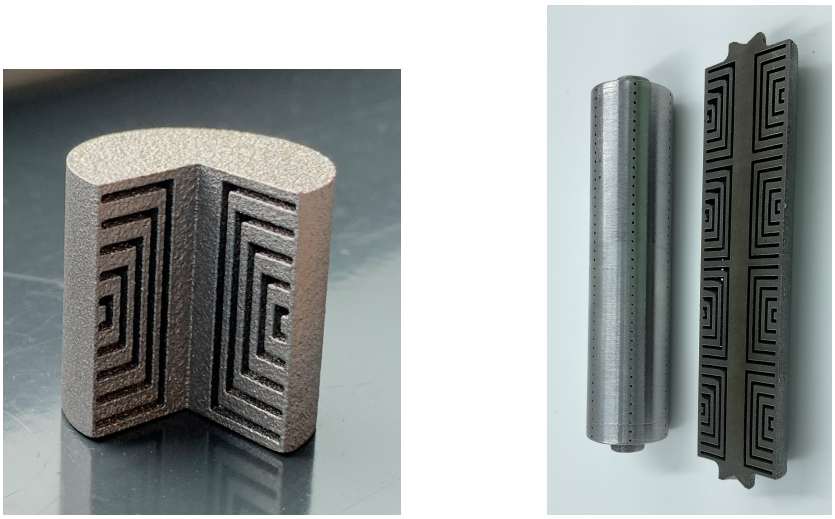

(a) **(b)**

Figure 5.29: Sample of 3D printed mover: one pole in Fe-545 (a) and the complete mover geometry in FeCo49V2 (b).

Two identical prototypes were produced through 3D printing, with one cut along its longitudinal axis to scrutinize the printing quality. A machining allowance of 0.5 mm was factored in. However, challenges in printing the entire geometry can occur if the component isn't angled at 45° during the additively manufactured process, due to perpendicular features to the build direction, necessitating additional support within the flux barriers for the full-length mover.

These supports could be straightforward wall structures or more sophisticated designs, which can help minimizing eddy current losses. To facilitate the full geometry's printing, a manufacturability-oriented redesign was imperative. Drain channels were incorporated at the flux barriers' termini at 120° intervals—totaling six per circlet—and the rib thickness was adjusted from 0.2 mm to 0.7 mm to offer a 0.5 mm allowance for machining. This machining allowance is critical for meeting post-processing needs due to surface and cylindricity demands. The four-pole configuration, importantly, can still be sintered at a 45° angle without needing internal supports.

As highlighted in [20] and [21], printing a non-laminated, solid conducting material for components in electrical machines leads to increased iron losses, due to enhanced generation of eddy currents and hysteresis losses. To minimize these losses in the mover, it is possible to adopt more complex internal structures that introduce gaps within the material. Various design strategies suitable for metal additive manufacturing are available, such as Hilbert structures or mesh-type geometries. Nevertheless, a careful trade-off must be achieved between reducing iron losses and ensuring sufficient mechanical strength of the component to undergo the annealing process with minimal distortion and to allow for machining to final dimensions.

5.9 Experimental Results

A prototype of the motor (see Figures 5.31, 5.32) was built to validate some of the results obtained analytically and through 2D FEA simulations. The stator was constructed using stacked lamination rings housed in a tubular outer shell, and the coil terminals were left unconnected to allow flexible interconnection for testing and parameter measurement.

Initially, the phase winding resistance was measured, yielding a value of 2.69 Ω,

which matches the value obtained through analytical calculations.

The leakage inductance associated with a single stator slot was measured. A value of 811 mH was obtained from 2D FEA simulations (see Figure 5.30 (a)), while experimental measurements on the prototype yielded a value of 813 mH. The analytical results also show good agreement with both the 2D FEA and experimental values.

The mover was manufactured through metal powder bed fusion using FeCo49V2 powder. It was printed with a building direction of 45 degrees. After the printing process, the mover was annealed to improve the magnetic properties of the material.

The complete annealing cycle, descried in [22] and [23], consists of:

- Pre-annealing at 700 $°C$ for two hours;
- Annealing at 820 $°C$ for ten hours.

The two-stage approach optimizes the microstructure for improved magnetic performance and allows to achieve more uniform and larger grain size which is known to be beneficial for reducing hysteresis losses and increasing permeability (further results are reported in [17]).

Additional measurements including the mover were made. As shown in Figure 5.30 (b) the single phase inductance value is slightly lower than the one obtained via 2D FEA simulations, about 0.2 mH less.

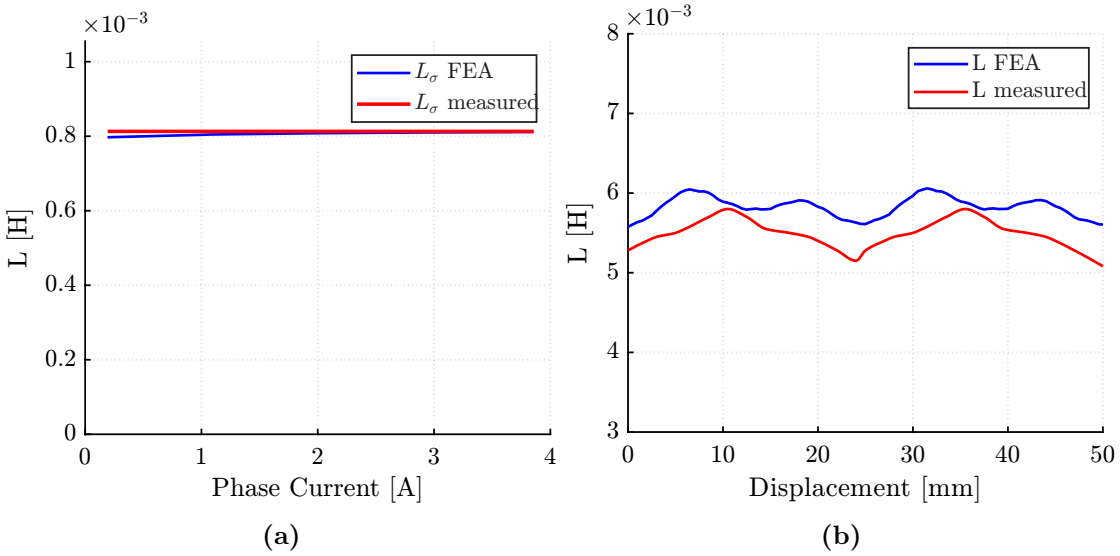

Figure 5.30: 2D FEA and measured L_σ (a) and phase inductance (b).

It is worth noticing that the saliency ratio for the simulated machine and the prototype is nearly the same, equal to 0.89 for the prototype and 0.91 from simulations. In Figure 5.31 the complete 3D geometry of the prototype is shown and a picture of the prototype is reported in Figure 5.32.

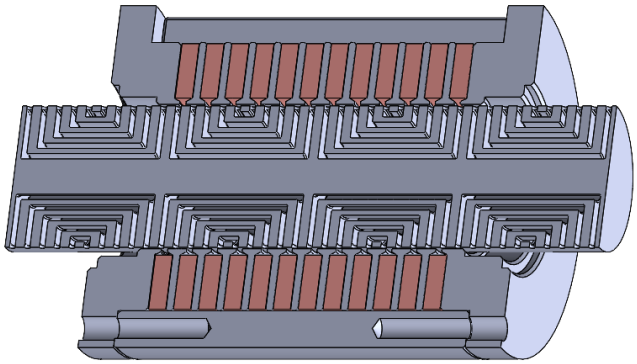

Figure 5.31: Complete CAD 3D rendering of the proposed tubular machine.

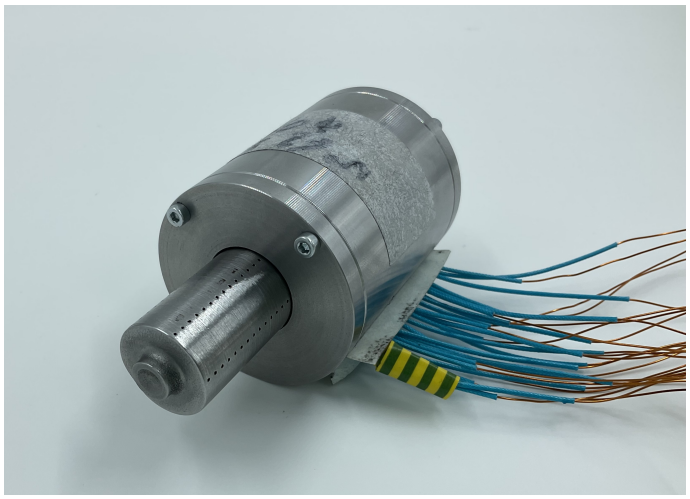

Figure 5.32: Fabricated linear motor prototype.

5.10 Conclusions

A novel configuration of a pure synchronous reluctance tubular linear machine is presented in this chapter. The complex geometry of the rotor part can be manufactured thanks to the metal additive manufacturing.

Furthermore, the lumped-parameter model of a pure synchronous reluctance tubular linear machine was presented. The analytical equations for rotating machines were adapted to linear tubular machines. This model can be used to obtain a first estimation of the expected performance of a machine in terms of thrust force. The results obtained analytically were compared with 2D finite-element simulations' results in order to verify the accuracy of the proposed model. A good correspondence was found between simulations' results and the analytical model over a broad range of current values and especially at low currents, thanks to the introduction of the saturation coefficient in the computation of L_{mD}.

Analytical and simulation analysis were held to define some design guidelines, with a focus on the rotor structure. The proposed analytical approach was validated by the 2-D FEA simulation to define the optimal diameters ratio that produces to the maximum of thrust force; results showed that the optimal ratio ranges between 0.54 and 0.58.

An extensive set of 2-D finite element simulations was performed to optimize the rotor structure. Findings showed that a number of rotor layers equal or greater than four is recommend to reduce the force ripple and that a percentage ratio of the rotor air to the pole pitch close to 22 % is optimal to increase the force density and reduce the force ripple.

In addition, some considerations relating to the re-design process for the manufacturing of the innovative geometry were given, and the first results from a prototype were presented. The measured quantities were in good agreement with the results obtained via 2D FEA and analytical computations when the mover was neglected. The inductance values measured with the mover inserted were slightly lower than the computed ones. Nevertheless, the saliency ratio was nearly the same.

5.11 References

[1] J. Wang, G. Jewell, and D. Howe, «A general framework for the analysis and design of tubular linear permanent magnet machines», *IEEE Transactions on Magnetics*, vol. 35, no. 3, pp. 1986–2000, 1999. DOI: 10.1109/20.764898.

[2] N. Bianchi, S. Bolognani, D. Corte, and F. Tonel, «Tubular linear permanent magnet motors: An overall comparison», *IEEE Transactions on Industry Applications*, vol. 39, no. 2, pp. 466–475, 2003. DOI: 10.1109/TIA.2003.809444.

[3] L. El Amraoui, F. Gillon, S. Vivier, P. Brochet, and M. Benrejeb, «Optimal design approach for linear tubular machines», in *IEEE International Conference on Systems, Man and Cybernetics*, vol. 5, 2002, 6 pp. vol.5-. DOI: 10.1109/ICSMC.2002.1176323.

[4] N. Bianchi, S. Bolognani, and J. Corda, «Tubular linear motors: A comparison of brushless pm and sr motors», in *2002 International Conference on Power Electronics, Machines and Drives (Conf. Publ. No. 487)*, 2002, pp. 626–631. DOI: 10.1049/cp:20020189.

[5] P. A. Commins, J. W. Moscrop, and C. D. Cook, «Synchronous reluctance tubular linear motor for high precision applications», in *2015 Australasian Universities Power Engineering Conference (AUPEC)*, 2015, pp. 1–6. DOI: 10.1109/AUPEC.2015.7324852.

[6] D. Bauer, D. Diamond, J. Li, T. Sandalow D. Paul, and B. Wanner, «U.s. department of energy critical material strategy», in *Tech. Rep. 2010*, 2010.

[7] G. Bailey, N. Mancheri, and K. Van Acker, «Sustainability of permanent rare earth magnet motors in (h)ev industry», in *Journal of Sustainable Metallurgy*, vol. 3, 2017, pp. 611–626. DOI: https://doi.org/10.1007/s40831-017-0118-4.

[8] C. Donaghy-Spargo, «Synchronous reluctance motor technology: Industrial opportunities, challenges and future direction», in *Eng. Technol. Reference*, 2016, pp. 1–15. DOI: 10.1049/etr.2015.0044.

[9] «Directive 2012/27/eu of the european parliament and of the council of 25 october 2012 on energy efficiency, amending directives 2009/125/ec and 2010/30/eu and repealing directives 2004/8/ec and 2006/32», in *Official Journal European Union*, vol. 315, 2012, pp. 1–56.

[10] A. T. de Almeida, F. J. T. E. Ferreira, and G. Baoming, «Beyond induction motors—technology trends to move up efficiency», *IEEE Transactions on Industry Applications*, vol. 50, no. 3, pp. 2103–2114, 2014. DOI: 10.1109/TIA.2013.2288425.

[11] G. Pellegrino, T. Jahns, N. Bianchi, W. Soong, and F. Cupertino, «The rediscovery of synchronous reluctance and ferrite permanent magnet motors», in *SpringerBriefs in Electrical and Computer Engineering*, 2016, pp. VIII, 136. DOI: 10.1007/978-3-319-32202-5.

[12] M. Murataliyev, M. Degano, M. Di Nardo, N. Bianchi, and C. Gerada, «Synchronous reluctance machines: A comprehensive review and technology comparison», *Proceedings of the IEEE*, vol. 110, no. 3, pp. 382–399, 2022. DOI: 10.1109/JPROC.2022.3145662.

[13] A. Vagati, G. Franceschini, I. Maongiu, and G. Troglia, «Design criteria of high performance synchronous reluctance motors», *Conference Record of the 1992 IEEE Industry Applications Society Annual Meeting*, 1992.

[14] A. Vagati, B. Boazzo, P. Guglielmi, and G. Pellegrino, «Ferrite assisted synchronous reluctance machines: A general approach», *2012 XXth International Conference on Electrical Machines*, 2012.

[15] S. Ferrari, G. Pelegrino, M. Davoli, and C. Bianchini, «Reduction of torque ripple in synchronous reluctance machines through flux barrier shift», *2018 XIII International Conference on Electrical Machines (ICEM)*, 2018.

[16] A. Vagati, M. Pastorelli, G. Franceschini, and S. C. Petrache, «Design of low-torque-ripple synchronous reluctance motors», *IEEE TRANSACTIONS ON INDUSTRY APPLICATIONS*, vol. 34, no. 4, 1998.

[17] N. Giannotta, G. Sala, G. Puccio, B. Kallenbach, C. Bianchini, and S. Nuzzo, «Effect of annealing and building direction on the magnetic behavior of additively manufactured feco49v2 alloy», *2025 Workshop on Electrical Machines, Design, Control and Diagnosis (WEMDCD)*, 2025.

[18] C. Bianchini, G. Sala, A. Torreggiani, *et al.*, «Synchronous reluctance tubular machine by means of additive manufacturing», in *2022 International Conference on Electrical Machines (ICEM)*, doi:10.1109/ICEM51905.2022.9910808, 2022, pp. 921–927.

[19] M. Garibaldi, I. Ashcroft, N. Hillier, S. Harmon, and R. Hague, «Relationship between laser energy input, microstructures and magnetic properties of selective laser melted fe-6.9%wt si soft magnets», *Materials Characterization*, vol. 143, Sep. 2018. DOI: 10.1016/\allowbreakj.matchar.2018.01.016.

[20] N. Giannotta, G. Sala, C. Bianchini, and A. Torreggiani, «A review of additive manufacturing of soft magnetic materials in electrical machines», *Machines*, vol. 11, no. 7, 2023, ISSN: 2075-1702. DOI: 10.3390/machines11070702. [Online]. Available: https://www.mdpi.com/2075-1702/11/7/702.

[21] A. Plotkowski, J. Pries, F. List, *et al.*, «Influence of scan pattern and geometry on the microstructure and soft-magnetic performance of additively manufactured fe-si», *Additive Manufacturing*, vol. 29, p. 100 781, 2019, ISSN: 2214-8604. DOI: https://doi.org/10.1016/j.addma.2019.100781. [Online]. Available: https://www.sciencedirect.com/science/article/pii/S2214860419304051.

[22] T. Lindroos, T. Riipinen, S. Metsä-Kortelainen, J. Pippuri-Mäkeläinen, and A. Manninen, «Lessons learnt-additive manufacturing of iron cobalt based soft magnetic materials», *Journal of Magnetism and Magnetic Materials*, vol. 563, p. 169 977, 2022.

[23] T. Riipinen, S. Metsä-Kortelainen, T. Lindroos, J. Keränen, A. Manninen, and J. Pippuri-Mäkeläinen, «Properties of soft magnetic fe-co-v alloy produced by laser powder bed fusion», *Rapid Prototyping Journal*, vol. 25, no. 4, pp. 699–707, 2019.

6. Innovative Rotor Winding Geometry for Synchronous Machine By Means of Additive Manufacturing

Wound-Field Synchronous Motors (WFSMs) represent a versatile and robust class of synchronous machines in which the rotor magnetic field is generated by an excitation winding rather than by permanent magnets. This configuration offers significant advantages, including controllable field strength, wide speed range, and the absence of rare-earth materials. However, the efficiency and performance of these machines are strongly influenced by the design and manufacturing of the rotor winding, which must balance electrical conductivity, thermal management, and mechanical integrity within a limited space.

Traditional manufacturing techniques impose geometric constraints on the winding layout, limiting the achievable slot fill factor. A low fill factor results in higher copper losses and reduced efficiency. To overcome these limitations, Additive Manufacturing (AM) offers a promising alternative. By enabling the direct fabrication of complex winding geometries, AM makes it possible to significantly increase the fill factor, optimize current distribution, and improve overall performance.

In the first part of this study, a rotor winding made of copper is considered, serving as a reference configuration due to its high electrical conductivity and established industrial use. In the second part, the same approach is extended to aluminum, whose lower conductivity is compensated by the enhanced slot utilization achieved through additive manufacturing. The maximization of the fill factor allows the aluminum winding to reach performance levels comparable to those of the copper design, while offering potential benefits in terms of weight reduction, cost, and sustainability.

This chapter therefore investigates the chance of applying additive manufacturing to rotor windings in wound-field synchronous machines, highlighting how this technology enables new design freedoms and efficiency improvements unattainable with

conventional production methods. In this context, only analytical analysis and simulations results relating to the innovative rotor winding configuration are reported and at this stage the printing process is not analyzed.

The chapter is organized as follows: Section 6.2 presents the main characteristics of the reference traditional motor considered for the comparison, Section 6.3 introduces the innovative winding geometry, Section 6.4 reports some analytical considerations, in Section 6.5 and Section 6.6 the magnetic and mechanical simulations' results are discussed.

6.1 General Overview

AM could be applied both for soft magnetic materials [1], [2] or copper [3], [4] and aluminum [5] for coils; in both cases it allows to obtain innovative and optimized geometries which can improve the machine performance and minimize the waste of material produced during the manufacturing process.

Many AM research related to electrical machines' try to improve the stator windings, as a substitution of copper wires and hairpin. In particular hairpin are getting popular in automotive applications, because they grant an higher filling factor and allow to reduce the AC losses respect to random wound windings. AM gives the possibility to further improve the hairpin design optimizing the shape of the winding, with innovative solutions that were not feasible with more traditional manufacturing techniques (for example variable hairpin cross section).

Authors in [6] shows an additive manufactured coil whose end windings are redesigned with the purpose of improving the heat transfer coefficients, so optimizing the cooling of these components. At the end, a significant reduction (about 30%) of the steady state temperature was measured.

Nevertheless, the insulation of additive manufactured windings is more complex and require an higher thickness of the insulating system. In addition, they are more sensitive to deterioration phenomena of the insulation related to the stress introduced by the PWM on the stator windings due to the insulation obtained typically with potting techiniques. In [7] the fabrication of an insulation coatings on an electrical windings made in CuCrZr is deepened considering three processing

techniques.

Furthermore, to obtain an higher fill factor in [8] authors proposes a geometry with variable cross-sectional area, which lead to an increment of the sensitivity of the winding losses to frequency variations.

Electrically excited synchronous motors (EESMs) are widely used in industrial applications, such as large pumps, generators and, more recently, also in automotive industry, due to their performance and high efficiency [9], [10], [11]. Nevertheless, to achieve the desired performance an optimal design and pole shaping of the rotor becomes crucial. In [12] an optimal pole shaping method is found analytically with the purpose of optimizing the MMF waveform at the airgap. Optimal shaping for electrically excited synchronous motors is an important aspect of motor design that has a significant impact on its performance and efficiency.

Furthermore, authors in [13] proposed a fluid dynamic-based pole shaping; combining fluid dynamics and electromagnetic considerations in the rotor design an improvement of the overall performance of the machine is obtained.

In [14], [15] and [16] hybrid excited PM synchronous motors are analyzed: thanks to the presence of both magnets and windings the flux on the rotor can be adjusted to achieve an higher maximum feasible speed in flux weakening condition. In [17] the control strategy of this configuration is deepened: a new FW control scheme suitable for anisotropic HEPM motors with high motor inductances is presented. A hybrid FW architecture is developed, including a feed-forward generation of the excitation current reference and a voltage loop for the direct-axis current reference. On one hand, the feed-forward excitation current reference generation aims to maximize the output power. On the other hand, the voltage loop for the direct axis current is inspired by conventional IPM sensorless schemes [18].

For these reasons, a design of a rotor winding for a synchronous machine is presented. With the purpose of maximizing the slot filling factor of rotor slots, the new rotor coil is completely re-designed and it must be produced employing AM. In this case DC voltages are used and lower values are involved compared to the ones relating to the ones generally used in stator windings, so from the insulation point of view the application is less critical.

6.2 Reference Machine

The reference machine considered for this work is shown in Figure 6.1 and its main data are reported in Table 6.2.

The classic geometry is a 36 slot-6 pole electrically excited salient pole machine, where the external pole shape was already optimized according to [12]. Optimal shaping for electrically excited synchronous motors is an important aspect of motor design that can have a significant impact on its performance and efficiency. Authors in [12] present a preliminary analytical method which provides a fast and effective way to design high-performance motors that meet the demands of modern industrial applications.

Considering traditional manufacturing techniques, generally rotor windings are characterized by a low filling factor, so the maximum copper surface is limited by the productive process. Incrementing the filling factor could lead to a reduction of rotor winding resistance and overall better performance of the machine.

Table 6.1: Reference Machine Parameters

Machine Parameter	Parameter Symbol	Value	U. M.
Pole pairs	p	3	-
Slots number	Q_s	36	-
External stator diameter	D_e	184	mm
Internal stator diameter	D_i	126	mm
Airgap	g	0.8	mm
Axial length	L_{stk}	80	mm
Slot area	S_{slot}	66.8	mm^2
Stator nominal current	I_{nom}	26	A_{rms}
Rotor ampère turn	$N_e I_e$	540	As
Mechanical base speed	ω_e	4500	As

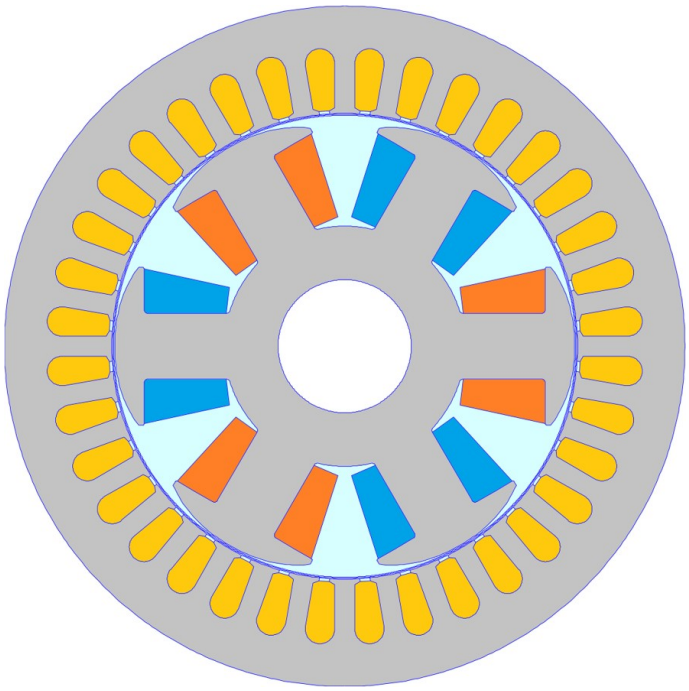

Figure 6.1: Reference machine.

6.3 AM Rotor Winding Geometry

Rotor windings are way more difficult to produce with traditional manufacturing techniques and, generally, a low filling factor is obtained. So, a complete re-design of the coil geometry was made. The proposed geometry, shown in Figure 6.2a, was designed considering 8 conductors with equal cross section area but different shapes with the purpose of maximizing the filling factor.

In Table 6.2 the main parameters of the rotor winding for the reference motor and the proposed one are presented and compared.

Table 6.2: Reference Machine Parameters

Machine Parameter	Reference Motor	Proposed Motor
Number of conductors	8	8
Filling factor	0.5	0.97
Conductor section	13.5 mm^2	33.5 mm^2
Current density	5 A/mm^2	1.96 A/mm^2

In Figure 6.2b an optimization of the pole shape is proposed, with the purpose of

reducing the mechanical stress, according to [13]. To exploit all the available area, the coil geometry is adapted to the optimized pole shape. It is evident, how the proposed geometry perfectly fits with the pole shape, while with more traditional manufacturing techniques a lower filling factor should have been used.

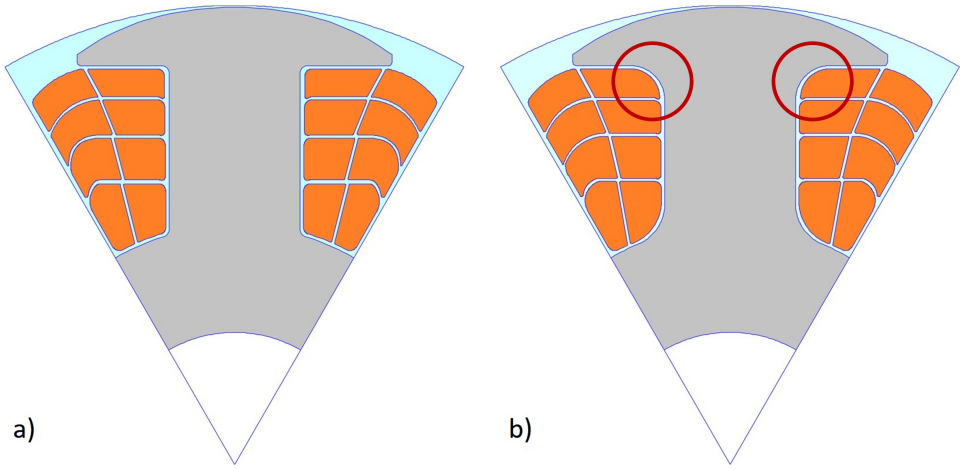

Figure 6.2: One pole sketch with the new coil geometry (a) and with the new pole shape (b).

The coil geometry was realized as a result of an optimization process, whose main purposes are:

- the maximization of the copper area between each pole, in order to exploit all the empty spaces and follow the pole shape geometry;
- keeping constant the cross section area of each conductor, so that the current density is the same in every conductors and there are not problem with the insulation of some conductors;
- finding a good balance of the overall rotor inertia.

Figure 6.3 shows the complete motor design with the innovative coil and the re-design of the poles. In the next sections the performance of the two machines will be compared through a magnetic analysis and a mechanical analysis.

6.4 Analytical Analysis

Figure 6.4 shows the per unit flux as a function of the rotor excitation. The per unit values are based on the nominal operating condition of the machine.

The proposed geometry is evaluated analytically with both copper and aluminium

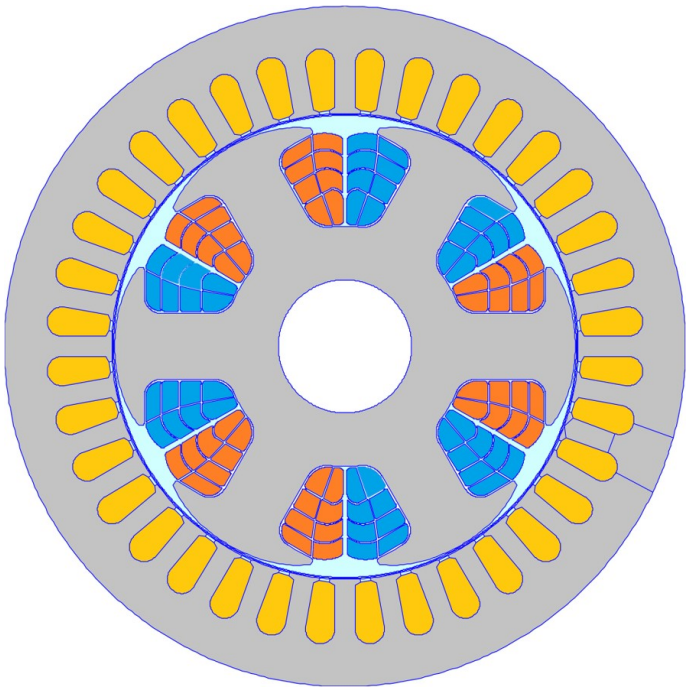

Figure 6.3: Innovative geometry proposed.

windings and at the same rotor Joule losses value of the traditional machine. The rotor Joule losses can be expressed as

$$P_{J,rot} = \rho_{Cu} S_{Cu} L_{stk} j_e^2; \tag{6.1}$$

Where ρ_{Cu} is the resistivity of the copper, S_{Cu} is the total copper cross section area, L_{stk} is the stack length and j_e is the rotor slot current density. Considering that:

- The copper resistivity of a printed winding has an increment of about 10 %;
- The total copper cross section is incremented by 2.5;
- The lenght of the stack is the same.

The following relations between the reference motor and the proposed one can be defined.

$$\rho_{Cu,AM} = 1.1 \rho_{Cu}; \tag{6.2}$$

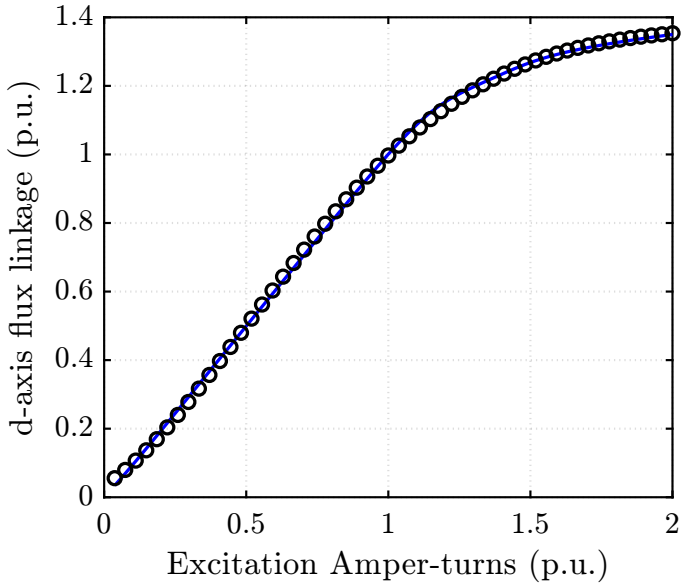

Figure 6.4: Per unit flux as a function of the rotor excitation.

$$S_{Cu,AM} = 2.5 S_{Cu}; \tag{6.3}$$

The corespondent current density which must be applied to obtain the same rotor Joule losses can be found equaling the two rotor Joule losses.

$$\rho_{Cu} S_{Cu} L_{stk} j_e^2 = \rho_{Cu,AM} S_{Cu,AM} L_{stk} j_{e,AM}^2; \tag{6.4}$$

Then

$$j_{e,AM} = j_e \sqrt{\frac{1}{1.1} \frac{S_{Cu}}{S_{Cu,AM}}} = 0.6 j_e = 3 \frac{A}{mm^2}; \tag{6.5}$$

Referring to the per unit flux linkage trend reported in Figure 6.4, the increment of the flux linkage is 25 %, which is directly related to the torque increment.

The same procedure was implemented considering an aluminum rotor winding, in which the resistivity of the winding material of the additively manufactured machine must be re-adaped according to aluminum properties.

$$j_{e,AM,Al} = j_e \sqrt{\frac{1}{1.71} \frac{S_{Cu}}{S_{Cu,AM}}} = 0.48 j_e = 2.42 \frac{A}{mm^2}; \tag{6.6}$$

In this case, always referring to Figure 6.4, the increment of the flux linkage is 16 %. This result can be compared with the one obtained with 2-D FEA simulations reported in Section 6.5.

6.5 Magnetic Analysis

The magnetic analysis was performed via 2D Finite Element Analysis (FEA). In Figure 6.5 and Figure 6.6 the 2D FEA post processor is reported for, respectively, the traditional topology and the innovative proposed winding and pole shape.

In Subsection 6.5.1, the two geometries were analyzed considering the same working condition, reported in Table 6.2. Otherwise, in Subsection 6.5.2 the two configurations are compared considering the same rotor Joule losses. Simulations were performed considering for the new geometry a filling factor of the rotor windings of 0.97 to take into account the thickness of the insulation.

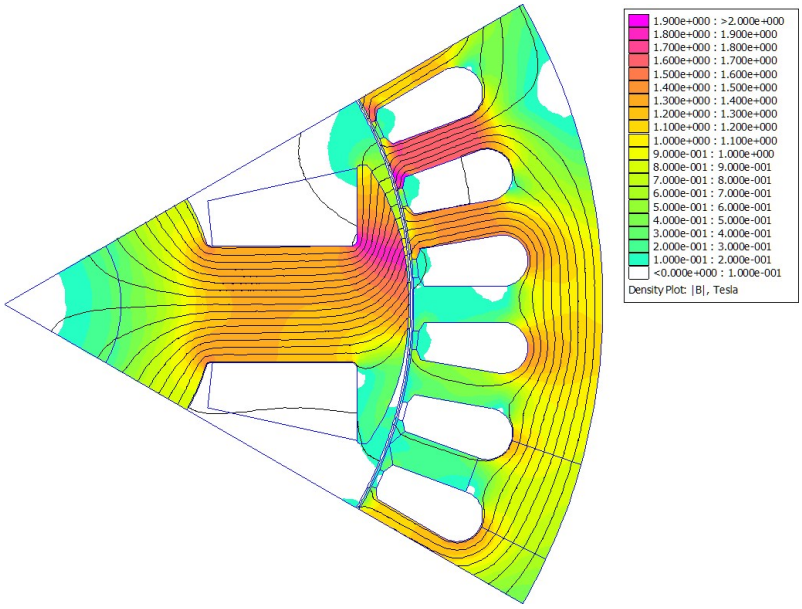

Figure 6.5: 2D FEA post processor for the traditional configuration.

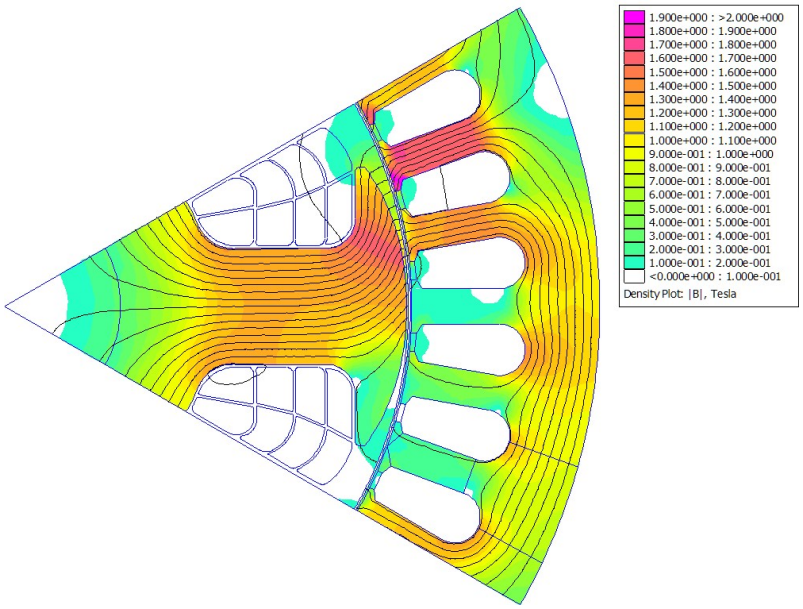

Figure 6.6: 2D FEA post processor for the proposed innovative coil geometry.

6.5.1 Constant torque comparison

From the flux density values found at load conditions (Figure 6.5 and Figure 6.6) a benefit related to the more fluid pole shape can be appreciated in the reduction of the maximum flux density value in the pole. With the traditional configuration a maximum value of 1.8 T is found, on the other side with the optimized pole shape the maximum inductance is reduced to 1.6 T.

Since the proposed geometry is characterized by lower rotor winding resistance, the reduction of the Joule losses generated in the rotor can be appreciated. So, a comparison between aluminum and copper windings is made: aluminum is becoming increasingly studied for electrical machine windings because it is less expensive and lighter than copper. Nevertheless, its electrical conductivity is lower, so its resistivity is higher, leading to an increment in the winding resistance and, consequently, the Joule losses.

Thus, with the proposed rotor coil geometry, the overall losses can be reduced even with aluminum, obtaining better performance with fewer costs and total weight.

Furthermore, thanks to the potentiality of AM, a re-design of the end windings could be made to improve the heat flow thermal coefficient by incrementing the total dissipating surface. Hence, the innovative geometry allows minor rotor-joule

losses to be obtained with a better thermal dissipation.

Neglecting the end windings re-design, the joule losses reduction obtained with the proposed aluminum winding is reduced of the 37 % compared with the traditional solution. Otherwise, if the proposed geometry is realized using copper, a 60 % rotor Joule losses reduction can be appreciated. Obviously this leads to great advantages in terms of overall efficiency of the machine.

These results do not consider the increment of copper resistivity related to the lower density of the printed material. However, according to [3], this increase is less than 10 %, so the results continue to be optimal for the innovative geometry proposed.

6.5.2 Constant rotor Joule losses comparison

Then a comparison is proposed considering the same Joule losses of the rotor between the traditional geometry and the innovative one with aluminum rotor windings. Figure 6.7 shows the 2D FEA post-processor of the proposed machine with the same Joule losses of the traditional configuration. It is interesting to notice how, due to the fluid design of the pole shape, the maximum induction value in the pole is still lower than in the traditional configuration (1.7 T).

In this case, an increase of the 10 % of the aluminum resistivity was considered in order to include the effect of the lower density of the printed material.

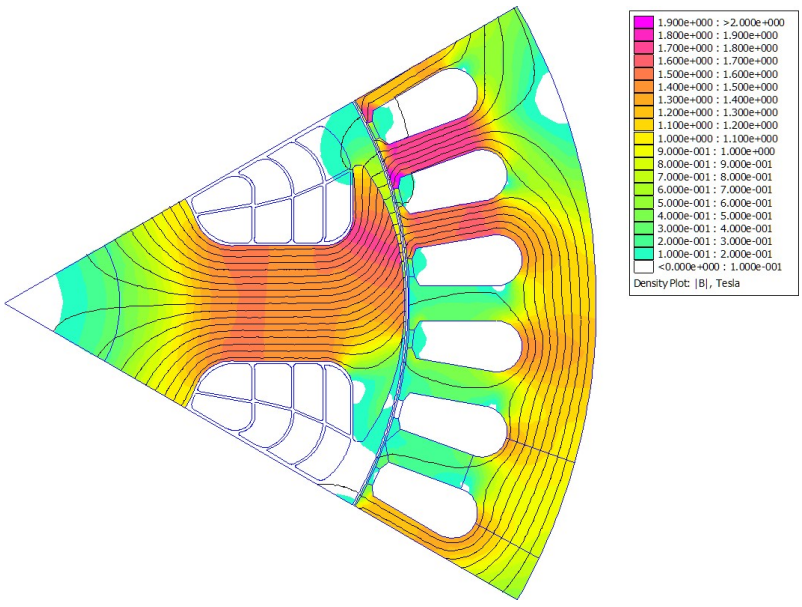

Figure 6.7: 2D FEA post processor for the proposed innovative coil geometry with the same rotor Joule losses.

In Figure 6.8 a torque comparison between the traditional and the proposed machine is shown. The torque increment from 25 Nm to 29.6 Nm, so an improvement of the 18 % can be appreciated.

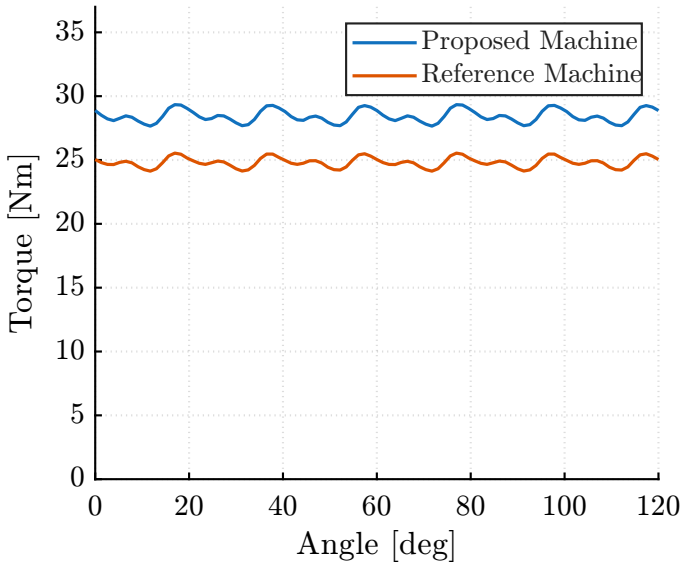

Figure 6.8: Torque comparison between the traditional and the proposed machine with the same Joule losses.

6.6 Mechanical Analysis

Another important aspect that must be considered is the mechanical resistance of the rotor. This analysis was performed with 3D FEA. Generally the most critical points are:

- the connection between the pole body and the rotor;
- the connection between the pole body and the airgap pole shoe.

In these points the maximum stress reached can be dangerous, especially when high speeds are involved. In the case of AM rotor it is possible to adopt a more smooth transition between the inner part of the rotor and the teeth to reduce the stress in this section.

Incrementing the fitting radius in those points leads to a more fluid geometry with reduced over stress in critical points.

In Figure 6.9, Figure 6.10 and Figure 6.11 the results of the mechanical simulations are shown. The simulations were performed considering the centrifugal force

generated with a maximum speed of 4500 rpm.

The simulation are referred to the base speed of the motor with the aim to compare the stress with the different rotor winding configurations, obviously an higher speed can be reached in the constant power region.

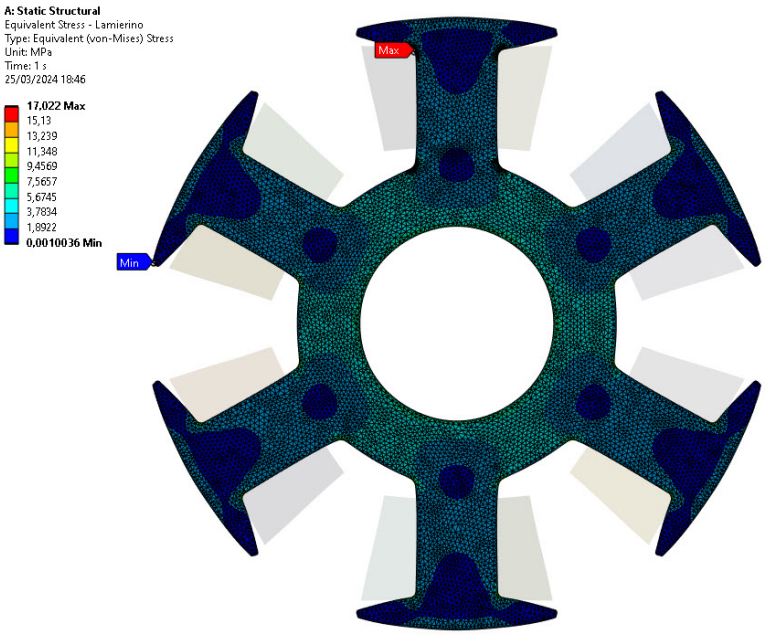

Figure 6.9: Von Mises equivalent stress with the traditional wound rotor.

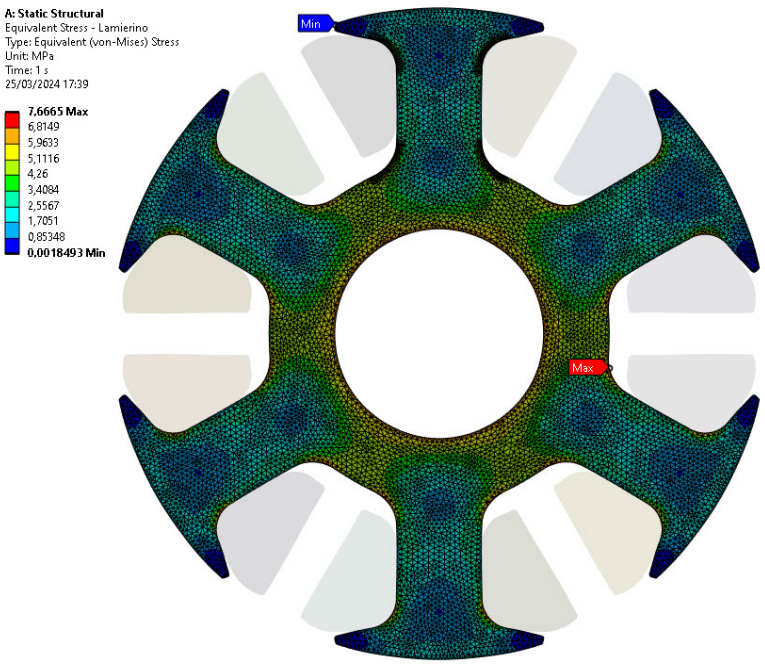

Figure 6.10: Von Mises equivalent stress with Aluminum AM coils.

According to these results, the proposed geometry with aluminum windings is the one with the lower maximum Von Mises equivalent stress. In the traditional original machine 17 MPa was detected in the connection between the pole body and the airgap pole shoe (Figure 6.9). Otherwise, with the proposed innovative geometry, the most stressed point is the connection between the pole body and the rotor, but the overall values are much lower than the ones obtained before, so the maximum value here is 7.7 MPa (Figure 6.10).

When copper coils are considered (Figure 6.11), the maximum stress obtained is a bit higher, 15.3 MPa, due to the fact that copper has a higher density.

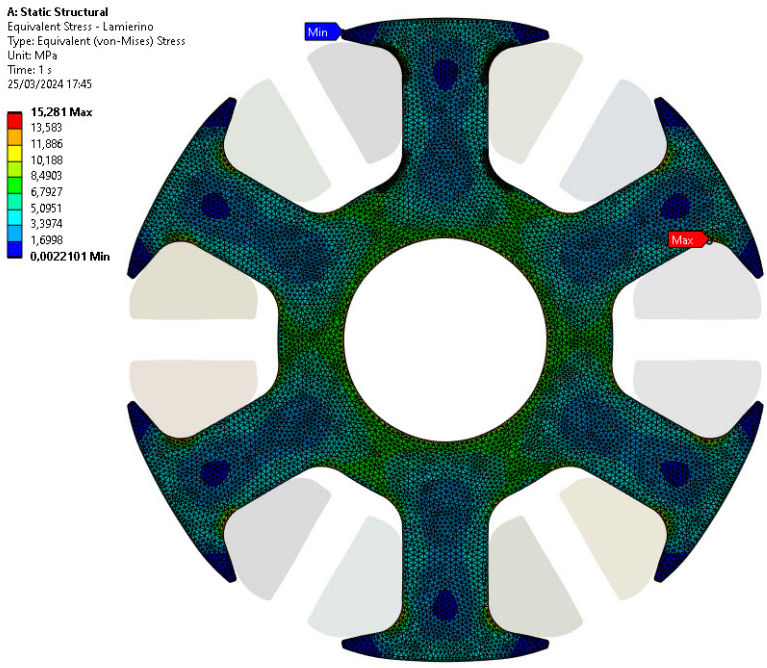

Figure 6.11: Von Mises equivalent stress with Copper AM coils.

Another important advantage from the mechanical point of view is that the proposed aluminum coil weights 24 % less than the traditional copper coil, despite the proposed winding geometry has higher volume.

The prototype is under construction, in Figure 6.12 the rotor poles are shown.

Figure 6.12: Rotor poles.

6.7 Conclusions

AM applied to electrical machines is gaining more and more interest thanks to the possibility of designing and manufacturing innovative optimized geometries. There are several applications in literature where AM is used to fabricate special stator hairpin windings, but in these applications the insulation of the windings is critical due to the PWM and high working voltages.

Here, AM is employed to design an innovative rotor winding for a synchronous electrically excited motor, in this case the insulation is less critical since the rotor winding is typically powered with low voltage DC current.

Furthermore a fluid pole shaping is made to reduce the mechanical stresses in the most critical points. The new coil geometry was designed with the purpose of maximizing the filling factor and granting constant cross section area of the conductors, to avoid undesired fluctuations in the current density of each conductor. The result is a coil design which perfectly fits into the pole shape obtained before. The final results of the comparison between the traditional and the innovative configurations can be summarized as follows.

1. The saturation in the pole, at the same working point, are reduced compared

to the ones obtained with the reference machine.

2. For the same MMF, the current density in rotor conductors is reduced by 60 %.

3. The rotor Joule losses generated with the innovative rotor configuration with aluminum windings are divided by 1.6 with respect to the ones obtained with the traditional motor. When copper is considered, this reduction increases to a factor of 2.5 . This is a very good achievement because it allows to modify the rotor winding material; in fact, using aluminum could lead to lower costs and total weight of the machine, with a gain in the overall efficiency of the machine.

4. The proposed pole shaping is characterized by lower mechanical stress in rotor most critical points and the total area at disposal can be exploited, creating a geometry which perfectly fits with the fluid pole shape.

5. The total coil weight is reduced by 24 % with aluminum.

A future development of this work could be, thanks to the potentialities of AM, the redesign of rotor end windings to obtain a geometry which increments the thermal dissipation of the machine.

6.8 References

[1] N. Giannotta, G. Sala, C. Bianchini, and A. Torreggiani, «A review of additive manufacturing of soft magnetic materials in electrical machines», *Machines*, vol. 11, no. 7, 2023, ISSN: 2075-1702. DOI: 10.3390/machines11070702. [Online]. Available: https://www.mdpi.com/2075-1702/11/7/702.

[2] L. Gargalis, V. Madonna, P. Giangrande, *et al.*, «Additive manufacturing and testing of a soft magnetic rotor for a switched reluctance motor», *IEEE Access*, vol. 8, pp. 206 982–206 991, 2020. DOI: 10.1109/ACCESS.2020.3037190.

[3] C. Wachter, F. Haller, and F. Liebetrau, «Additive manufactured copper conductors: Impedance characteristics of samples with varying density and cross-section profile», in *2022 12th International Electric Drives Production Conference (EDPC)*, 2022, pp. 1–5. DOI: 10.1109/EDPC56367.2022.10019767.

[4] N. Simpson, J. Jung, A. Helm, and P. Mellor, «Additive manufacturing of a conformal hybrid-strand concentrated winding topology for minimal ac loss in electrical machines», in *2021 IEEE Energy Conversion Congress and Exposition (ECCE)*, 2021, pp. 3844–3851. DOI: 10.1109/ECCE47101.2021.9595059.

[5] V. E. Vavilov, F. R. Ismagilov, E. I. Zaynagutdinova, *et al.*, «Improving the processibility of manufacturing windings of electrical machines using additive manufacturing methods: Experience of using A1Si10Mg and carbon nanotubes», in *2021 International Conference on Electrotechnical Complexes and Systems (ICOECS)*, 2021, pp. 636–641. DOI: 10.1109/ICOECS52783.2021.9657373.

[6] D. Sossong, D. Zdunek, and I. P. Brown, «Cast or additively manufactured coils with end turn enhanced heat transfer surfaces for spray or jet cooling», in *2023 IEEE Energy Conversion Congress and Exposition (ECCE)*, 2023, pp. 6061–6068. DOI: 10.1109/ECCE53617.2023.10362145.

[7] S. P. Munagala, Y. X. Pang, S. N. B. Hodgson, and N. Simpson, «Fabrication of insulation coatings on additively manufactured CuCrZr electrical windings», *IEEE Transactions on Dielectrics and Electrical Insulation*, vol. 31, no. 1, pp. 505–512, 2024. DOI: 10.1109/TDEI.2023.3324285.

[8] Y. Yang, X. Huang, and J. Fu, «Design and performance analysis of additively manufactured windings with high slot fill factor for permanent magnet synchronous motors», in *2023 26th International Conference on Electrical Machines and Systems (ICEMS)*, 2023, pp. 1384–1389. DOI: 10.1109/ICEMS59686.2023.10344756.

[9] A. Di Gioia, I. P. Brown, Y. Nie, *et al.*, «Design and demonstration of a wound field synchronous machine for electric vehicle traction with brushless capacitive field excitation», *IEEE Transactions on Industry Applications*, vol. 54, no. 2, pp. 1390–1403, 2018. DOI: 10.1109/TIA.2017.2784799.

[10] C. Rossi, D. Casadei, A. Pilati, and M. Marano, «Wound rotor salient pole synchronous machine drive for electric traction», in *Conference Record of the 2006 IEEE Industry Applications Conference Forty-First IAS Annual Meeting*, vol. 3, 2006, pp. 1235–1241. DOI: 10.1109/IAS.2006.256689.

[11] G. Petrelli, S. Nuzzo, T. Zou, D. Barater, G. Franceschini, and C. Gerada, «Review and future developments of wound field synchronous motors in automotive», in *2023 IEEE International Conference on Electrical Systems for Aircraft, Railway, Ship Propulsion and Road Vehicles & International*

Transportation Electrification Conference (ESARS-ITEC), 2023, pp. 1–6. DOI: 10.1109/ESARS-ITEC57127.2023.10114826.

[12] L. Cinti and N. Bianchi, «Optimal shaping for electrically excited synchronous motor», in *2023 IEEE International Conference on Electrical Systems for Aircraft, Railway, Ship Propulsion and Road Vehicles & International Transportation Electrification Conference (ESARS-ITEC)*, 2023, pp. 1–6. DOI: 10.1109/ESARS-ITEC57127.2023.10114885.

[13] L. Cinti, C. Contò, and N. Bianchi, «Fluid dynamic-based pole shaping for electrically excited synchronous motor», in *2023 IEEE Energy Conversion Congress and Exposition (ECCE)*, 2023, pp. 4016–4021. DOI: 10.1109/ECCE53617.2023.10362462.

[14] L. Cinti, C. Contò, and N. Bianchi, «A comparison between hybrid excited permanent magnet and wound rotor motor», in *2022 International Symposium on Power Electronics, Electrical Drives, Automation and Motion (SPEEDAM)*, 2022, pp. 14–19. DOI: 10.1109/SPEEDAM53979.2022.9842232.

[15] D. Michieletto, L. Cinti, and N. Bianchi, «Hybrid excitation PM synchronous motors: Part I – per unit analysis», *IEEE Transactions on Energy Conversion*, vol. 37, no. 1, pp. 487–494, 2022. DOI: 10.1109/TEC.2021.3107937.

[16] D. Michieletto, L. Cinti, and N. Bianchi, «Hybrid excitation PM synchronous motors: Part II — finite element analysis», *IEEE Transactions on Energy Conversion*, vol. 37, no. 1, pp. 495–504, 2022. DOI: 10.1109/TEC.2021.3107957.

[17] L. Cinti, P. G. Carlet, L. Ortombina, and N. Bianchi, «Flux-weakening control of hybrid-excited permanent magnet synchronous motors», in *2022 IEEE Energy Conversion Congress and Exposition (ECCE)*, 2022, pp. 1–8. DOI: 10.1109/ECCE50734.2022.9948090.

[18] J. JACOB, S. CALLIGARO, O. BOTTESI, and R. PETRELLA, «Design criteria for flux-weakening control bandwidth and voltage margin in ipmsm drives considering transient conditions», in *2019 IEEE Energy Conversion Congress and Exposition (ECCE)*, 2019, pp. 5667–5674. DOI: 10.1109/ECCE.2019.8913236.

7. A Double Three-Phase Axial-Flux Synchronous Reluctance Motor

Axial-flux machines have attracted growing interest in recent years due to their compact geometry, high torque density, and suitability for applications where axial space is limited.

In conventional manufacturing for radial flux machines, the rotor of a reluctance machine is typically realized through stacked laminations with well-defined flux barriers. While this approach is practical and widely adopted, it imposes strong geometric constraints that limit the manufacturability for axial flux motors. Additive Manufacturing (AM) offers a new degree of freedom in this context, allowing for the realization of complex three-dimensional structures that are not achievable using traditional techniques.

In this study, the design process begins with a traditional barrier-type rotor geometry, which serves as a reference configuration. Subsequently, a simplified rotor topology is proposed, with the objective of maximizing the magnetic flux transfer between the two stators. This approach not only enhances the electromagnetic coupling and torque production but also demonstrates how additive manufacturing can enable innovative design strategies that simplify construction while improving performance.

This chapter presents the design methodology, modeling considerations, and comparative analysis between the conventional and additively manufactured rotor configurations, highlighting the advantages and challenges associated with implementing AM in axial-flux reluctance machines.

The chapter is organized as follows: in Section 7.2 the main parameters related to motor geometry are presented and in Section 7.3 the proposed geometry is described, then, Section 7.4 describes the 2-D FEA simulations results obtained with a modified rotor geometry. To conclude, Section 7.5 shows the final design proposed and presents the 3-D FEA simulations results.

7.1 General overview

In recent years, there is continuous research about the design of new motors and new motor geometries. The main aims are:

- to increase the motor torque;
- to have compact electrical machines;
- to achieve a proper redundancy;
- to reduce the rare-earth material used in machine.

The synchronous reluctance machine has been studied for many years and only recently is adopted in industrial and traction applications. The analysis of this machine reached a maturity and the design procedure is well described in literature, e.g. [1].

The highest advantage of the synchronous reluctance machine is the total absence of permanent magnets, in particular of rare-earth permanent magnet. This aspects makes these motors highly sustainable, since rare-earth permanent magnets are expensive and of difficult disposal.

The torque is due to the rotor anisotropy, in particular to the difference of the d-axis and q-axis inductances. Thus the rotor is often characterised by several flux barriers that limit the flux along the q-axis without obstructing the flux along d-axis. Figure 7.1 shows the flux lines along d-axis and q-axis in a traditional radial flux motor.

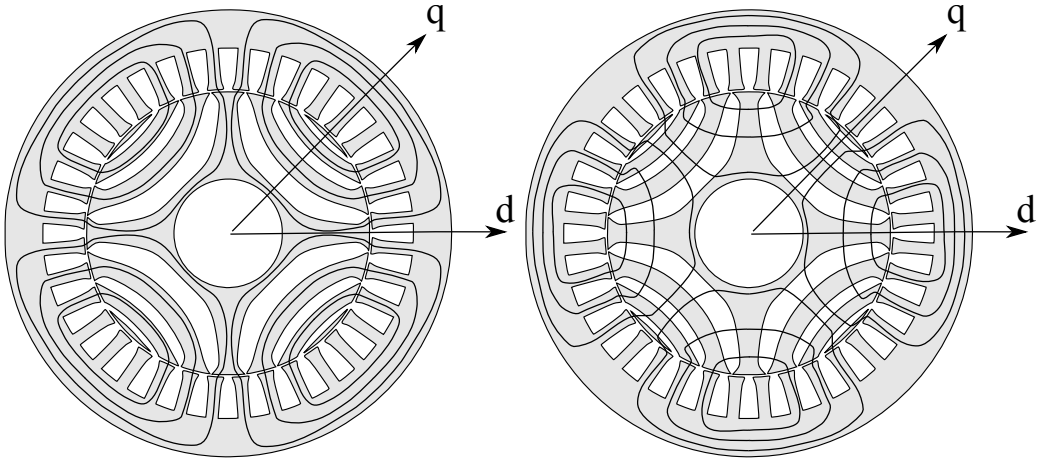

Figure 7.1: Flux lines along d-axis and q-axis in axially laminated motor.

Sometimes, low-energy PMs, like ceramic Ferrite, are adopted to saturate the iron bridges and to increase the power factor [2], [3], [4]. They are commonly adopted in radial flux machine, while they are barely used in axial-flux machine due to the complex structure of the rotor in such a configuration.

Figure 7.2 shows a possible rotor geometry of an axial-flux reluctance rotor, showing how the flux paths have to be designed. The difficulty of achieving such a geometry by using laminations is evident.

Nevertheless, it can be obtained using Soft Magnetic Composites (SMC) [5] or either with metal additive manufacturing, a new technology which allows customized geometries to be obtained for several applications. On the other hand, the rotor is not laminated, so eddy currents and hysteresis losses may be generated by flux density variations due to stator slots and MMF harmonics [6].

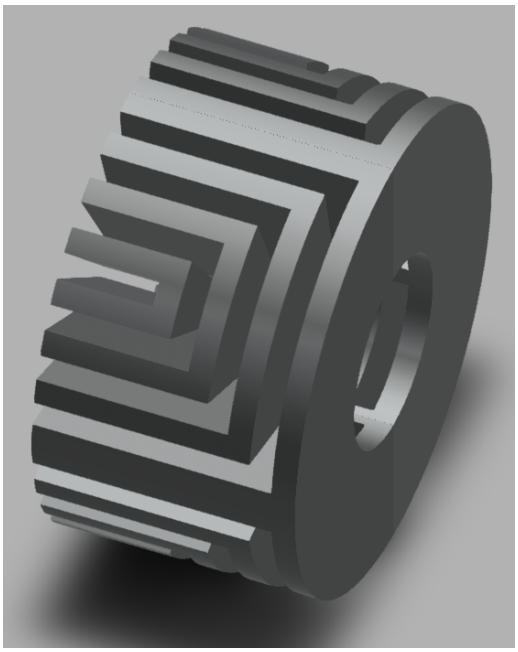

Figure 7.2: Complex geometry of an axial flux reluctance rotor.

Hysteresis losses are due to a non optimal grain dimension obtained during the additive manufacturing process. An annealing process can reduce significantly the impact of these losses, but this leads to an increment of the resistivity of the material, so eddy current losses will be higher. As authors state in [7], an annealing process is mandatory to obtain good performance from a 3D printed ferromagnetic core.

Nevertheless, additive manufaturing gives almost unlimited chances to redesign the

iron core geometry, included the possibility to introduce some micro structures to reduce the losses induced in the iron, as pointed out in [8]. In fact, authors in [9] build an additively manufactured iron core for a transformer exploiting the hilbert structure to reduce the induced current in the core and, consequently, the iron losses.

Axial flux machines are compact machine, characterised by a high torque per volume ratio. However, in comparison to the radial flux machine, in the axial flux machine there is a high axial force that acts on the two parts [10]. The stator is attracted by the rotor and vice versa. To compensate such an attractive force, it is possible to adopt an axial flux machine with one rotor and two stators [11], or two rotors and a single stator [12]. Hereafter a solution with two-stator and a single rotor is studied, where the two stator are powered by two different inverters, achieving a double three-phase machine.

Multi-phase motors are considered for various reasons. At first they allow the total power to be subdivided on different parts. This is advantageous especially for high-power machines, to split the current on various paths. Therefore they exhibit an intrinsecal redundancy, which make these solutions advantageous for fault-tolerant applications. In the event of a fault on a single three-phase set, the other three-phase set can continue to operate [13]. In addition, some solutions in which the two three-phase sets are shifted of 30 electrical degrees allow the MMF waveform to be improved, since some harmonics are removed [14].

Hereafter, an axial-flux synchronous reluctance machine is proposed. It is characterised by two stators and a single rotor in the middle. It is a **double three-phase machine**: the first set of three phase winding is addressed on the first stator, and the second set of three phase winding is addressed on the second stator.

7.2 Analytical Design

The proposed dual three-phase axial-flux synchronous reluctance machine is characterised by a single inner rotor and two external stators, each of them addressing a separate three-phase winding. The currents in the two winding sets are controlled separately, by means of the strategy described in the following.

Table 7.1 resumes the main data of the motor.

Table 7.1: Motor Parameters.

Name	Symbol	Value	U. M.
Pole Pair Number	p	2	-
Slot Number	Q	24	-
External Diameter	D_e	120	mm
Inner Diameter	D_i	50	mm
Air gap	g	0.3	mm
Rotor core height	h_r	15	mm
Stator core height	h_s	30	mm
Number of phases	m	3	-
Nominal frequency	f	50	Hz

7.2.1 Stator design

The two stators of the machine have the same geometrical dimensions, so the design of only one stator is needed. The stator slots have rectangular shape, as shown in Figure 7.3. A polar expansion can be added to have a better MMF distribution in the airgap.

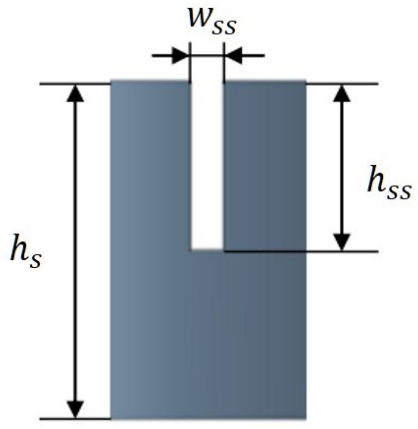

Figure 7.3: Stator slot dimensions.

Generally, the slot depth h_{ss}, the slot width w_{ss} and the slot pitch p_s can be considered related by:

$$h_{ss} = \left(\frac{h_{ss}}{w_{ss}}\right)\left(\frac{w_{ss}}{p_{ss}}\right)p_s \tag{7.1}$$

Where typically the two ratios needs to be in the following range of values:

$$\frac{h_{ss}}{w_{ss}} = 4 - 6 \tag{7.2}$$

$$\frac{w_{ss}}{p_s} = 0.4 - 0.6 \tag{7.3}$$

Choosing $h_{ss}/w_{ss} = 5$ and $w_{ss}/p_{ss} = 0.5$, the stator slot height results about 15 mm. Consequently, the stator slot width can be computed as

$$w_{ss} = \frac{h_{ss}}{\frac{h_{ss}}{w_{ss}}} = 3mm \tag{7.4}$$

The ratio between w_{ss} and p_s is 0.46, which stays in the range given in (7.3).

The final stator geometry is represented in Figure 7.4.

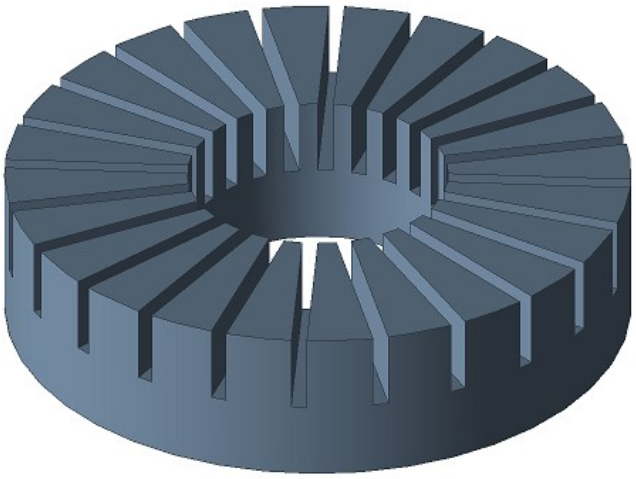

Figure 7.4: Stator core with 24 slots.

7.2.2 Traditional rotor design

The rotor has 4 poles, so each of them has an angular amplitude of $\theta_p = 90$ degrees. To reduce torque ripple it is important to compute the optimal number of barriers which depends on the slot-pole configuration of the machine. In this case a 4 barriers per pole design is chosen. The barriers need to be at the same distance in the circumferential direction, in this case spanning an angle of 5 degrees.

Figure 7.5 shows the rotor design with four flux barriers per pole. The geometry obtained is complex and difficult to manufacture, so in the following a simplification of the rotor geometry is proposed.

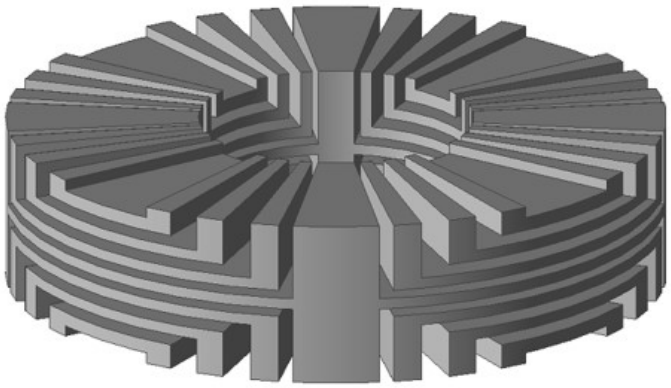

Figure 7.5: Rotor core.

7.3 The Motor Geometry Development

Since the classical reluctance geometry can be difficult to manufacture, a simplification of the original flux barrier configuration is proposed, with the purpose of maximizing the flux concatenated with the two stators.

As shown in Figure 7.6, the original number of flux barrier is reduced and the external one is removed. This is possible because in the central part of the rotor, there is no flux in the horizontal direction, considering the original geometry. Therefore, the horizontal iron layer can be replaced by air, and then the external flux barrier can be simplified. This is confirmed also with 2D FEA simulations, as shown in Figure 7.7.

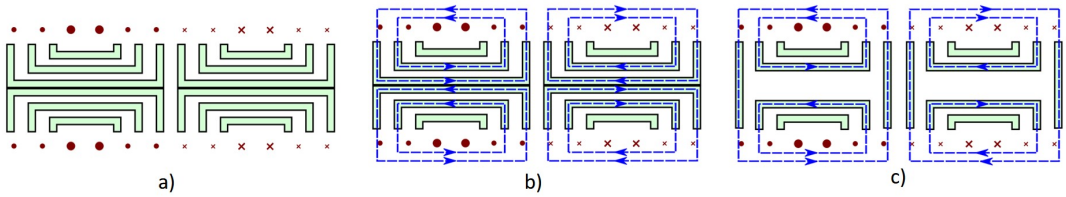

Figure 7.6: Flux barriers geometry evolution: starting from the classical geometry in (a) with a classical flux distribution, shown in (b), the new configuration is proposed in (c).

The flux barriers geometry can be re-designed in order to reduce the saturation in the rotor iron and therefore the torque ripple, which is particularly high in synchronous reluctance machines.

Furthermore, the total number of rotor slots has to be chosen carefully, according to [15], to minimize the torque ripple generated. Adopting the right number of rotor slots the saturation level of the rotor can be reduced with this geometry.

In Figure 7.7 and Figure 7.8 the 2D FEA post processor is reported for, respectively, the original geometry and the proposed one; according to these data, the maximum flux density value in the flux barrier is 1.7 T for the traditional geometry and 1.6 T for the proposed one.

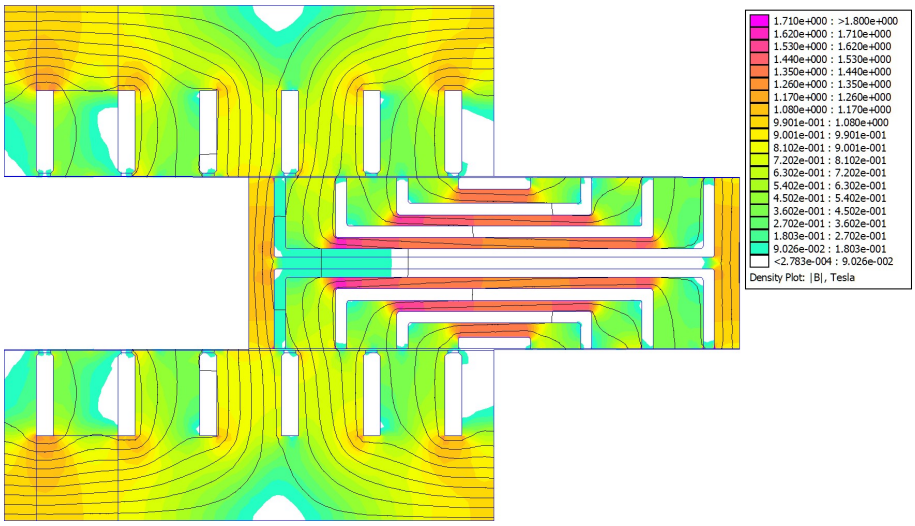

Figure 7.7: 2D FEA post processor of the original geometry.

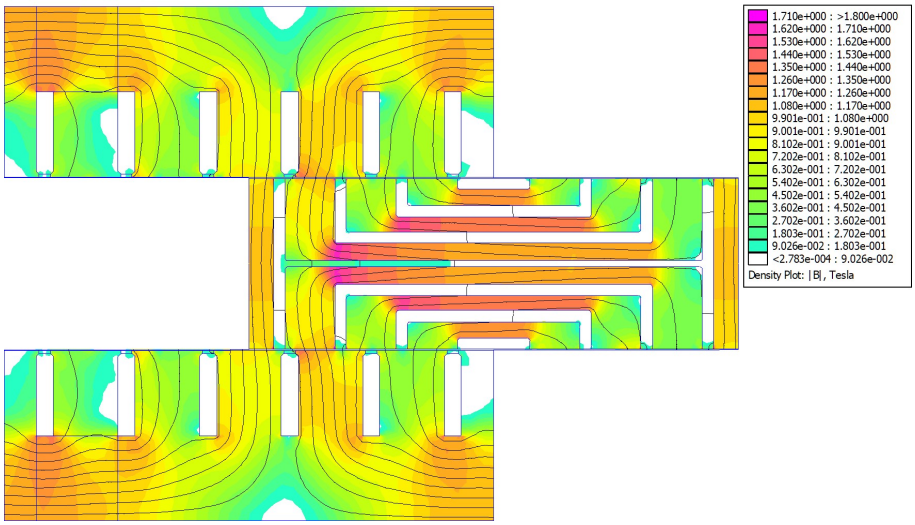

Figure 7.8: 2D FEA post processor of the proposed geometry.

7.4 2D FEA Simulations Results

The control of the flux angle is carried out controlling the phase angle of the currents of the two three-phase sets. In particular, thanks to the double stator configuration, it is possible to control separately the input currents to the two stators, with the purpose of obtaining a reduced torque ripple, which is one of the main drawback of traditional reluctance synchronous machines when the design is not optimized.

The torque obtained from the simulations of the two geometries is reported in Figure 7.9 and Figure 7.10.

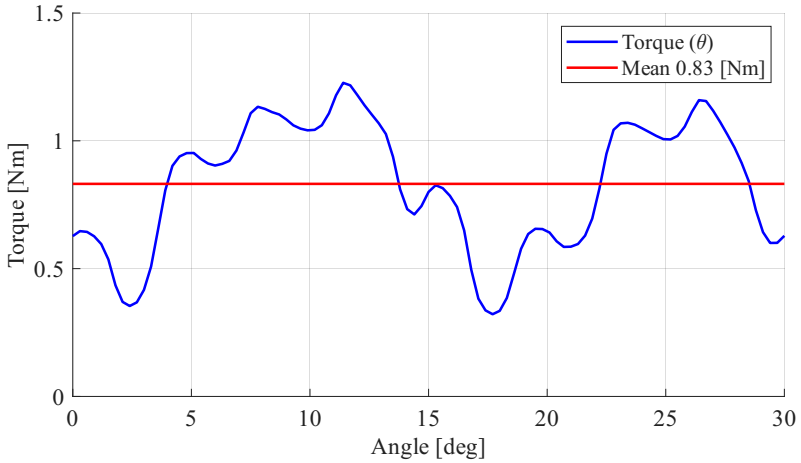

Figure 7.9: 2D FEA resulting torque of the original geometry.

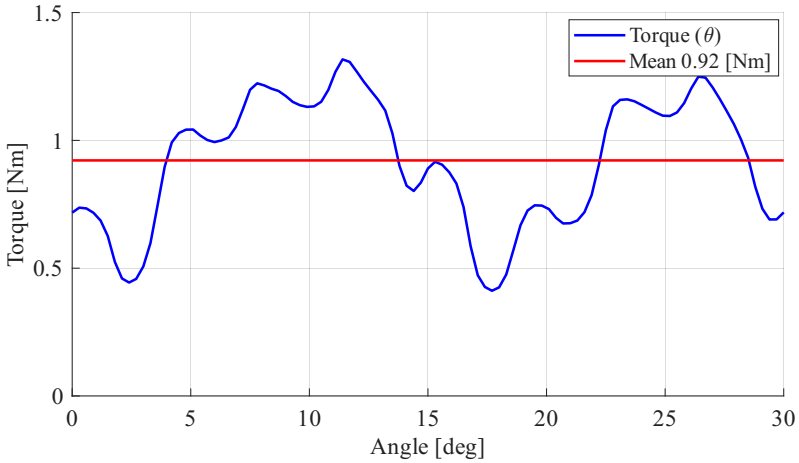

Figure 7.10: 2D FEA resulting torque of the proposed geometry.

At first the results obtained with the two stators powered with the same phase currents were considered. The main torque ripple frequency could be found and the angle shift at which the ripple is verified. This can be used as the power current angle of the second stator.

Furthermore, the mean torque value is incremented with the proposed geometry from 0.83 Nm to 0.92 Nm. In particular, in this case it is more interesting to evaluate the torque density per unit volume, computed as:

$$t = \frac{T}{Vol} \tag{7.5}$$

Where T is the mean torque generated by the machine and Vol is the machine volume. In this first comparison the volume of the two machines is the same, so the only parameter which affects the torque density is the mean torque.

The total volume of the machine is 1.02 dm^3 so the torque density is 0.8 Nm/dm^3 for the traditional geometry and 0.9 Nm/dm^3 for the proposed one.

The torque ripple of the traditional configuration is 0.85 Nm while the one of the proposed new geometry is 0.65 Nm. It is worth noting that it remains still high, but the improvement from the traditional configuration is significant.

7.5 New Geometry Proposal and 3D FEA Simulations Results

Starting from the configuration proposed in Section 7.4, a new geometry proposal is made, with the purpose of further simplifying the manufacturing of the rotor. In Figure 7.11 a representation of the new topology is shown: the flux barriers of the rotor are reduced to a single radial barrier, so the circumferential part is removed. The flux can now flow directly from one stator to the other.

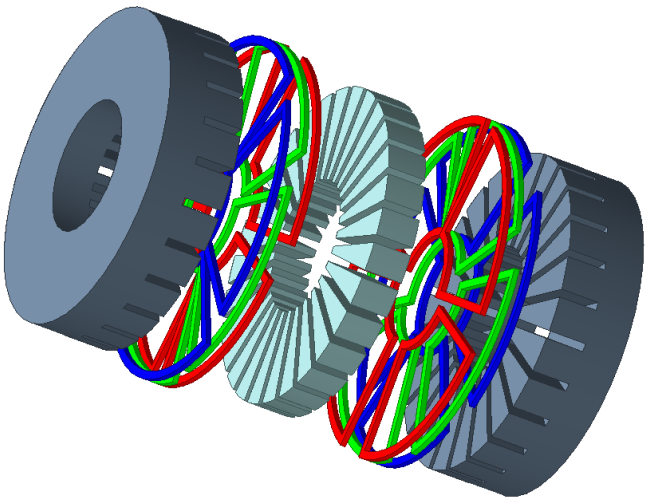

Figure 7.11: 3D sketch of the new geometry proposed.

Exploiting the double three-phase systems, the control of the flux angle is carried out controlling the phase angle of the currents of the two three-phase sets. In particular the flux angle is varied acting on the shift between the currents controlled in the two separate three-phase stators.

Thanks to this control technique the rotor flux barriers are completely modified and the rotor manufacturing results simplified.

The purpose is powering the two stators with currents that can ensure high torque and low torque ripple.

At first, the two stators are powered with the same current. A sketch of the flux lines induced in this case is shown in Figure 7.12. The flux lines flow from one stator iron to the other stator iron flowing on the rotor iron paths, without considering the

air barriers between them. Such a flux corresponds to the d-axis flux.

This behaviour is the same for all the current angle. The motor operates without seeing any saliency, the flux value is maximum and the machine does not produce any torque.

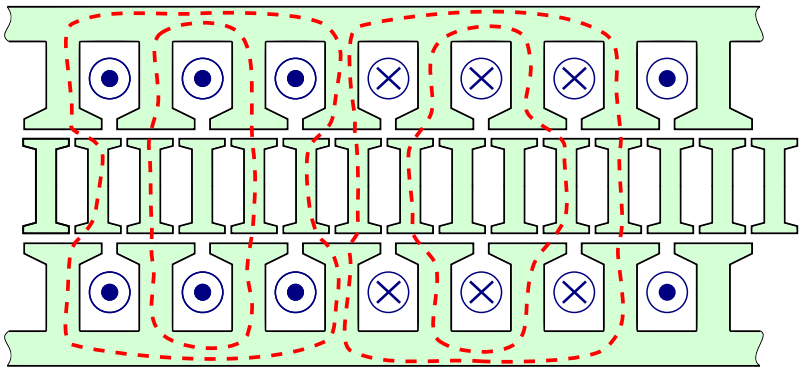

Figure 7.12: Sketch of the d-axis flux lines when the currents of the two stators are in phase.

Then, thanks to the double stator and the chance to have a double three phase system, the two stators are powered with different current angles.

Figure 7.13 shows a sketch of the flux lines when the currents of the two stators are of phase of 180 electrical degrees. The flux lines flow from each stator iron to the rotor and they flow back to the same stator crossing the rotor flux barriers. Thus the flux is strongly limited by the rotor flux barriers. Such a flux corresponds to the q-axis flux.

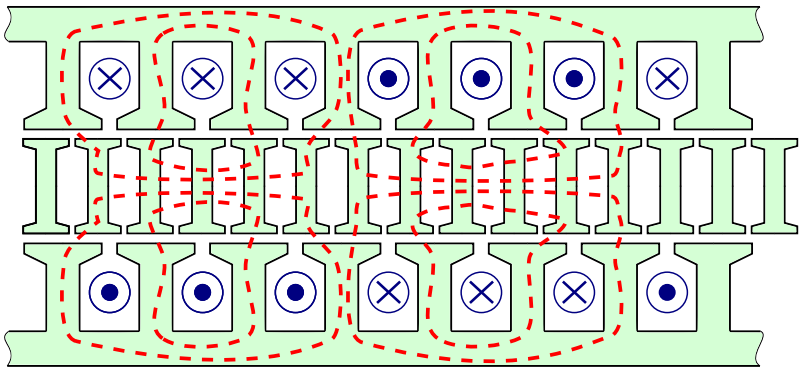

Figure 7.13: Sketch of the q-axis flux lines when the currents of the two stators are out of phase.

Figure 7.16 a) shows the 3D sketch of the proposed rotor design.

As stated before, this configuration when both the windings are excited with the same current does not produce any torque. For this reason, the stators are now powered with two different current angle. The first stator is powered with only direct-axis current and the other with quadrature-axis current. The purpose is to have one stator producing the flux and the other one powered with a current generating the torque.

The flux lines generated by the two stators, shown in Figure 7.14, are both generating a torque contribution, but the two stators produced torque in opposites directions. The global result is an average torque value which is near to zero.

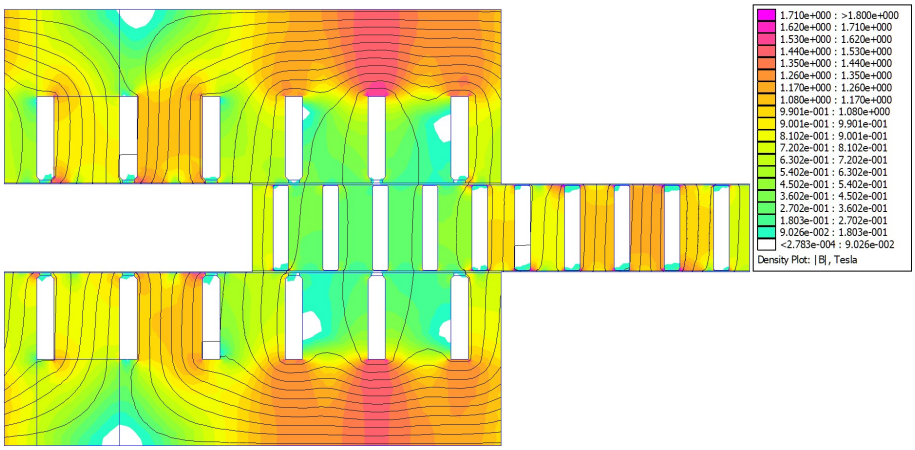

Figure 7.14: 2D FEA post processor of the simplified rotor design with constant rotor teeth width with one stator powered with d-axis current and the other with q-axis current.

Since the two stators generate a torque, a single stator motor was simulated with the proposed rotor design. Nevertheless, the motor does not generates torque.

This is due to the fact that the stator does not recognize the pole geometry in the rotor, so some anisotropy was introduced, as shown in Figure 7.16, where starting from the just described solution, Figure 7.16 a), the tooth height is modified progressively.

In Figure 7.16 b) the tooth height is modified only on one side of the rotor; this solution was simulated considering only one stator. The total geometry is reported in Figure 7.15. This configuration introduces a variable permeability path for the flux, allowing torque generation.

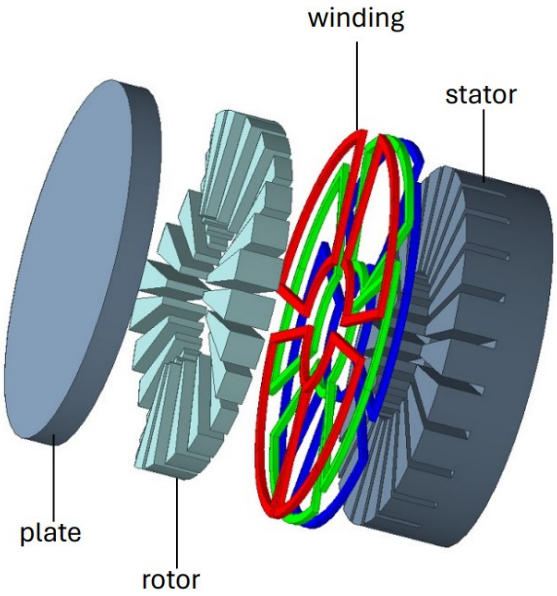

Figure 7.15: Single stator motor geometry with variable rotor teeth height.

Figure 7.16 c) shows the final rotor design proposed for a dual stator axial motor. A variable height of the rotor teeth is designed to obtain magnetic paths between stator and rotor with variable permeability. The proposed rotor design has a sinusoidal trend through the air gap. The geometry obtained is greatly simplified compared to the more traditional reluctance machine design (reported in Figure 7.5).

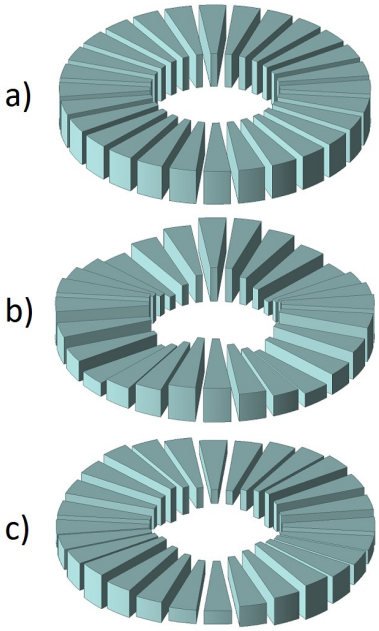

Figure 7.16: 3D representation of the rotor evolution: constant rotor tooth width (a), variable tooth height on one side of the rotor (b) and variable tooth height on both side of the rotor (c).

Furthermore, the new rotor geometry allows to reduce the rotor total thickness thanks to the removal of complex barriers. The 3D sketch of the proposed geometry is reported in Figure 7.17.

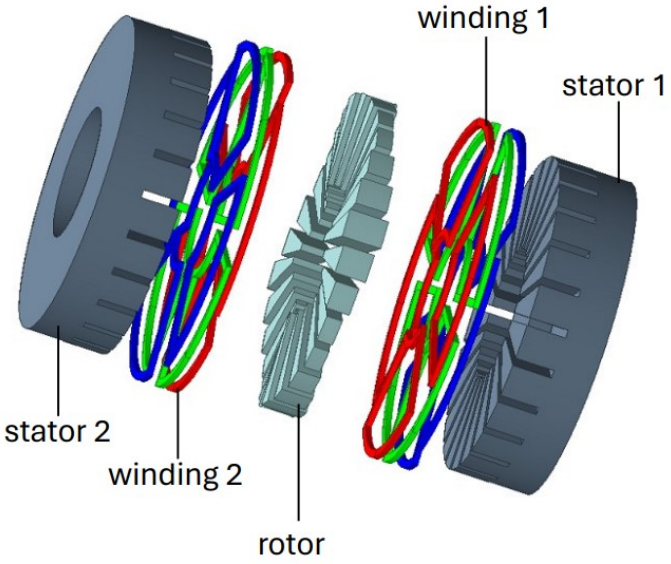

Figure 7.17: 3D sketch of the new geometry proposed with variable rotor tooth height.

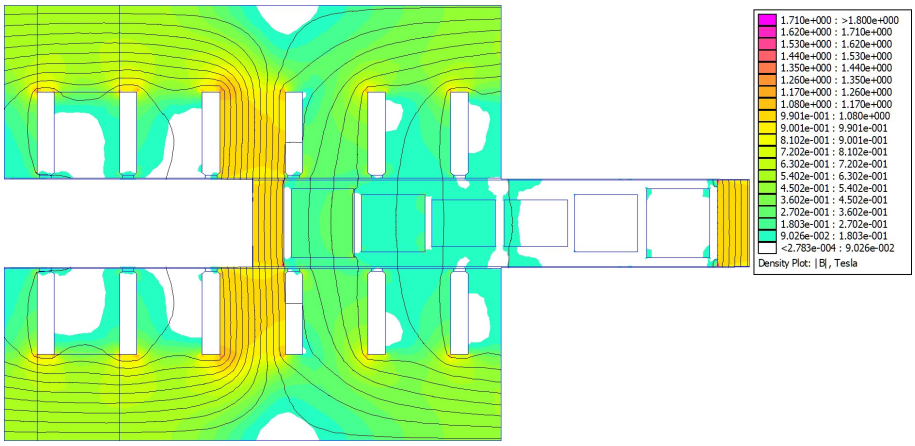

Figure 7.18: Flux density distribution in the rotor from 2D FEA simulations.

The resulting average torque of the proposed geometry is 1.6 Nm, higher than the one obtained with the traditional geometry. The volume of the new rotor is halved with respect to the original one, so the total volume of the machine is 0.86 dm^3. So the torque density per unit volume is 1.86 Nm/dm^3.

Another important aspect of the new geometry is the low saturation of the rotor. In the traditional configuration the flux barriers had quite high saturation level due to

the thin iron ribs between the barriers; in the new rotor configuration the saturation level reached in the operating point considered is much lower (see Figure 7.19). The maximum flux density value in rotor teeth is about 1.5 T.

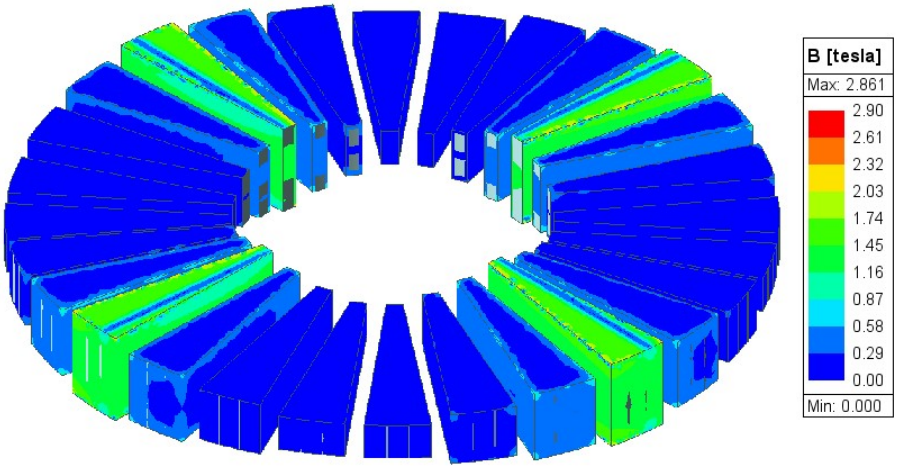

Figure 7.19: Flux density distribution in the motor from 3D FEA simulations.

A parametric study based on the per-unit current i_{pu} of the stator is made. The per unit current is defined as follows.

$$i_{pu} = \frac{I}{I_{nom}} \tag{7.6}$$

The trend of the torque is reported in Figure 7.20 and Figure 7.21.

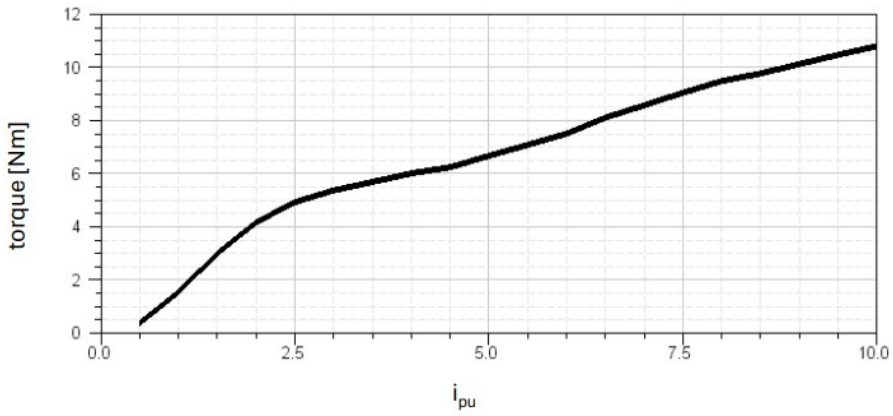

Figure 7.20: Torque trend as a function of the per unit current of the stator.

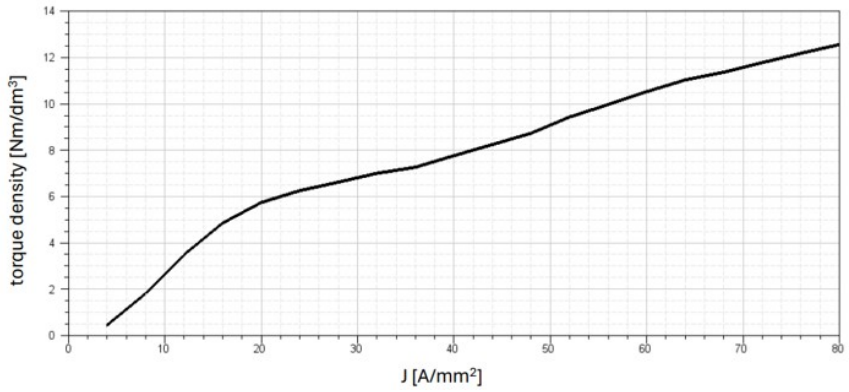

Figure 7.21: Torque density per unit volume trend as a function of the current density of the stator.

To keep a reasonable value of saturation in the rotor (around 2 T) the current density that should be considered is about 20 A/mm^2 and the torque density obtained is 6 Nm/dm^3.

A comparison between the performance obtained from the proposed machine can be made with an axial flux permanent-magnet spoke-type coreless machine reported in [16]. The paper investigates the flux focusing technique in coreless structures with NdFeB PMs. The motor proposed in the paper has a double rotor configuration and a comparison with traditional surface mounted PM machines is made analytically.

The performance obtained in [16] are reported here in terms of torque density per unit volume, in order to obtain a fair comparison. The external overall volume of the machine considered in the paper is 0.6 dm^3 the torque obtained in the paper is 4.6 Nm with a current density of 19 A/mm^2; so the torque density per unit volume is 7.67 Nm/dm^3.

Referring to the innovative reluctance machine proposed here at 19 A/mm^2, the torque density is about 5.5 Nm/dm^3, which is comparable to the one obtained with the permanent magnet coreless machine. With the advantages of having completely removed the rare earth in the motor and simplified the rotor structure to obtain.

7.6 Conclusions

An innovative rotor geometry for a double three phase axial flux synchronous reluctance machine was presented. The main purpose was to obtain a simplified rotor

design. The flux barriers, typical for reluctance radial machines, in axial configuration become difficult to be manufactured with traditional manufacturing techniques. So, a new rotor design was made in three steps:

- Firstly, the external flux barrier was removed because the flux in the internal horizontal iron path is null, so the last barrier can be removed. The proposed design allows to reduce the saturation level in the rotor. This leads to a reduction of the torque ripple and an increment of the average torque generated.
- Then, to maximize the flux flowing from one stator to the other, the flux barriers in the rotors are removed and substituted with rotor teeth. The two stators can be powered separately. Thanks to the double three phase system, it is possible to obtain the d-axis or the-q axis flux by modifying the current angle of the two stators. When the stators are powered with the same current angle, they are generating torque in opposite directions, resulting in a null average torque contribution. Also a single stator design configuration was analyzed with the proposed rotor geometry. The average torque produced is still null, because there is no anisotropy in the rotor.
- The designed geometry could not ensure the right anisotropy of the rotor, so the height of the different rotor teeth was modified. In this way, iron paths with variable permeability are introduced with a sinusoidal trend of the variable height of the rotor teeth. The machine proposed has a saliency and generates a torque value comparable with other axial flux machines.

The final design shows good results both in terms of generated torque per unit volume and rotor iron saturation. The total volume of the motor is reduced. This reduction is obtained thanks to the simplification of the rotor geometry. The initial rotor dimensions are halved; nevertheless, the average torque generated increment. In addition, with the new rotor design there is a lower saturation in the iron paths when the motor is powered with the same current density of the traditional geometry.

The innovative motor proposed allows to obtain performance that are comparable to the one of others axial flux PM machines with similar dimensions. The main advantages of the proposed rotor design are:

- The absence of permanent magnets, so the absence of rare earth materials

inside the machine. Notoriously they are expensive and difficult to dispose.

- An easy geometry of the rotor which allow to obtain the desired saliency, so a good torque value, without the traditional flux barriers.
- A good flux density distribution in the rotor which allows to reduce the saturation value in the rotor barrier.

7.7 References

[1] A. Vagati, A. Canova, M. Chiampi, M. Pastorelli, and M. Repetto, «Design refinement of synchronous reluctance motors through finite-element analysis», *IEEE Transactions on Industry Applications*, vol. 36, no. 4, pp. 1094–1102, 2000. DOI: 10.1109/28.855965.

[2] A. Vagati, B. Boazzo, P. Guglielmi, and G. Pellegrino, «Ferrite assisted synchronous reluctance machines: A general approach», in *2012 XXth International Conference on Electrical Machines*, 2012, pp. 1315–1321. DOI: 10.1109/ICElMach.2012.6350047.

[3] A. Vagati, B. Boazzo, P. Guglielmi, and G. Pellegrino, «Design of ferrite-assisted synchronous reluctance machines robust toward demagnetization», *IEEE Transactions on Industry Applications*, vol. 50, no. 3, pp. 1768–1779, 2014. DOI: 10.1109/TIA.2013.2284302.

[4] B. Raghuraman, S. Nategh, N. Sidiropoulos, L. Petersson, and A. Boglietti, «Sustainability aspects of electrical machines for e-mobility applications part i: A design with reduced rare-earth elements», in *IECON 2021 – 47th Annual Conference of the IEEE Industrial Electronics Society*, 2021, pp. 1–6. DOI: 10.1109/IECON48115.2021.9589246.

[5] N. Ahmed and G. J. Atkinson, «A review of soft magnetic composite materials and applications», in *2022 International Conference on Electrical Machines (ICEM)*, 2022, pp. 551–557. DOI: 10.1109/ICEM51905.2022.9910712.

[6] A. Cavagnino, S. Vaschetto, E. Pošković, A. Fortunato, and E. Liverani, «Magnetic behavior and loss assessment of additively manufactured fe-si alloys», in *2023 IEEE International Electric Machines & Drives Conference (IEMDC)*, 2023, pp. 1–6. DOI: 10.1109/IEMDC55163.2023.10238925.

[7] M. Garibaldi, I. Ashcroft, J. Lemke, M. Simonelli, and R. Hague, «Effect of annealing on the microstructure and magnetic properties of soft magnetic fe-si produced via laser additive manufacturing», *Scripta Materialia*, vol. 142, pp. 121–125, 2018, doi:10.1016/j.scriptamat.2017.08.042, ISSN: 1359-6462.

[8] R. Wrobel and B. Mecrow, «Additive manufacturing in construction of electrical machines – a review», in *2019 IEEE Workshop on Electrical Machines Design, Control and Diagnosis (WEMDCD)*, vol. 1, 2019, pp. 15–22. DOI: 10.1109/WEMDCD.2019.8887765.

[9] A. Plotkowski, K. Carver, F. List, *et al.*, «Design and performance of an additively manufactured high-si transformer core», *Materials & Design*, vol. 194, p. 108 894, 2020, doi.org/10.1016/j.matdes.2020.108894, ISSN: 0264-1275.

[10] D. J. Patterson, G. Heins, M. Turner, B. J. Kennedy, M. D. Smith, and R. Rohoza, «An overview of the compactness of a range of axial flux pm machines», in *2017 IEEE Workshop on Electrical Machines Design, Control and Diagnosis (WEMDCD)*, 2017, pp. 27–32. DOI: 10.1109/WEMDCD.2017.7947719.

[11] Q. A. S. Syed, H. Kurtovic, and I. Hahn, «Double stator and single rotor type single-phase flux switching axial flux permanent magnet motor», in *2017 20th International Conference on Electrical Machines and Systems (ICEMS)*, 2017, pp. 1–5. DOI: 10.1109/ICEMS.2017.8056172.

[12] J. H. Kim, Y. Li, and B. Sarlioglu, «Novel dual-rotor single-stator axial flux switching permanent magnet machine with even harmonic elimination topology», in *2015 Intl Aegean Conference on Electrical Machines & Power Electronics (ACEMP), 2015 Intl Conference on Optimization of Electrical & Electronic Equipment (OPTIM) & 2015 Intl Symposium on Advanced Electromechanical Motion Systems (ELECTROMOTION)*, 2015, pp. 506–512. DOI: 10.1109/OPTIM.2015.7426994.

[13] I. Bolvashenkov, J. Kammermann, H.-G. Herzog, I. Frenkel, E. Ikar, and L. Khvatskin, «Investigation of reliability and fault tolerance of multi-phase traction electric motor supplied with multi power source based on lz-transform», in *2017 2nd International Conference on System Reliability and Safety (ICSRS)*, 2017, pp. 303–309. DOI: 10.1109/ICSRS.2017.8272839.

[14] H. Dhulipati, S. Mukundan, W. Li, J. Tjong, and N. C. Kar, «Investigation of phase angle displacements in six-phase pmsm with concentrated windings for reduced mmf harmonics», in *2018 21st International Conference on*

Electrical Machines and Systems (ICEMS), 2018, pp. 308–313. DOI: 10.23919/ICEMS.2018.8549176.

[15] A. Vagati, M. Pastorelli, G. Francheschini, and S. Petrache, «Design of low-torque-ripple synchronous reluctance motors», *IEEE Transactions on Industry Applications*, vol. 34, no. 4, pp. 758–765, 1998. DOI: 10.1109/28.703969.

[16] F. Marcolini, G. De Donato, F. G. Capponi, M. Incurvati, M. Schiestl, and F. Caricchi, «Analysis and design of a low-speed, spoke-type coreless axial-flux permanent-magnet motor», in *2023 IEEE Energy Conversion Congress and Exposition (ECCE)*, 2023, pp. 3759–3766. DOI: 10.1109/ECCE53617.2023.10361947.

Conclusions

The main contributions of this thesis are discussed hereafter. The focus of the thesis was the development of high performance electric motors exploiting the advantages of additive manufacturing. Thanks to this manufacturing technique it is possible to obtain complex and optimized geometries. This thesis starts from the analytical basement for the modeling of electrical machines, moving on to their design and optimization, up to the design of three innovative motor topologies that exploit additive manufacturing and complex shapes to maximize their performance without the usage of rare earths.

Chapter 1 presents an overview of electrical machines topologies and their most general analytical model. In the end a lumped parameter non linear model for fast simulation is presented. This model was developed during the PhD to obtain a direct model in PLECS® that could have as an input the results obtained from 2D FEA. The model takes into account the non linearities of the machine and the iron losses. The simulations were compared with experimental results to validate the model.

Chapter 3 exposes the classical analytical design procedure for electrical machines. Then an analytical optimization method that include the iron losses is proposed. Given a range of external diameters it is possible to obtain for each of them the machine with minimized volume. In this way the mass of the motor is minimized, leading to the maximization of the power density of the machine.

In Chapter 4 a literature overview about metal additive manufacturing applied to soft magnetic materials is presented. Aspects such as iron losses, mechanical defects and the effects of post processing treatments like annealing are analyzed and deepened.

All of the concepts reported in the previous chapters were exploited to carry out the design of three innovative machines.

The first one is a tubular synchronous reluctance machine (Chapter 5). A novel

pure synchronous reluctance tubular linear motor was developed, featuring a complex rotor geometry made possible by metal additive manufacturing. An analytical lumped-parameter model was formulated and validated against 2D finite-element simulations, showing good agreement across operating conditions. Design optimization identified an optimal rotor diameter ratio between 0.54 and 0.58 and recommended at least four rotor layers with an air-gap-to-pole-pitch ratio of about 22 % to minimize force ripple. Prototype measurements confirmed the accuracy of both the analytical and simulation results, demonstrating the feasibility and effectiveness of the proposed design.

The second innovative machine design is described in Chapter 6. Additive manufacturing was applied to the design of an innovative rotor winding for a wound-field synchronous motor, enabling complex geometries and a higher slot fill factor. Unlike stator applications, insulation requirements are less critical due to the low-voltage DC excitation of the rotor. A fluid pole shape was also introduced to reduce mechanical stress and ensure an optimal fit of the new coil geometry. The optimized design achieved significant performance improvements: magnetic saturation was reduced, rotor current density decreased by 60 %, and Joule losses were lowered by factors of 1.6 with aluminum and 2.5 with copper compared to the conventional configuration. Additionally, the total coil weight was reduced by 24 % when aluminum was used. These results demonstrate the effectiveness of AM in enhancing both the electromagnetic and mechanical performance of wound-field rotors. Future developments could focus on redesigning the rotor end windings to further improve thermal dissipation.

To conclude, an axial flux machine design was reported in Chapter 7. An innovative rotor geometry for a double three-phase axial flux synchronous reluctance motor was developed to simplify the rotor structure and overcome the manufacturing limitations of conventional flux barriers. The design process evolved through successive simplifications, ultimately replacing traditional barriers with shaped rotor teeth to facilitate flux transfer between the two stators. By varying the height of these teeth, a sinusoidal permeability profile was achieved, introducing rotor saliency and enabling effective torque generation. The final configuration demonstrated improved performance, with higher average torque, reduced torque ripple, and lower iron saturation compared to the initial design. The overall motor volume was halved while

maintaining torque levels comparable to similar axial-flux machines. Moreover, the rotor geometry eliminates the need for permanent magnets, avoiding the use of rare-earth materials, reducing costs, and simplifying recyclability. The proposed design thus combines mechanical simplicity, good electromagnetic performance, and sustainable material use.

The shift from subtractive to Additive Manufacturing represents a fundamental change in how high-performance electric motors are conceived. By removing the constraints of traditional tooling, the transition from "design for manufacture" to "manufacture for design" is made, allowing for electromagnetic and thermal optimizations that were previously physically impossible.

The main limitations of conventional manufacturing are:

- high waste of material;
- long lead times due to custom tooling;
- high energy intensity in raw material processing.

Additive manufacturing allows to overcome the traditional constraints of conventional manufacturing, since it ensures:

- minimal waste, thanks to near net shape production;
- rapid prototyping and direct production;
- reduced carbon footprint through optimized weight;
- the chance to optimize the design to maximize the performance of the machine, such as the insertion of integrated cooling channels.

The adoption of AM in the electric motors sector directly addresses the global demand for sustainability. The ability to produce lightweight components reduces the overall inertia of the motor, leading to higher system efficiency and lower energy consumption during the operational phase. Furthermore, the reduction in raw material usage and the potential for localized production significantly reduce the environmental impact of the supply chain, aligning the electric machine industry with circular economy goals.

The findings of this research suggest that AM will be the cornerstone of the next generation of traction motors, particularly in high-stakes industries such as aerospace

and automotive racing.

The main disadvantage of additive manufacturing is the high cost, but in the long term, as AM scales and costs decrease, we can expect a democratized access to high-efficiency machines.

An important aspect that was deepened in this thesis is related to the properties of printed materials, which are responsive to printing parameters and post processing treatments. As pointed out in this thesis, after a printing process a post processing annealing treatment is mandatory to increase the magnetic properties of the printed material. The annealing cycle that must be implemented improves magnetic properties of the printed material but it reduces its mechanical properties. A good trade off between mechanical resistance and magnetic performance of the material must be found, depending on the specific application.

The next frontier in AM for electric machines lies in multi-material printing. Future research should focus on the simultaneous deposition of conductive, magnetic, and insulating materials. Developing functionally graded components, where material properties change locally to optimize magnetic flux or thermal dissipation, could lead to a level of power density that is currently unattainable with mono-material processes.

This thesis has demonstrated the potential of AM for high-performance electric motors, several avenues remain for further exploration to bridge the gap between prototyping and large-scale industrial adoption. To move beyond high-performance applications (such as aerospace or motor sport), the scalability of the AM process must be addressed. Future studies should investigate:

- high-speed printing techniques to reduce manufacturing time and costs;
- certification and qualification protocols to ensure the structural integrity and fatigue resistance of printed parts over long operational life cycles.

As the carbon footprint becomes a primary KPI, future work should evaluate the recyclability of 3D-printed metal powders. Investigating life-cycle assessments (LCA) for AM-produced motors—comparing the energy saved during operation (due to light weighting) against the energy used in the printing process will provide a definitive road map for the green future of electric mobility.

Finally, the list of published and under revision works is reported hereafter.

Published works:

1. C. Bianchini; G. Sala; A. Torreggiani; N. Giannotta; M. Davoli; E. Macrelli; F. Immovilli; A. Bellini, "Synchronous Reluctance Tubular Machine by Means of Additive Manufacturing," 2022 International Conference on Electrical Machines (ICEM), Valencia, Spain, 2022, pp. 921-927, doi: 10.1109/ICEM51905.2022.9910808.

2. C. Bianchini, A. Torreggiani, G. Sala, A. Sala, N. Giannotta and M. Davoli, "2-D FEA Design of a Low-Cost and Self-Powered Sin/Cos Sensor," 2024 International Conference on Electrical Machines (ICEM), Torino, Italy, 2024, pp. 1-7, doi: 10.1109/ICEM60801.2024.10700587.

3. C. Bianchini, N. Bianchi, G. Sala, N. Giannotta and A. Torreggiani, "Innovative Rotor Winding Geometry for Synchronous Machine by Means of Additive Manufacturing," 2024 International Conference on Electrical Machines (ICEM), Torino, Italy, 2024, pp. 01-07, doi: 10.1109/ICEM60801.2024.10700314.

4. C. Bianchini, G. Sala, M. Frigieri, M. Vogni, N. Giannotta and E. Macrelli, "Extended MTPA-FW Control Technique for PM Electrical Machines with CSI," 2024 International Conference on Electrical Machines (ICEM), Torino, Italy, 2024, pp. 1-7, doi: 10.1109/ICEM60801.2024.10700071.

5. C. Bianchini, N. Bianchi, L. Cinti, M. Davoli and G. Sala, "Design of High Power Density IPM Machines with Fractional or Integral Slot for Off-Highway Vehicles," 2024 International Conference on Electrical Machines (ICEM), Torino, Italy, 2024, pp. 1-7, doi: 10.1109/ICEM60801.2024.10700348.

6. G. Sala, C. Bianchini, M. Vogni, E. Macrelli and A. Bellini, "Current Source Inverter Drive of an Ironless Motor for Flywheel Batteries," 2024 IEEE Energy Conversion Congress and Exposition (ECCE), Phoenix, AZ, USA, 2024, pp. 354-358, doi: 10.1109/ECCE55643.2024.10861673.

7. N. Bianchi, G. Sala and C. Bianchini, "A Double Three-Phase Axial-Flux Synchronous Reluctance Motor," 2024 IEEE Energy Conversion Congress and Exposition (ECCE), Phoenix, AZ, USA, 2024, pp. 5794-5801, doi: 10.1109/

ECCE55643.2024.10861291.

8. C. Bianchini, G. Sala, M. Frigieri, M. Vogni, N. Giannotta and A. Capitanio, "Inductance Based Lumped Parameter IPM Machine Model for Fast Simulation," 2024 IEEE Energy Conversion Congress and Exposition (ECCE), Phoenix, AZ, USA, 2024, pp. 5262-5268, doi: 10.1109/ECCE55643.2024.10861024.

9. G. Sala, S. Ferrari, G. Pellegrino, C. Bianchini and M. Davoli, "Influence of MTPA Trajectory Evaluation on Synchronous Machines Performance," 2025 IEEE Workshop on Electrical Machines Design, Control and Diagnosis (WEMDCD), Valletta, Malta, 2025, pp. 1-6, doi: 10.1109/WEMDCD61816.2025.11014114.

10. N. Giannotta, G. Sala, G. Puccio, B. Kallenbach, C. Bianchini and S. Nuzzo, "Effect of Annealing and Building Direction on the Magnetic Behavior of Additively Manufactured FeCo49V2 Alloy," 2025 IEEE Workshop on Electrical Machines Design, Control and Diagnosis (WEMDCD), Valletta, Malta, 2025, pp. 1-6, doi: 10.1109/WEMDCD61816.2025.11014110.

11. A. Capitanio, G. Sala, G. Franceschini, A. Esmaelina, I. G. de Madinabeitia, A. Pastore, M. Tranchero, M. Saur, “Improve Modeling, Control, and Health Monitoring of an E-Motor Applying an Integrated Flux Sensor Array: Concepts and Design”, 17th International Conference on Engines & Vehicles for Sustainable Transport, Capri, Italy, 2025.

12. G. Sala, C. Bianchini, E. Macrelli, A. Bellini, N. Bianchi, “Electric Machine Design: An Attempt to Apply Artificial Intelligence”, 2025 IEEE Energy Conversion Congress and Exposition (ECCE), Philadelphia, PA, USA, 2025.

13. Giannotta, N.; Sala, G.; Bianchini, C.; Torreggiani, A. A Review of Additive Manufacturing of Soft Magnetic Materials in Electrical Machines. Machines 2023, 11, 702. https://doi.org/10.3390/machines11070702

14. Sala, G.; Giannotta, N.; Vogni, M.; Bianchini, C.; Immovilli, F. Analytical Model and Feasibility Assessment of a Synchronous Reluctance Tubular Machine with an Additively Manufactured Mover. Energies 2025, 18, 3918. https://doi.org/10.3390/en18153918

15. M. Vogni, G. Sala, E. Macrelli, C. Bianchini and A. Bellini, "Comprehensive Load Loss Model of an Ironless Machine: Advantages of Current Source Inverter Supply," in IEEE Transactions on Industry Applications, doi: 10.1109/TIA.2026.3656127.

Between these papers, only some of them are reported in this work of thesis:

- The eighth one named "Inductance Based Lumped Parameter IPM Machine Model for Fast Simulation" is reported in Chapter 1.
- Paper number thirteen named "A Review of Additive Manufacturing of Soft Magnetic Materials in Electrical Machines" is reported in Chapter 4.
- The first one named "Synchronous Reluctance Tubular Machine by Means of Additive Manufacturing" and the last one named "Analytical Model and Feasibility Assessment of a Synchronous Reluctance Tubular Machine with an Additively Manufactured Mover" are reported in Chapter 5.
- The third paper named "Innovative Rotor Winding Geometry for Synchronous Machine by Means of Additive Manufacturing" is reported in Chapter 6.
- Paper number seven named "A Double Three-Phase Axial-Flux Synchronous Reluctance Motor" is reported in Chapter 7.

Currently under revision:

1. G. Sala, C. Bianchini, M. Galea, A. Torreggiani, “Analytical Optimization for Concentrated Winding Machines for Marine Application”, ICEM 2026.
2. G. Sala, M. Galea, C. Bianchini, J. Cilia, “Motor Immersion in Sea Water for Marine Applications”, ICEM 2026.

Technical report:

1. Rete Alta Tecnologia Emilia Romagna, “Additive manufacturing applicato ai motori elettrici sincroni tubolari a riluttanza”

Tesi di dottorato finanziata dall'Unione europea- Next Generation EU, Missione 4, componente 2 "Dalla Ricerca all'Impresa" - Investimento 3.3 "Introduzione di dottorati innovativi che rispondono ai fabbisogni di innovazione delle imprese e promuovono l'assunzione dei ricercatori dalle imprese".